Ductility of M5® and ZIRLO® Sibling Pin Cladding

Spent Fuel and Waste Disposition

Prepared for
US Department of Energy
Spent Fuel and Waste Science and Technology

Argonne National Laboratory
M.C. Billone, T.A. Burtseva, Y. Chen and Z. Han

September 30, 2020
M2SF-20AN010201012
ANL-20/47

SUMMARY

This report satisfies SFWD-SFWST-2020 milestone M2SF-20AN010201012.

In support of the High Burnup Cask Demonstration Project (Demo Project), 25 sibling pins (i.e., fuel rods) irradiated to high burnup (HBU) have been provided for characterization and testing: (a) 15 fuel rods for Oak Ridge National Laboratory (ORNL), (b) 10 fuel rods for Pacific Northwest National Laboratory (PNNL), and (c) the equivalent of about 1.4 m of defueled cladding provided by ORNL and PNNL for testing at Argonne National Laboratory (ANL). These fuel rods were either extracted from fuel assemblies loaded into the Demo Cask or from assemblies with irradiation histories similar to assemblies loaded into the Demo Cask. ANL's mission is to conduct characterization and testing to determine if cladding retains ductility following drying and long-term storage. Ductility retention is desirable during all phases of storage and transportation, particularly during post-storage transport.

ORNL provided ANL with 12 cladding segments, each 90-mm long. Six segments were in the as-irradiated condition (i.e., baseline): (a) M5® fuel rod 30AD05 (two axial locations), (b) ZIRLO® fuel rod 3D8E14 (two axial locations) and (c) low-tin Zircaloy-4 (Zry-4) fuel rod 3A1F05 (two axial locations). Six segments (two per rod) were sectioned from M5®, ZIRLO®, and Zry-4 fuel rods (30AE14, 3F9N05, and F35P17, respectively), subjected to heat treatment at 400°C peak cladding temperature (PCT) for eight hours followed by cooling at ≤3.7°C/h to 100°C.

Four segments were inspected visually, and destructive examinations were conducted on two M5® segments (baseline and heat-treated) and two ZIRLO® segments (baseline and heat-treated). Metallographic examination was performed at three axial locations per segment to determine oxide-layer and metal-wall thickness, as well as hydride distribution and orientation. Eight ring compression test (RCT) samples per segment were prepared and tested. RCTs were performed at room temperature (RT) and 0.05 mm/s displacement rate to a maximum sample displacement of 1.7 mm. The maximum displacement was chosen to give about 10% offset strain for samples that did not experience significant load drops (>25%) at <1.7 mm. For such samples, 10% represents a lower bound on ductility. Three tests were stopped at <1.7 mm to determine cracking location and extent following steep load drops of 13%, 23%, and 29%. ***All 32 RCT samples exhibited ductility at RT with most samples achieving up to 10% offset strain without significant cracking.***

The as-irradiated and heat-treated M5® segments, as well as the heat-treated ZIRLO® segment, used in the current work, were from relative axial elevations of ≈90% from their respective fuel-column bottoms. The as-irradiated ZIRLO® segment was at a relative axial elevation of ≈70% from its fuel-column bottom. The oxide-layer thickness was measured and hydrogen content was estimated for each segment based on this thickness: (a) 90−100 wppm for as-irradiated M5® with 13±1 µm oxide layer, (b) 80−90 wppm for heat-treated M5® with 11±1 µm oxide layer, (c) 350±40 wppm for as-irradiated ZIRLO® with 28±3 µm oxide layer, and (d) 550±50 wppm for heat-treated ZIRLO® with 44±7 µm oxide layer. Hydrogen analysis will be performed to determine more precise values.

The heat-treated M5® segment was initially overheated to 485°C for ≈1.75 hours. At cooling initiation, the temperature had coasted down to 401°C with corresponding internal pressure of 7.24 MPa and average hoop stress of 52±1 MPa. The heat-treated ZIRLO® segment had a cooling-initiation temperature of 400°C with corresponding internal pressure of 8.99 MPa and average hoop stress of 66±1 MPa. These hoop stresses were considerably lower than the minimum values (80−90 MPa) used in previous ANL experiments. On the basis of ANL results for much higher hoop stresses, expectations were that radial hydrides would be relatively short and ductility values would be high.

Although metallographic examinations revealed relatively short radial hydrides and RCTs indicated high RT ductility for sibling pin M5® and ZIRLO® cladding, there were unanticipated results worth highlighting. Radial hydrides have been observed in as-irradiated HBU-fuel M5® and ZIRLO® cladding. However, these radial hydrides were too short and too isolated to affect cladding ductility. The microstructure (recrystallized-annealed) of M5® is more conducive to precipitating radial hydrides than the microstructure (cold-worked, stress-relief annealed) of ZIRLO®. As such, more radial hydrides were expected in as-irradiated M5® than in as-irradiated ZIRLO®. Metallographic examination revealed the opposite to be the case. Only two short radial hydrides (7% and 10% of the cladding wall) were observed in as-irradiated M5®. As-irradiated ZIRLO® had many short radial hydrides (8±4% of the cladding wall) and one that was 26% of the cladding wall. The short radial hydrides were located in the middle 70−80% of the cladding wall, which appeared to have very low hydrogen content. Most of the hydrogen was in the hydride rim (expected) at the cladding outer surface and in several circumferential hydrides near the cladding inner surface (unexpected). For as-irradiated ZIRLO® previously characterized by ANL, these inner-surface circumferential hydrides were located close to the mid-radius. The radial hydrides observed in as-irradiated ZIRLO® did not degrade ductility because they were located in low bending stress regions.

For heat-treated ZIRLO® (400°C/66-MPa) with ≈550 wppm hydrogen, circumferential hydrides below the hydride rim were more uniformly distributed than those observed in as-irradiated ZIRLO® with 350 wppm hydrogen. The radial-hydride continuity factor (RHCF), which is the effective radial hydride length relative to cladding wall thickness, was only 9±5% with a maximum value of 26% (similar to as-irradiated ZIRLO®). However, longer hydrides appeared close to the cladding inner surface, which is a region of high tensile hoop stress at loading and support locations. Load drops of 7−13%, and 23% were observed for six of the heat-treated RCT samples, four of which had regions of peeled oxide. Metallographic examination is in progress for samples with load drops of 13% and 23% to determine crack locations (relative to peeled oxide location) and crack lengths. Based on load recovery following the 7−13% load drops, cracking appeared to be minor. The 23% load drop at high offset strain (7.8%) indicated high ductility.

For heat-treated M5® (401°C/52-MPa), a large number of relatively short radial hydrides were observed, including radial hydrides clusters, emanating from the cladding inner surface. The RHCF was challenging to determine because of gaps between short radial hydrides. Radial hydrides separated by ≤5-μm in the radial direction were treated as continuous. It is assumed that a crack can propagate rapidly through ≤5 μm of metal from one radial hydride to the next. Using this assumption, the RHCF was measured to be 18±12% with a maximum value of 60%. As a result of these radial hydrides, load drops of 9% (at low displacement) and 29% (at high displacement) occurred for two RCT samples. Based on load recovery, the 9% load drop appears to have caused a minor crack, which had no effect on ductility. The 29% load drop resulted in a single crack 60% of the wall thickness at one end and two 54% wall cracks at the sample mid-span. However, the ductility of the sample was high (7.8%). Based on the observed crack lengths, it appears that rapid crack growth does occur between radial hydrides separated by ≤5 μm and may even occur between radial hydrides separated by >5 μm. Maximum RCT loads for heat-treated M5® (529±7 N) were compared to those for as-irradiated M5® (534±6 N). The overlapping data sets suggest that partial annealing did not occur during overheating (up to 485°C) of the heat-treated M5® fuel rod.

Future work will consist of characterizing and testing the remaining eight ORNL segments, as well as the ten defueled cladding segments PNNL will send to ANL. A new hydrogen analyzer has been ordered to allow determination of hydrogen content in sibling pin cladding. In addition to pre-RCT characterization, post-RCT metallographic examination will be performed to determine relationships between cracking extent, load-drop magnitude, and RHCF. These relationships are important in the establishment of the ASTM standard for RCT conduct and data analysis. With regard to the RHCF, the ≤5-μm gap criterion for continuity will continue to be evaluated and refined.

CONTENTS

FIGURES

TABLES

Page intentionally blank

REVISION HISTORY

Date	Revision	Changes
09/29/20	0	Draft submitted for DOE Policy Review; uploaded into PICS:NE
10/01/20	0	No changes after policy review

Page intentionally blank

ACRONYMS, UNITS AND SYMBOLS

ACRONYMS

AF	as-fabricated
ANL	Argonne National Laboratory
ASTM	American Society for Testing and Materials
CWSRA	cold-worked, stress-relief annealed
DE	destructive testing
DOE	U.S. Department of Energy
DTT	ductility transition temperature
EPRI	Electric Power Research Institute
FEA	finite element analysis
FHT	full-length heat treatment
HBU	high burnup
LT	low tin
LVDT	linear variable differential transformers
NDE	nondestructive testing
MET	metallographic examination
NRC	Nuclear Regulatory Commission
ORNL	Oak Ridge National Laboratory
PCT	peak cladding temperature
PNNL	Pacific Northwest National Laboratory
PWR	pressurized water reactor
RCT	ring compression test
RHCF	radial hydride continuity factor (%)
RHT	radial-hydride treatment
RIP	rod internal pressure
RT	room temperature
RXA	recrystallized-annealed
SFWST	Spent Fuel Waste and Science Technology
TBD	to be determined
Zry-4	Zircaloy-4

UNITS

°C	degree Celsius
GWd/MTU	giga-watt-days per metric ton (tonne) of uranium
h	hour
kN	kilo-newton
m	meter
mm	millimeter
µm	micro-meter (micron)
MPa	mega-pascal
N	newton
Pa	pascal
s	second
wppm	weight parts per million

SYMBOLS

C_H	total hydrogen content in weight parts per million (wppm)
D_{mi}	inner diameter of cladding alloy (mm)
D_{mo}	outer diameter of cladding alloy (mm)
D_o	cladding outer diameter (includes outer-surface oxide layer if present, mm)
d_p	permanent displacement (pre-test minus post-test diameter in loading direction, mm)
d_p/D_{mo}	permanent strain (%)
δ	controlled sample displacement (mm) at the 12 o'clock loading position
δ_e	elastic displacement (mm)
δ_{max}	maximum sample displacement (mm) at the 12 o'clock sample position
$\Delta L/L_o$	change in length (ΔL) normalized to initial length (L_o)
Δp	pressure difference across cladding wall ($p_i - p_o$, MPa)
δ_p	corrected offset displacement (mm)
δ_{pt}	traditional offset displacement (mm)
δ_p/D_{mo}	corrected offset strain (%)
δ_{pt}/D_{mo}	traditional offset strain (%)
E	Young's modulus (GPa)
ε_θ	hoop strain calculated using small strain assumption
e_θ	hoop strain calculated from large-strain theory
h_m	cladding alloy wall thickness (mm or µm)
h_{ox}	thickness of outer surface oxide layer (µm)
K_{LC}	calculated loading slope (i.e., loading stiffness) for RCT samples (kN/mm)
K_{LM}	measured linearized loading slope (kN/mm)
K_U	calculated linearized unloading slope (kN/mm)
K_{UM}	measured linearized unloading slope (kN/mm)
L	length of RCT sample (mm)
M_{max}	maximum RCT bending moment (N•m)
ν	Poisson's ratio
P	measured RCT load at the 12 o'clock sample position (N or kN)
P_e	load during elastic displacement (N)
p_i	internal gas pressure (MPa)
P_{max}	maximum RCT load (N)
p_o	external gas pressure
R_{mi}	inner radius of cladding alloy (mm)
R_{mid}	mid-wall radius of cladding alloy (mm)
σ_θ	hoop stress (MPa)
$\sigma_{\theta Y}$	yield stress in hoop direction (MPa)
$\sigma_{\theta UTS}$	ultimate tensile stress in hoop direction (MPa)
σ_{rY}	yield stress in radial direction (MPa)
σ_{zY}	yield stress in axial direction (MPa)
σ_{zUTS}	ultimate tensile stress in axial direction (MPa)
T	temperature (°C)
T_D	hydrogen dissolution temperature (°C)
T_P	hydrogen precipitation temperature (°C)
z/L_f	axial position (z) from bottom of fuel column divided by fuel column length (L_f)

1. INTRODUCTION

The High Burnup Cask Demonstration Project (Demo Project) is a DOE-Industry effort that addresses the effects of long-term, dry-cask storage and transportation on high-burnup (HBU, >45 gigawatt-days per metric ton uranium [GWd/MTU]) pressurized water reactor (PWR) fuel rods. The overall goal of the program is to assess the integrity of HBU PWR fuel rods under long-term storage and post-storage transportation. In November 2017, thirty-two PWR fuel assemblies, which were irradiated in Dominion's North Anna Power Station to HBU, were loaded into an instrumented cask, dried, and transferred to the storage pad. In addition to collecting valuable thermal and gas sampling data during drying, transfer, and early storage, the cask will be stored for about ten years, during which time it will be transported to a DOE facility for post-storage/transport inspection, characterization, and possible testing.

In support of the Demo Project, 25 fuel rods irradiated to HBU in the same power station were sent to Oak Ridge National Laboratory (ORNL) for nondestructive examination (NDE). The rods are referred to as sibling pins (previously called sister rods) because they have similar designs and irradiation histories as the stored fuel rods with many of the rods extracted from fuel assemblies loaded into the Demo Cask. A full description of these 25 fuel rods, along with NDE results, is presented in Ref. 1. Destructive examinations (DEs) are being performed at ORNL, Pacific Northwest National Laboratory (PNNL), and Argonne National Laboratory (ANL) in accordance with the Phase 1 Test Plan [2]. This plan calls for characterization and mechanical-properties determination of fuel-rod cladding in the as-irradiated condition and following heat treatment at 400°C for eight hours and cooling at ≤5°C/h. The 400°C heat-treatment temperature is consistent with the peak cladding temperature (PCT) limit of 400°C recommended by the Nuclear Regulatory Commission (NRC) [3]. ORNL [4] and PNNL [5] have already performed preliminary DEs, including rod internal pressure (RIP) measurements for 18 fuel rods. PNNL has received 10 of the 25 fuel rods and ANL is scheduled to receive about 1.4 m of defueled cladding from ORNL and PNNL, as well as PNNL cladding ring compression test (RCT) samples. The defueled cladding samples from ORNL and PNNL will be characterized and subjected to RCTs to determine ductility as a function of test temperature. Maintaining ductility is desirable for all phases of drying, transfer, storage and transport, especially post-storage transport.

ORNL shipped to ANL 12 defueled cladding segments, each 90-mm long, from fuel rods clad in M5®, ZIRLO®, low-tin (LT) Zircaloy-4 (Zry-4), and standard Zry-4. Six of these segments were in the as-irradiated condition and six were from three fuel rods subjected to full-length heat treatment (FHT): heat pressurized rod to 400°C, hold at 400°C for 8 hours, and cool at ≈3.7°C/h. One purpose of the FHT is to determine if radial hydrides precipitate during cooling and if they have any detrimental effect on cladding mechanical properties, particularly ductility. The uniform PCT of 400°C bounds internal rod pressures and cladding hoop stresses for fuel rods subjected to drying, transfer, and storage during normal operation. The 12 cladding segments are summarized in Section 2. Characterization and RCT results are presented in Section 4 for a pair of as-irradiated and heat-treated M5® segments. Section 5 gives similar results for a pair of as-irradiated and heat-treated ZIRLO® segments.

Hydride morphology and orientation are expected to be different in M5® as compared to ZIRLO® because of the low-hydrogen content in M5® and because of its recrystallized-annealed (RXA) microstructure. ZIRLO® cladding has much higher hydrogen content and has a cold-worked, stress-relief-annealed (CWSRA) microstructure.

Future ANL work will include characterization, RCTs, and post-RCT characterization of the remaining eight ORNL defueled cladding segments, as well as the 10 defueled cladding segments to be received from PNNL.

Section 2 describes the ANL protocol for conducting RCTs and for analysis of RCT load displacement curves to determine offset strain and ductility. It also includes the embrittlement criteria used by ANL. The Section 2 material forms the basis for the American Society for Testing and Materials (ASTM) standard being developed by ANL for RCTs.

The RCT is used as a ductility screening test to determine the ductility transition temperature (DTT). The DTT is the temperature at which the ductility (offset strain prior to >50% wall crack) is 2%. At temperatures below the DTT, the offset strain is <2% and the material is classified as brittle. Permanent displacement is determined from pre- and post-test diameters measured along the loading direction for samples that do not exhibit cracking. Offset displacement is determined from load-displacement curves for samples that exhibit cracking. These are normalized to the cladding outer diameter to calculate relative displacement (strain) for the ring structure. The structural strain differs from the local strain in the ring material. The situation is analogous to a coiled spring subjected to a tensile force. If the spring displacement exceeds the material elastic limit, permanent elongation is present after the load is released. Normalizing the permanent change in length to the initial length gives the structural strain for the spring. However, the plastic strains in the coil material are different from the structural strain. The relationship between structural strain and material strain is quantified in Section 3. Measured RCT structural strains are compared to material strains calculated using the finite element analysis (FEA) model for as-fabricated (AF) 17×17 M5® benchmark rings at four displacement levels. The material presented in Section 3 is useful for understanding the circumferential and radial variations of stress and strain in a compressed ring. However, a detailed knowledge of mechanical properties in the circumferential, axial, and radial directions would be needed to determine the distribution of material strain in anisotropic materials such as zirconium-based cladding alloys. As such detailed information is generally not available, structural strain continues to be the metric used for the RCT ductility screening test.

2. HBU-FUEL CLADDING MATERIALS AND TEST METHODS

2.1 HBU-FUEL CLADDING MATERIALS

Table 1 summarizes relevant features of the twelve 90-mm-long cladding segments received from ORNL. The first six segments are from sibling pins that were heat treated by ORNL using the FHT protocol [4] prior to puncturing for rod internal pressure (RIP) measurements, sectioning, defueling and shipment to ANL. The remaining six segments are cladding in the as-irradiated condition. The ORNL segment ID number can be determined by combining the fuel rod number with the axial distances from the bottom of the fuel rod (e.g., ANL segment 654A is equivalent to ORNL ID 30AE14 2694 2784). For items listed in bold black, characterization and RCT data are presented in Sections 4 and 5 for M5® and ZIRLO® cladding, respectively. TBD stands for to be determined, and σ_θ (PCT) is the wall-averaged hoop stress at the PCT. The top zone of heat-treated M5® fuel rod (30A-E14) experienced overheating to 485°C for ≈1.75 hours during the heating ramp [4]. If the whole fuel rod were at 485°C the RIP would have increased to 8.14 MPa and the corresponding hoop stress would have been 58 MPa, which is too low for thermal creep to occur. During the 8-hour "hold time," the temperature decreased to 401°C at cooling initiation. Segment 654B (3309−3399 mm from the fuel rod bottom) was part of this overheated zone. From the perspective of hydrogen precipitation, the rod internal pressure at cooling initiation is relevant for low-hydrogen-content M5® cladding. The overheating would not have increased the hydrogen in solution because all hydrogen would have been in solution by ≈325°C. However, the overheating may have resulted in partial annealing of radiation damage, which would have a positive effect on cladding ductility. Partial annealing would reduce the cladding yield stress, which in turn would reduce the maximum load achieved during RCTs. However, the best way to assess the effects of overheating would be to perform hardness tests on cladding within the overheated zone and cladding below this zone for which the PCT was 400°C.

Table 1 Summary of cladding alloys and relevant sibling pin information for the 12 defueled cladding segments provided by ORNL.

Cladding Alloy	Burnup, GWd/MTU	ANL ID	Fuel Rod ID	Axial Span, mm	RIP at 25°C, MPa	FHT PCT, °C	σ_θ (PCT), MPa
M5®	54	654A	30A-E14	2694−2784	3.2	400	52
M5®	**54**	**654B**	**30A-E14**	**3309−3399**	**3.2**	**401**	**52**
ZIRLO®	54	656A	3F9-N05	2572−2662	4.0	400	TBD
ZIRLO®	**54**	**656B**	**3F9-N05**	**3241−3331**	**4.0**	**400**	**66**
Zry-4	60	658A	F35-P17	2555−2645	4.7	400	66
Zry-4	60	658B	F35-P17	3069−3159	4.7	400	TBD
M5®	54	653A	30A-D05	2429−2519	3.5	---	---
M5®	**54**	**653B**	**30A-D05**	**3259−3349**	**3.5**	**---**	**---**
ZIRLO®	54	655A	3D8-E14	2213−2303	4.2	---	---
ZIRLO®	**54**	**655B**	**3D8-E14**	**2565−2655**	**4.2**	**---**	**---**
LT-Zry-4	51	657A	3A1-F05	2555−2645	3.7	---	---
LT-Zry-4	51	657B	3A1-F05	3015−3105	3.7	---	---

The 12 ORNL segments were unloaded from shield containers and aluminum-alloy shipping tubes in ANL's Irradiated Materials Laboratory Hot Cell 3. Two pairs of segments were moved to a glove box for imaging, length and diameter measurements, and sectioning. Photographs of the two M5® segments (654B and 653B) are shown in Fig. 1. Each segment had a mark near the left end indicating the top of the segment relative to the orientation of the fuel rod. The appearance (ignoring color differences) of these two

segments is consistent with ORNL NDE results [1]. Figure 2 shows two orientations of ZIRLO® segment 656B from fuel rod 3F9-N05. The dark spots indicate regions of peeled oxide, which is also consistent with ORNL NDE results. The lower half of the bottom figure contains axial magic marker lines that partially obscure some peeled oxide under those lines. These lines are an artifact and do not represent peeled oxide. As-irradiated ZIRLO® segment 655B was inspected visually, but it was not photographed. It contained no unusual features.

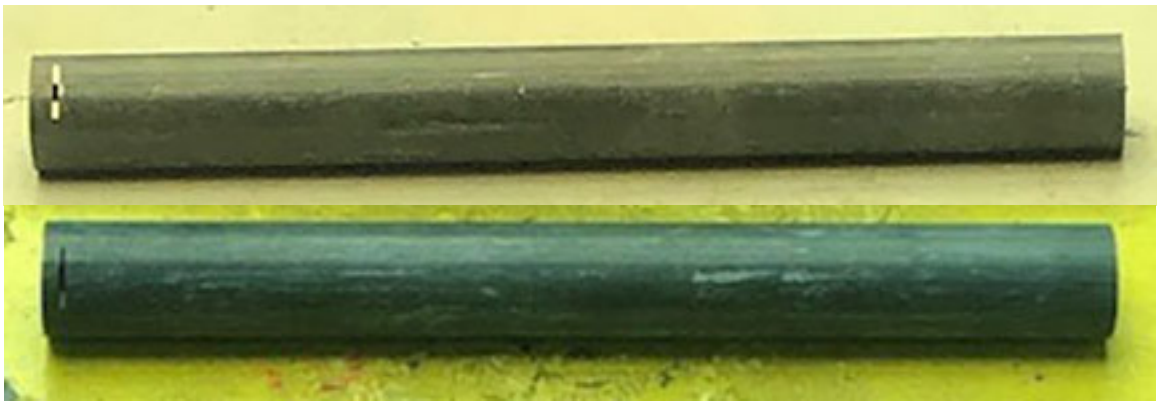

Figure 1: Physical appearance of M5® cladding segments 654B (top) and 653B (bottom).

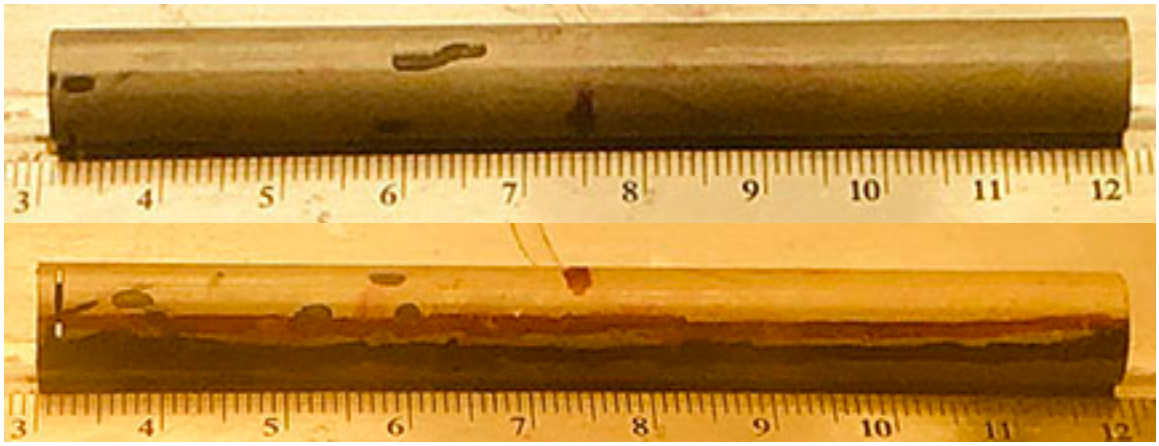

Figure 2: Physical appearance of ZIRLO® cladding segment 656B.

The terms “peeled” and “spalled” both refer to delamination and flaking off of the oxide layer. Spallation is used to describe complete delamination and flaking off of the oxide layer down to the cladding metal. Spalling results in a cold spot on and in the cladding, which may result in increased hydrogen content and hydride blisters in cladding under the spalled oxide. Peeling is used to describe partial delamination and flaking off of the outer region of the oxide layer (e.g., 5% to 50% of the oxide layer). The consequences of peeling are considered to be benign with respect to hydrogen-content increase under peeled regions.

The as-irradiated M5® and FHT M5® and ZIRLO® segments were from an elevation about 90% from the bottom of the fuel column, close to or within the burnup downslope and the upper grid spacer. The as-irradiated ZIRLO® segment (70% elevation above bottom of fuel column) was within the uniform burnup region and not under a grid space.

2.2 TEST METHODS

The ANL protocol [6] has been described for heat-treating pressurized rodlets fabricated from defueled cladding segments. Experimentally, this process is called radial-hydride treatment (RHT). However, the current work involves cladding from ORNL FHT [4]. During FHT, pressurized full-length fuel rods were heated to a PCT of ≈400°C at 10°C/h, held at the PCT for eight hours, and cooled down to 100°C at ≈3.7°C/h. Prior to FHT, cladding profilometry was performed to determine cladding outer diameter (D_o) as a function of axial position. Following FHT, the rod internal pressure (p_i) was measured and extrapolated to 25°C (see Table 1). Sectioning and defueling were performed for segments sent to ANL.

The ideal gas law was used to calculate p_i at the PCT: p_i (PCT) = ([PCT + 273]/298) p_i (25°C). This relationship assumes no significant increase in void volume due to heating. Cladding geometrical parameters, along with the ambient pressure in the ORNL hot cell, are needed to determine the wall-average cladding hoop stress. Hot cell pressures are slightly less than ambient pressures within the hot-cell building, which are smaller than atmospheric pressures outside the building. The hot cell pressure is assumed to be 0.1 MPa even though it is lower. The lower the external pressure (p_o) is on the cladding wall, the less significant it is. It is more significant in dry-storage canisters where it can be as high as 0.6 MPa for convection canisters.

Cladding geometrical parameters needed to calculate stress from pressure are the inner radius of the cladding (R_{mi}) and the metal wall thickness (h_m), which is measured as part of metallographic examination. The corroded cladding D_o is measured by profilometry for a full-length rod (ORNL) or via calipers for a cladding segment (ANL). Given the oxide-layer thickness (h_{ox}) measured as part of metallographic examination, the outer diameter of the cladding alloy (D_{mo}) is $D_o - 2\ h_{ox}$, and the cladding alloy inner diameter (D_{mi}) is simply $D_{mo} - 2\ h_m$. The ratio R_{mi}/h_m, where R_{mi} is $D_{mi}/2$, is used in Eq. 1 to calculate the average hoop stress (σ_θ) from the pressure difference ($\Delta p = p_i - p_o$) across the cladding wall.

$$\sigma_\theta = (R_{mi}/h_m)\ \Delta p - p_o \qquad (1)$$

Equation 1 is valid for both thick- and thin-wall pressurized tubes. In many reports, papers, and textbooks, R_{mi} is replaced by the mid-wall radius ($R_{mid} = [D_{mo} - h_m]/2$) for thin-wall tubes. For as-fabricated 17×17 cladding with 9.50-mm D_{mo} and 0.57-mm h_m, this approximation leads to a 7% overestimation of the average cladding hoop stress for $p_o << p_i$.

The second phase of the test protocol consists of RCTs. Figure 3 shows a schematic of the RCT loading. The displacement (δ) is determined from the controlled displacement rate and the load (P) is measured. The loading induces maximum tensile hoop bending stresses (σ_θ) at the inner surfaces of the 12 (under load) and 6 (above support) o'clock positions. Tensile hoop stresses also occur at the 3 and 9 o'clock outer surfaces. Associated with these tensile stresses are tensile strains (ε_θ). Stresses induced by shear and normal loads are insignificant relative to bending stresses. Within the elastic range, hoop stresses at 3 and 9 o'clock are about 40% less than hoop stresses at 12 and 6 o'clock. Also, because the length (L ≈ 8 mm) of the rings is much greater than the cladding wall thickness (0.54 to 0.57 mm for 17×17-array PWR HBU-fuel-rod cladding), an axial stress is induced that is up to 0.37 times the hoop stress within the elastic deformation regime. The maximum sample displacement (δ_{max} = 1.7 mm) is chosen to give ≈10% offset and permanent strains for the ring structure. This maximum displacement gives an S-shaped offset strain vs. test temperature curve for brittle-to-ductile materials with a "lower-shelf" plastic strain <2% and an "upper-shelf" plastic strain of about 10% from which the DTT can be determined. The reference displacement rate used in previous testing was 5 mm/s. It was reduced to 0.05 mm/s for the current tests to allow real-time visualization of the load-displacement curve and load removal following a significant load drop.

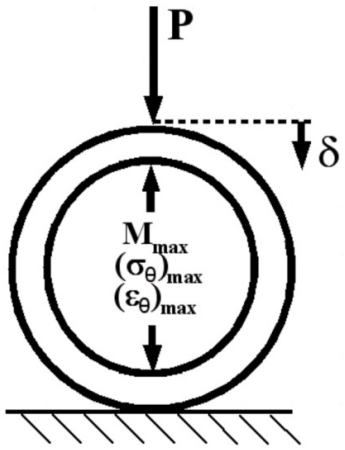

Figure 3: RCT measured load (P) and controlled displacement (δ).

Load-displacement curves and post-test diameter measurements are used to determine offset (δ_p) and permanent (d_p) displacements, respectively. These are normalized to D_{mo} to give relative plastic displacement (i.e., plastic strain) for the ring structure. Permanent displacement is defined as the difference between pre- and post-test diameter measurements along the loading direction. Figures 4 and 5 show how traditional (δ_{pt}) and corrected (δ_p) offset displacements are determined from benchmark load-displacement curves for AF 17×17 M5® rings subjected to displacements of 1.7-mm (Fig. 4) and 0.5-mm (Fig. 5). For the benchmark samples, D_{mo} = 9.49 mm in the loading direction, h_m = 0.57 mm, and L = 8.06 mm. The traditional offset-displacement methodology calls for unloading the sample at the same slope as the measured linearized loading slope (K_{LM}). It should be noted that K_{LM} is less than the calculated ring stiffness (K_{LC}) due to the influence of machine compliance. For the case shown in Fig. 4, this approach gives δ_{pt} = 1.24 mm, which is greater than the more accurate d_p = 1.10 mm. Thus, there is an inherent error in the traditional approach as the measured linearized unloading slope (K_{UM}) is always less than K_{LM}. K_{UM} is determined from the slope of the line connecting δ_{max} to the displacement axis value based on the measured value of d_p at zero load. Normalizing these displacements to D_{mo} gives 13% traditional offset strain and 11.6% permanent strain, which is also the corrected offset strain (δ_p/D_{mo}) for these benchmark tests. For Fig. 4, K_{UM}/K_{LM} is 0.771. As the total and traditional offset displacements decrease, the difference between δ_{pt} and d_p decreases. This is shown in Fig. 5 for which δ_{pt} is 0.11 mm, d_p is 0.09 mm, and K_{UM}/K_{LM} is 0.944.

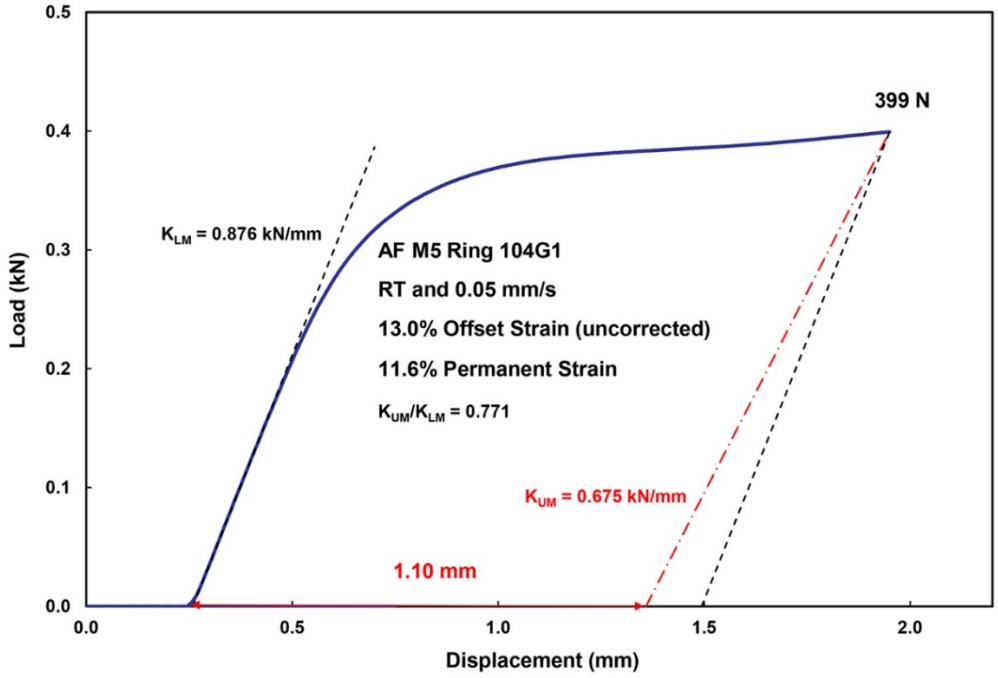

Figure 4: Load-displacement curve for AF M5® ring tested at RT and 0.05 mm/s to 1.7-mm displacement.

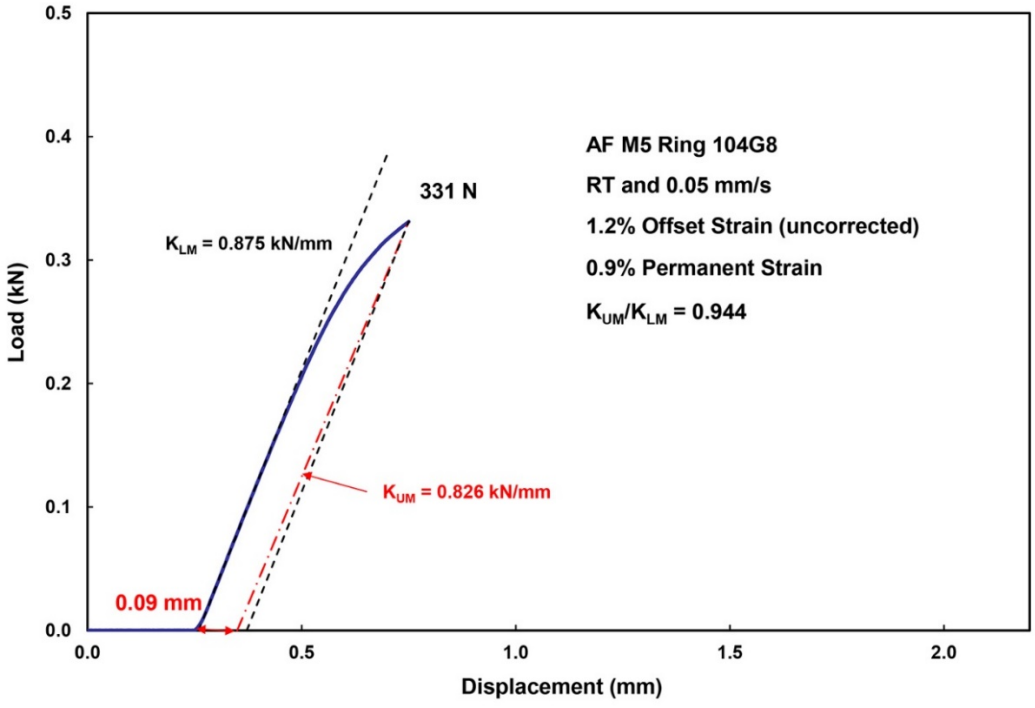

Figure 5: Load-displacement curve for AF M5® ring tested at RT and 0.05 mm/s to 0.5-mm displacement.

Energy methods were used to determine the bending moment as a function of circumferential orientation. Both wide-beam and narrow-beam assumptions were used to relate the bending moment to bending stresses and strains within the elastic-deformation regime, as well as the relationship between the elastic load (P_e) and elastic displacement (δ_e). The curvature of the ring was not taken into account in the bending analysis. The calculated loading stiffness is $K_{LC} = P_e/\delta_e$, where

$$P_e = f(\nu) \{(E\ L)/(1.79)\} (h_m/R_{mid})^3\ \delta_e \quad (2)$$

In Eq. 2, E is Young's modulus (91.9 GPa for RXA alloys at room temperature [7]) and ν is Poisson's ratio (0.37 for RXA and CWSRA alloys at RT to 400°C [8]). For a narrow beam (in terms of the length [L] to h_m ratio), f (ν) = 1. For a wide beam (L/h_m >>1), it is difficult for the material to expand or contract in the length direction and the assumption of plane strain in the axial direction leads to f (ν) =$1/(1-\nu^2)$ = 1.16. However, no guidance is given in the literature for determining f (ν) as a function of L/h_m. FEA calculations were used to determine that f (ν) = 1.09 for L = 8 mm and h_m = 0.57–0.61 mm (L/h_m = 13.1 to 14.0), which is close to half way between the narrow- and wide-beam solutions.

For HBU-fuel cladding rings that crack during the 1.7-mm displacement, d_p cannot be determined accurately. Thus, one must rely on a correlation for the unloading slope to determine the corrected offset displacement prior to the first significant crack, from which the ductility is determined. The correlation developed for this application is based on the results from a large number of benchmark tests with permanent displacements ranging from 0.09 mm to 1.4 mm, displacement rates of 0.03−50 mm/s, and temperatures of 20−150°C. Results of these benchmark tests are shown in Fig. 6 for the ratio of measured unloading/loading (K_{UM}/K_{LM}) slope vs. traditional offset strain (δ_{pt}/D_{mo}). Also shown in Fig. 6 are results from nine RCTs with HBU-fuel M5® (solid red circles) that exhibited no cracking after 1.7-mm total displacement. The blue hollow-circle data points are from RCTs conducted with AF 17×17 M5® (48 points) and AF 17×17 ZIRLO® (six points) cladding samples. Outer diameters were 9.49±0.1 mm and nominal cladding wall thickness values were 0.61 mm (reference case) and 0.57 mm (six ZIRLO® data points and 15 M5® data points). The data set includes RCT results from two machines: (a) screw-type Instron 5556 and (b) servo-hydraulic Instron 8511. Results are also shown for shorter (6 mm) and longer (10 mm) rings, as well as larger-diameter 15×15 M5® rings.

The correlation for the ratio K_U/K_{LM} as a function of δ_{pt}/D_{mo} (in %) is:

$$K_U/K_{LM} = 1 - 0.0303\ \delta_{pt}/D_{mo} \text{ for } \delta_{pt}/D_{mo} \leq 8.0\% \quad (3a)$$

$$K_U/K_{LM} = 0.758 \text{ for } \delta_{pt}/D_{mo} > 8.0\% \quad (3b)$$

The stiffness ratio for HBU-fuel M5® with >8% traditional offset strain is 0.746, which is in good agreement with the 0.758 determined for AF cladding materials.

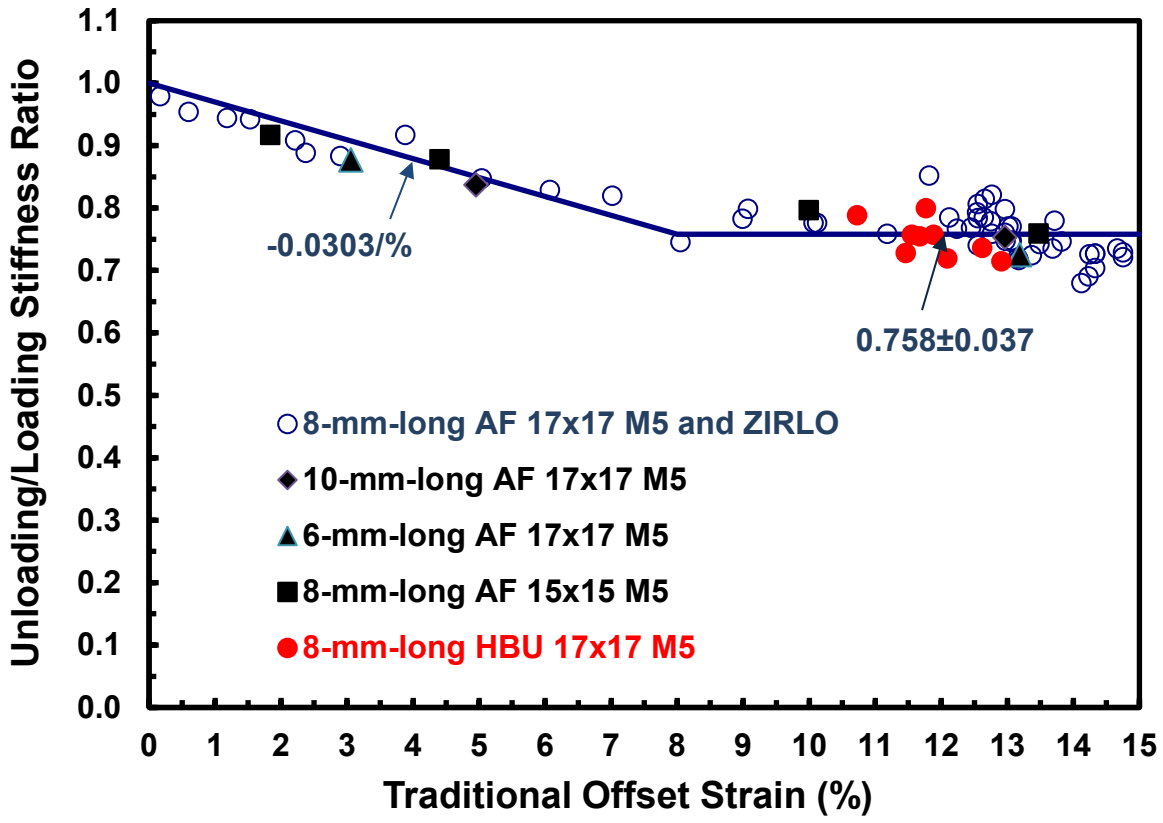

Figure 6: RCT benchmark results for determining the unloading/loading stiffness ratio as a function of the traditional offset strain.

There is reasonable confidence in using Eqs. 3a and 3b to calculate the corrected offset displacement (δ_p) and corresponding corrected offset strain (δ_p/ D_{mo}) for cladding rings that do not crack prior to a significant load drop. However, with the possible exception of HBU-fuel M5® with long radial hydrides, sparsely distributed circumferential hydrides, and a thin oxide layer (≈10±3 µm), most HBU-fuel cladding samples exhibited some cracking prior to the maximum displacement or prior to a significant load drop. The effects of minor cracks (e.g., multiple short cracks through the hydride rim) can reduce the unloading slope by as much as 25%. A large number of tests with HBU-fuel cladding would be needed to develop a correlation for unloading slope as a function of number and depth of cracks. Until such tests are performed, uncertainty in the determination of the corrected offset strain is taken into account in the formulation of the embrittlement criterion. A set of criteria is described below.

Two of the criteria for determining embrittlement remain unchanged since 2013 for cladding with radial and circumferential hydrides: δ_p/D_{mo} <2% prior to >25% load drop or >50% decrease in re-loading slope. In previous work [10–11], it was established that >25% load drop or >50% decrease in re-loading slope corresponded to a crack or cracks extending through >50% of the wall thickness. A third criterion was added within the past few years for load-displacement curves that indicated major cracking could occur within the transition from elastic to elastic-plastic displacement without exhibiting either a 25% load drop or a 50% decrease in elastic re-loading slope, for which an "implied" load drop >25% is used. The implied load drop criterion can result in a significant decrease in ductility. It is based on comparing the load-bearing capability of the suspect ring to loads achieved by intact rings and rings with severe load drops indicative of significant cracking.

The 2% offset strain limit is based on the uncertainty in the measurement of the permanent displacement (pre-test diameter minus post-test diameter) for HBU-fuel cladding and the added uncertainty in the permanent displacement measurement for HBU-fuel cladding due to flaking off of the oxide layer under the applied loading plate and above the support plate. Multiple cracks through the oxide layer and the hydride rim lower the unloading stiffness to values less than shown in Fig. 6, which has also been factored into the 2% offset-strain limit.

The relative displacements for the ring structure are referred to as strains, but they do not represent strains in the material. An apt analogy would be to consider a coiled spring that lengthens due to tensile loading. If the spring is pulled beyond the elastic limit of the coils, there is a permanent increase in length (ΔL) after unloading. From a structure perspective, the permanent strain (i.e., relative displacement) is $\Delta L/L_o$, where L_o is the initial length of the spring prior to application of the load. However, the plastic strain in the coil material is quite different from $\Delta L/L_o$ and is a combination of shear and tensile strains.

As the HBU-fuel M5® tested had very thin oxide layers (10±3 μm) and no hydride rim, the 2% offset strain criterion is more conservative for this HBU-fuel alloy than for the HBU-fuel Zry-4 and ZIRLO® samples tested, both of which had thicker oxide layers (30−100 μm), thick hydride rims (30−100 μm), and minor cracks through the oxide layer and the hydride rim during the RCT.

3. FEA RESULTS FOR RCT LOADING

The FEA model was developed using ABAQUS for cladding rings subjected to RCT hoop-bending loading. The model includes the machine stiffness (>10 kN/mm), elastic properties for RXA AF M5® (i.e., E= 91.9 GPa [7] and ν = 0.37 [8] at RT), large strain capability, and anisotropic plastic stress-strain properties. ABAQUS allows for specification of three anisotropy factors for principal yield stresses and three anisotropy factors for shear yield stresses. Given that parameters are adjusted to match a single load-displacement curve, there is no unique set of anisotropy factors that can be determined, as multiple combinations of anisotropy factors will result in a good fit with the measured load-displacement curve. In this section, we focus only on the anisotropy factors (ratios of yield stresses) for the hoop, axial, and radial yield stresses. In addition to variations in yield stress with principal axes, the strain hardening exponent is likely to be different for the three principal axes. However, the anisotropic model in ABAQUS is limited to one strain hardening exponent for plastic flow in the hoop, axial, and radial directions. Excluding anisotropy factors for shear stresses, that leaves six unknowns, which cannot be uniquely determined from an RCT load-displacement curve.

Literature values [11] for the hoop tensile properties of AF M5® were based primarily on results of ring-stretch tests conducted at low and high strain rates (up to 500%/s): 432 MPa hoop yield stress ($\sigma_{\theta Y}$) and 516 MPa hoop ultimate tensile stress ($\sigma_{\theta UTS}$), both at RT (22°C). Based on unpublished ANL data, the axial tensile properties measured at RT and 0.1%/s strain rate were: 400 MPa for σ_{zY} and 530 MPa for σ_{zUTS}. Although the strain-rate dependence of these properties should be relatively low, it is surprising that the literature values are treated as strain-rate independent. Use of these properties in the FEA model resulted in an under-prediction of load in the elastic-plastic displacement regime. Thus, yield stresses were modified for each ABAQUS run until good agreement was obtained between calculated and measured RCT load-displacement curves. In previous work [6], the best fit was obtained with 540 MPa for $\sigma_{\theta Y}$, 513 MPa for σ_{zY}, and 567 MPa for σ_{rY} (not measured). In the current work, more reasonable values of the hoop and axial yield stress values were used in combination with an elevated value of the radial yield stress: 440 MPa for $\sigma_{\theta Y}$, 400 MPa for σ_{zY}, and 638 MPa for σ_{rY}.

The FEA model includes the machine stiffness, as is shown in Fig. 7. For machine stiffness values >10 kN/mm, as is the case, the elastic loading slope and plastic deformation are relatively insensitive to machine stiffness for sample stiffness values <1 kN/mm. For computational-stability purposes, the friction coefficient between the loading/support plates and the sample was set at 0.1.

It is interesting to compare the structure strain determined from load-displacement curves with the peak material plastic hoop strain for purposes of enhancing fundamental understanding. As demonstrated previously [6], the structure strain is higher than the material strain in the elastic deformation regime, lower at 0.7-mm displacement, and higher at 1.7-mm displacement. In the current work, structure and material strains are compared for displacements of 0.5 mm and 0.9 mm. These results are for benchmark AF 17×15 M5® cladding rings with 9.49-mm outer diameter, 0.57-mm wall thickness and 8-mm length.

Previously Reported Results [6] for 1.7-mm Displacement of an AF M5® Benchmark Sample

Figure 8 shows the FEA-calculated and measured load-displacement curves for 1.7-mm displacement of an AF 17×17 M5® benchmark sample. The good agreement was obtained by fixing the hoop (440 MPa) and axial (400 MPa) yield stresses and increasing the radial yield stress to 638 MPa. The measured permanent structure strain was 11.6% and the maximum FEA-calculated plastic hoop strain after unloading was 0.08737 large strain (9.13% small strain), which is lower. The hoop stress distribution at 1.7 mm and the plastic hoop strain distribution after unloading are shown in Figs. 9a and 9b, respectively.

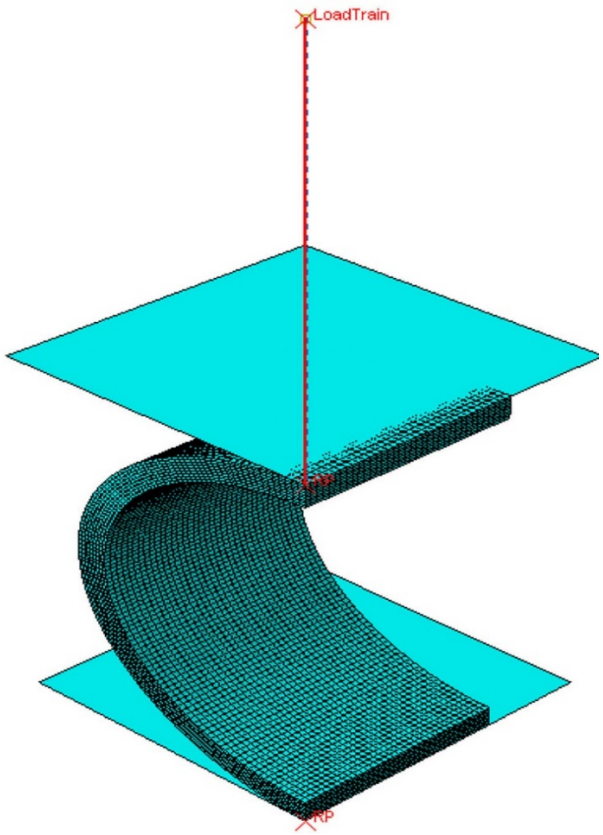

Figure 7: FEA model for RCT loading in benchmark tests.

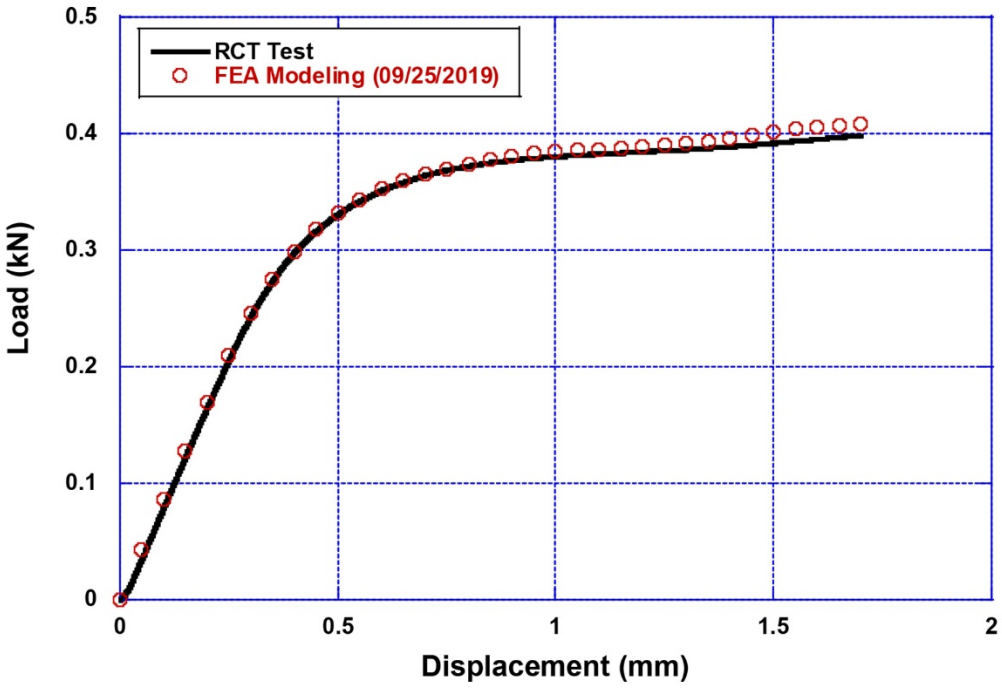

Figure 8: Comparison of FEA-predicted and measured load-displacement curves for 1.7-mm displacement of an AF M5® benchmark sample.

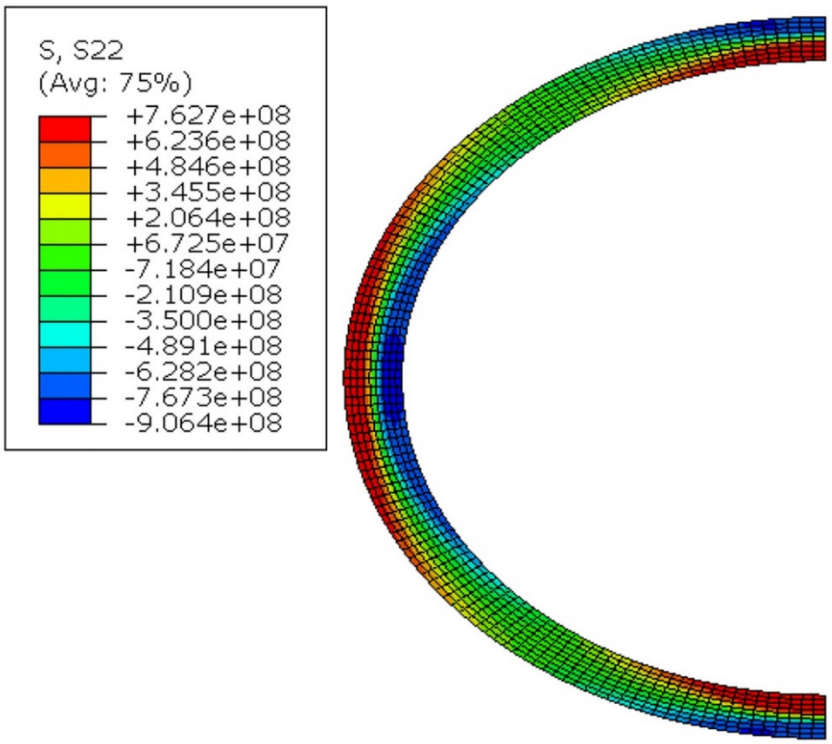

(a)

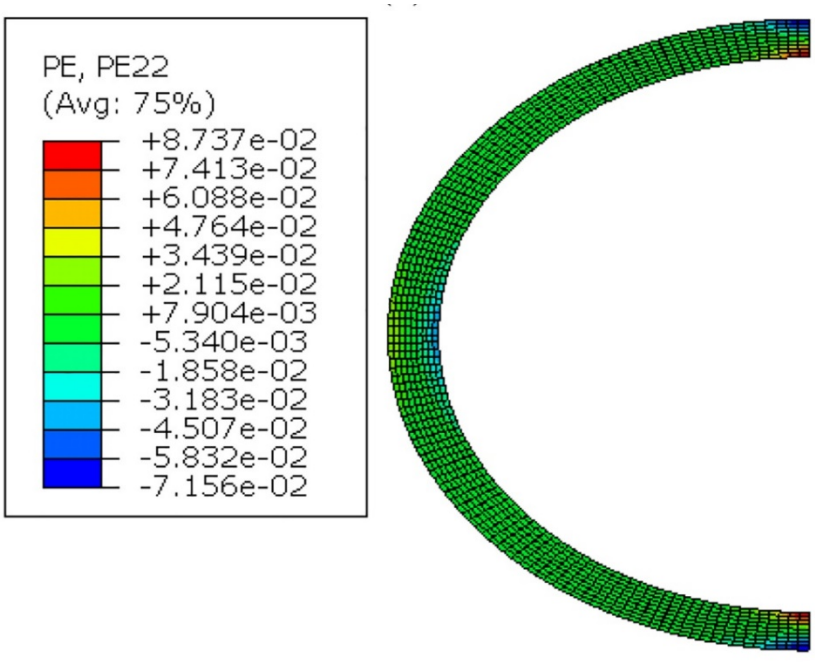

(b)

Figure 9: FEA-predictions for an AF M5® sample subjected to 1.7-mm displacement: (a) hoop stress (Pa) at 1.7-mm displacement and (b) plastic hoop strain after unloading.

Previously Reported Results [6] for 0.7-mm Displacement of an AF M5® Benchmark Sample

The measured load-displacement curve for 0.7-mm displacement is shown in Fig. 15 of Ref. 6. FEA predictions are repeated here for the convenience of the reader. Figures 10a and 10b, respectively, show the FEA-calculated hoop stress distribution at 0.7-mm displacement and the plastic hoop strain distribution after unloading. The FEA-calculated maximum hoop stress at 0.7 mm was 760 MPa and the maximum plastic hoop strain after unloading was 0.0292 (large strain). The small-strain equivalent was 2.96%, which is larger than the permanent structure strain (2.3%).

FEA-Predicted Results for 0.5-mm Displacement of an AF M5® Benchmark Sample

The load-displacement curve for this case is shown in Fig. 5. The hoop stress distribution prior to unloading and the plastic hoop strain distribution following unloading from 0.5 mm are shown in Figs. 11 and 12, respectively. The peak cladding hoop stress at 0.5 mm is predicted to be 743 MPa. The peak plastic hoop strain following unloading is 0.01399 (large-strain), which corresponds to 1.41% (small-strain). This is higher than the measured 0.9% permanent structure strain.

FEA-Predicted Results for 0.9-mm Displacement of an AF M5® Benchmark Sample

The FEA-predicted distributions of hoop stress at 0.9-mm displacement and the plastic hoop strain following unloading are given in Figs. 13 and 14, respectively. The maximum tensile hoop stress at 0.9 and the maximum plastic hoop strain following unloading are 760 MPa and 0.04641 (large strain), respectively. The corresponding small strain value is 4.75%, which is larger than the 4.2% measured permanent structure strain.

Comparison between Maximum Plastic Material Hoop Strain and Permanent Structure Strain

For RCT displacements of 0.5 mm, 0.7 mm, and 0.9 mm, the FEA-calculated maximum plastic hoop strain following unloading is greater than the measured permanent structure strain. For 1.7-mm displacement, the reverse is observed. The same trend was observed for the initial set of yield stresses used in the FEA calculations: 540 MPa (hoop), 513 MPa (axial) and 567 MPa (radial). Results are summarized in Fig. 15 for the current set of yield stresses.

The 0.5-mm-displacement case is particularly interesting with respect to embrittlement. If the sample had failed at 0.5 mm (i.e., experienced >25% load drop), it would have been assessed as brittle (0.9% <2%) based on the ductility screening criterion. Except for very local regions at the loading/support plate cladding inner surfaces, most of the cladding ring experienced no plastic deformation. Only a very small amount of material experienced any plastic deformation. It would be difficult to justify classifying the ring as ductile even if a complete set of mechanical properties were known to allow a good prediction to be made.

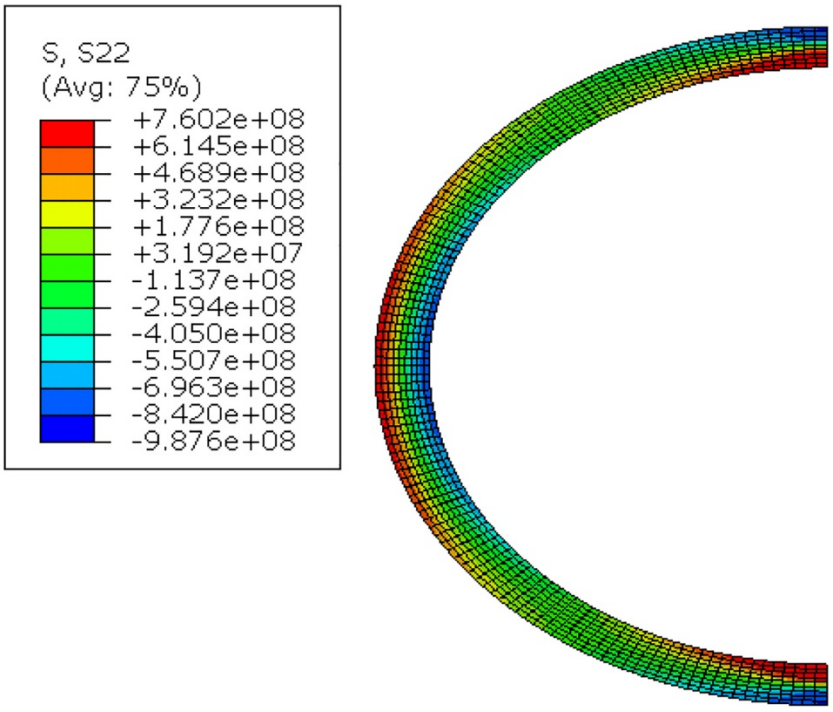

(a)

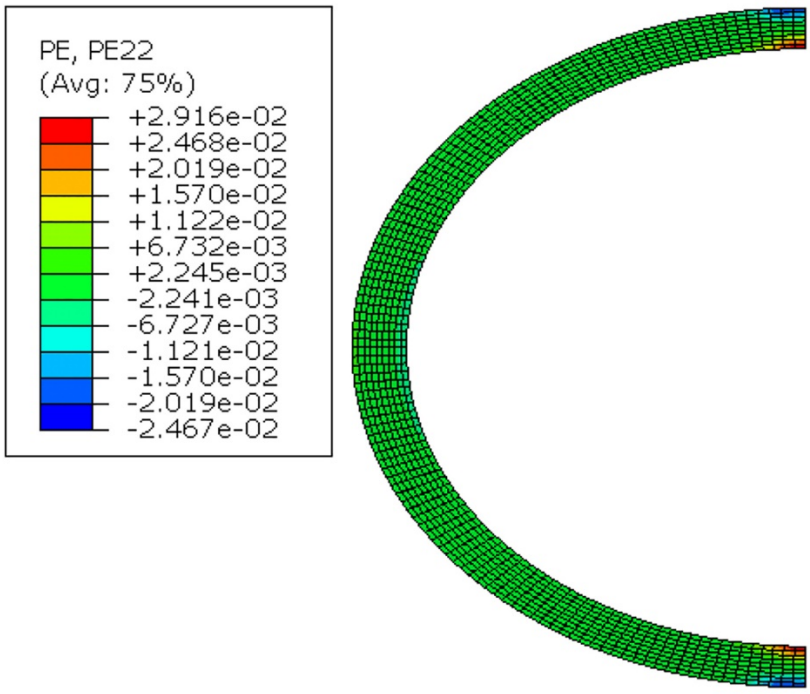

(b)

Figure 10: FEA-predictions for an AF M5® sample subjected to 0.7-mm displacement: (a) hoop stress (Pa) at 0.7-mm displacement and (b) plastic hoop strain after unloading.

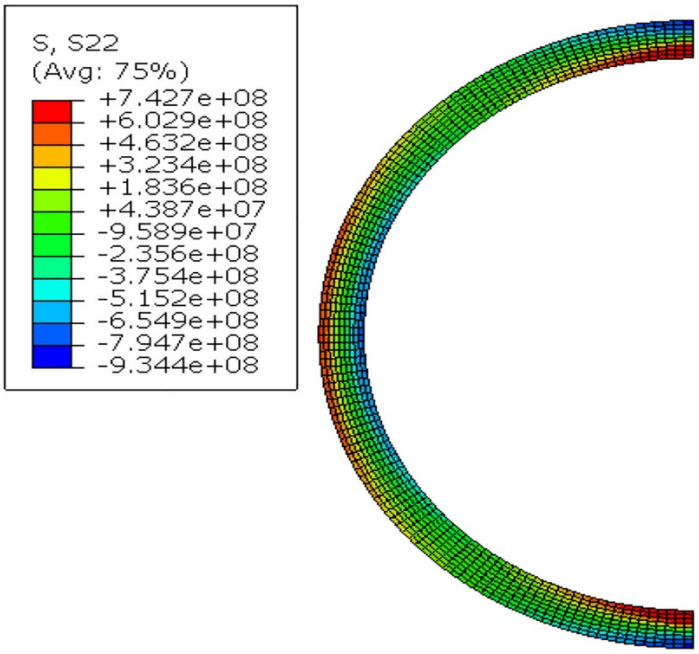

Figure 11: FEA-predicted hoop stress (Pa) distribution at 0.5-mm RCT displacement.

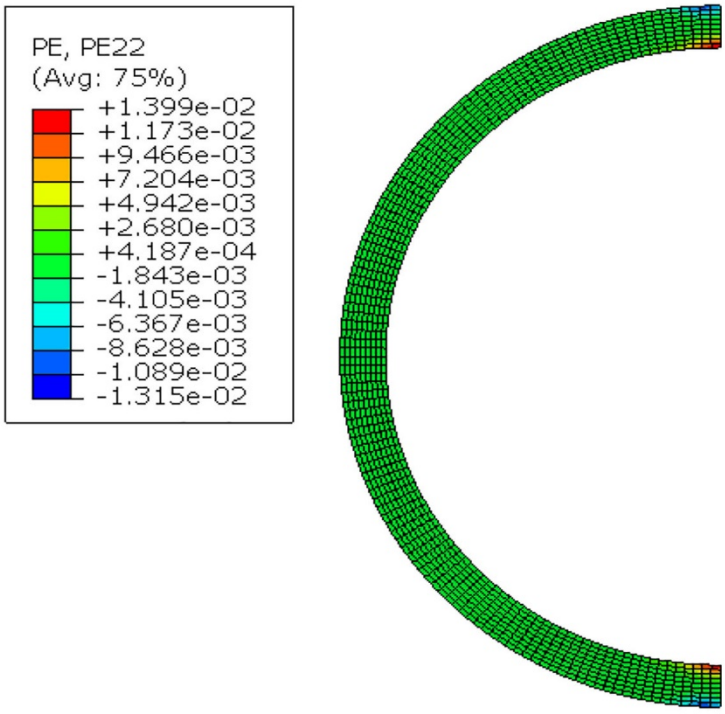

Figure 12: FEA-predicted plastic hoop strain distribution following unloading from 0.5-mm displacement.

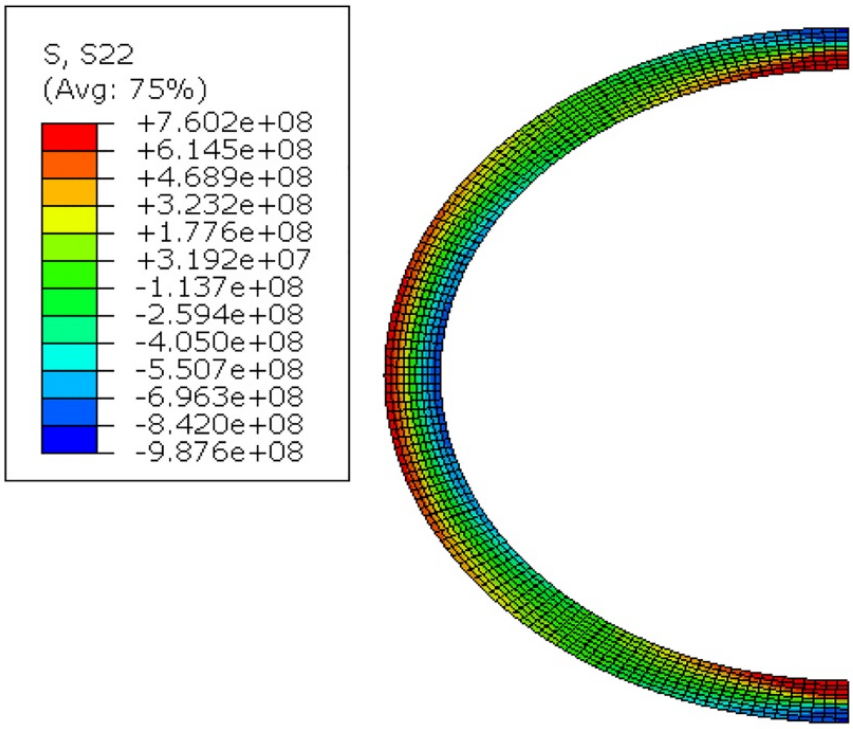

Figure 13: FEA-predicted hoop stress (Pa) distribution at 0.9-mm displacement.

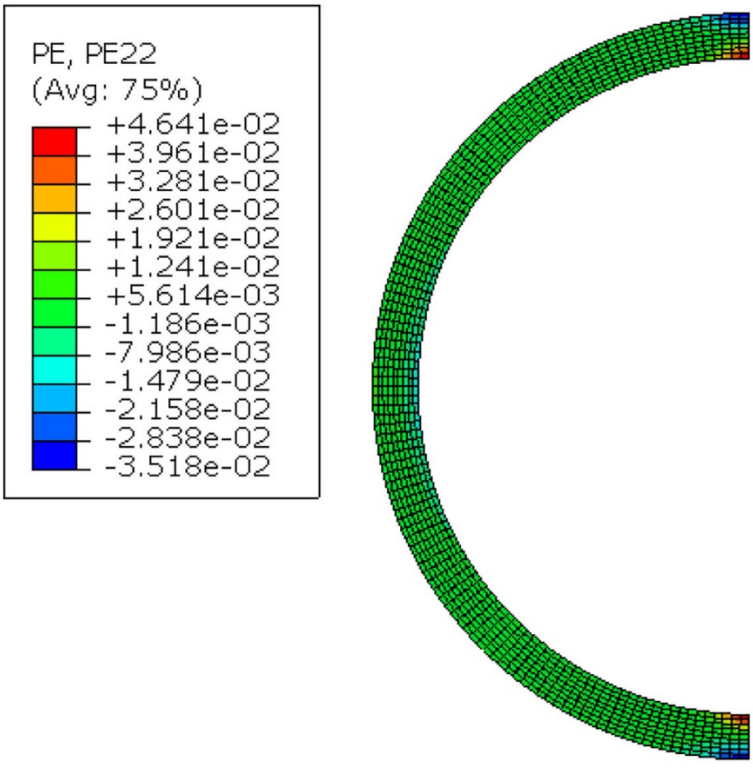

Figure 14: FEA-predicted plastic hoop strain distribution after unloading from 0.9-mm displacement.

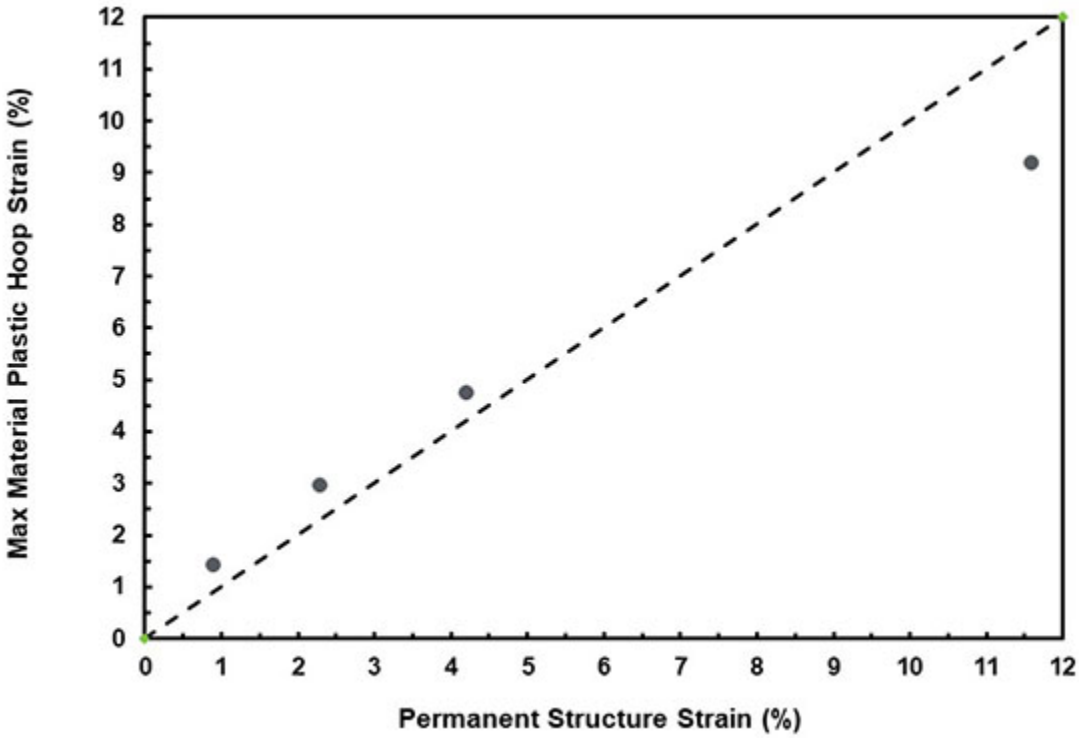

Figure 15: Comparison of measured permanent structure strain and FEA-predicted maximum material plastic hoop strain after unloading AF M5® samples from displacements of 0.5 mm, 0.7 mm, 0.9 mm and 1.7 mm.

4. M5® CLADDING CHARACTERIZATION AND TEST RESULTS

The sibling-pin cladding segments received from ORNL are described in Table 1. Two M5® segments were selected for metallographic examination (MET) and RCTs: (a) 653B (as-irradiated ORNL ID 30AD05 3259 3349) and (b) 654B (FHT ORNL ID 30AE14 3309 3399) [4]. Relative to the fuel column bottom, the mid-spans of these segments were, respectively, at relative axially locations of 0.90 and 0.93 z/L_f, where z is axial elevation and L_f is fuel column length (3678 mm). Both segments were partially under the top grid spacer and at a location where there was a sharp decrease in burnup. Prior to sectioning and defueling samples for ANL and prior to heat-treating 654B, D_o was measured by ORNL [1] at two orientations along the fuel-rod length using linear variable differential transformers (LVDT). ORNL profilometry results are shown in Figs. 16 and 17 for as-irradiated M5® 30AD05 and as-irradiated (pre-FHT) M5® 30AE14 fuel rods, respectively, in axial regions relevant to segments sent to ANL. The estimated average, minimum and maximum values for 30AD05 are 9.41 mm, 9.39 mm, and 9.43 mm, which give 9.41±0.02 mm (note ±0.02 mm is not one standard deviation), within 3259 mm and 3349 mm. Estimated average, minimum, and maximum values for 30AE14 are 9.44 mm, 9.425 mm, and 9.455 mm, which give 9.440±0.015 mm. These measurements are only accurate to the second decimal place.

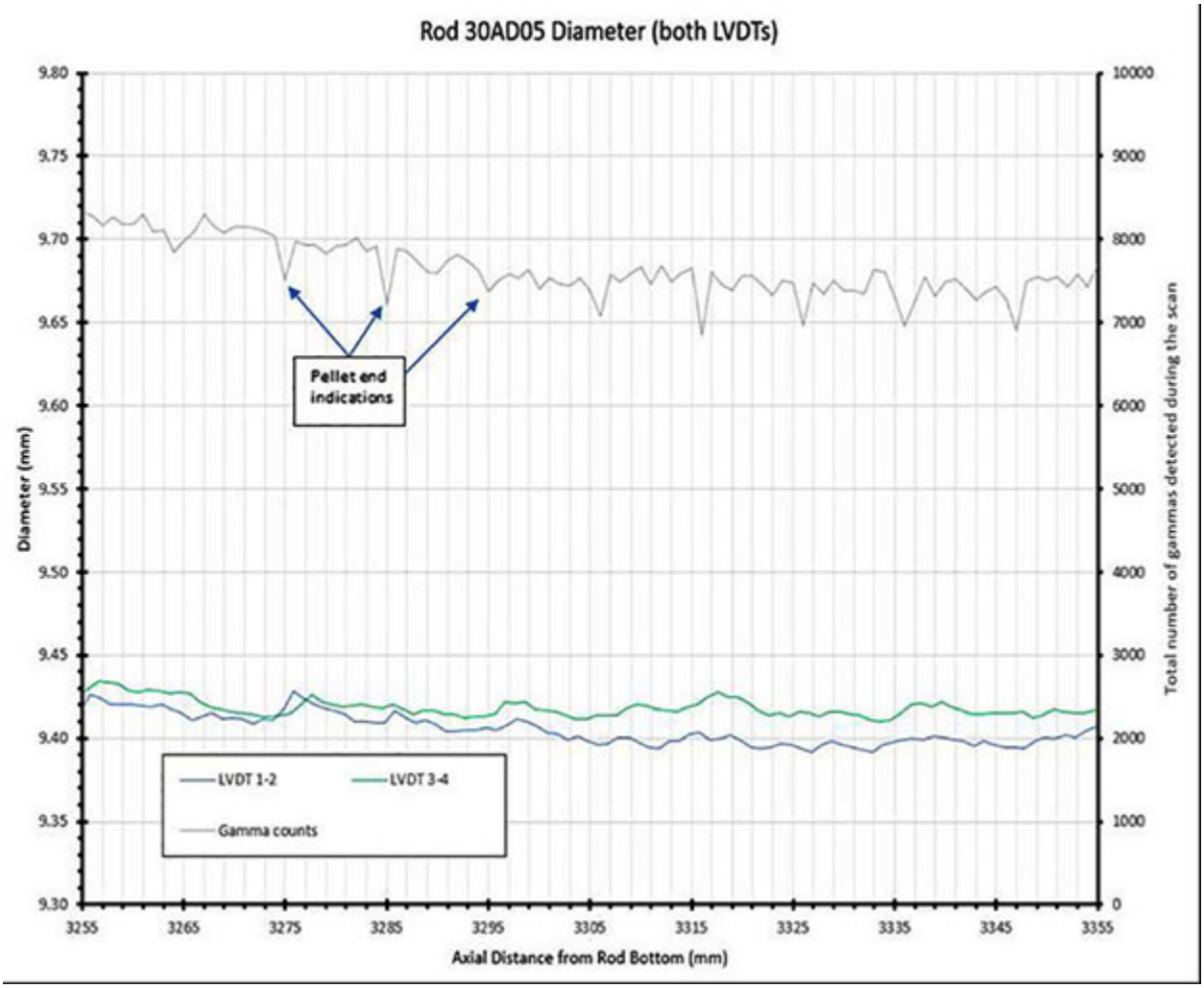

Figure 16: Profilometry results for as-irradiated M5® fuel rod 30AD05 including the 653B segment range of 3259−3349 mm from fuel-rod bottom (*courtesy of ORNL*).

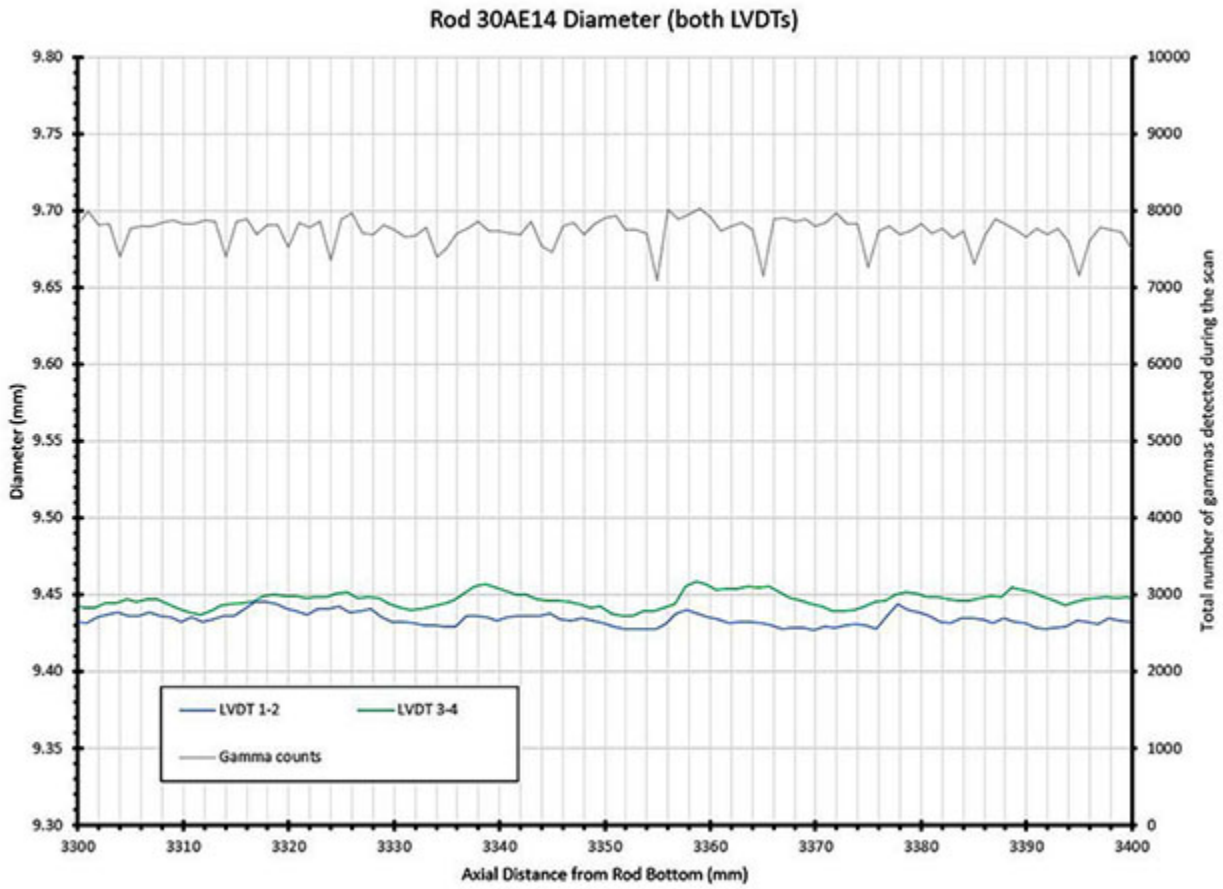

Figure 17: Profilometry results for as-irradiated M5® fuel rod 30AE14 including the 654B segment range of 3309−3399 mm from fuel-rod bottom (*courtesy of ORNL*).

4.1 MET & RCT RESULTS FOR AS-IRRADIATED M5® (653B)

Figure 18 shows the pre-sectioning diagram for segment 653B. Cutting losses and losses due to squaring and deburring resulted in about 5 mm of material loss. Most of the material loss occurred during the squaring process. Figure 19 shows the post-sectioning diagram. The lengths of the eight RCT samples were in the range of 8.05±0.09 mm, where 0.09 mm is one standard deviation. The three samples sectioned for metallographic examination are labeled B1, B6, and B11 with the circle indicating the surface to be examined.

Prior to sectioning, the segment was cleaned with ethanol and D_o was measured at three axial locations (≈25%, ≈50%, and ≈75% from the bottom) and two orientations (0° and 90°) to be 9.38±0.01 mm, which is lower than the 9.41±0.02 mm shown in Fig. 16. Following sectioning, squaring, and deburring of RCT samples, D_o was measured at one-to-three axial locations and two orientations (28 data points) to be 9.41±0.02 mm, which is also the result obtained by averaging the two data sets. This value is in excellent agreement with ORNL profilometry results. Two competing effects that may offset each other in this case are (a) ORNL defueling in nitric acid and ANL ethanol cleaning may reduce fuel rod diameters by removing possible debris and (b) sectioning, squaring and deburring may still leave some flaring (i.e., diameter increase) at the sample ends.

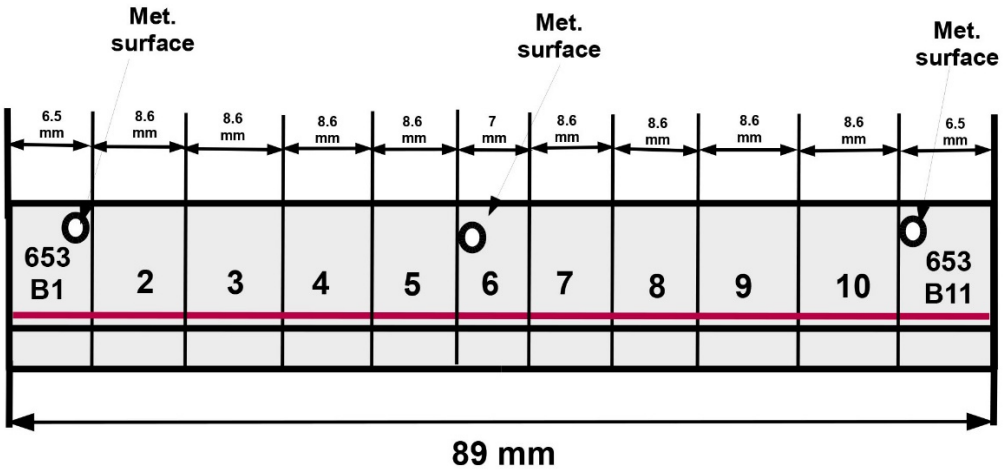

Figure 18: Pre-sectioning diagram for as-irradiated M5® segment 653B. Segment top is to the left.

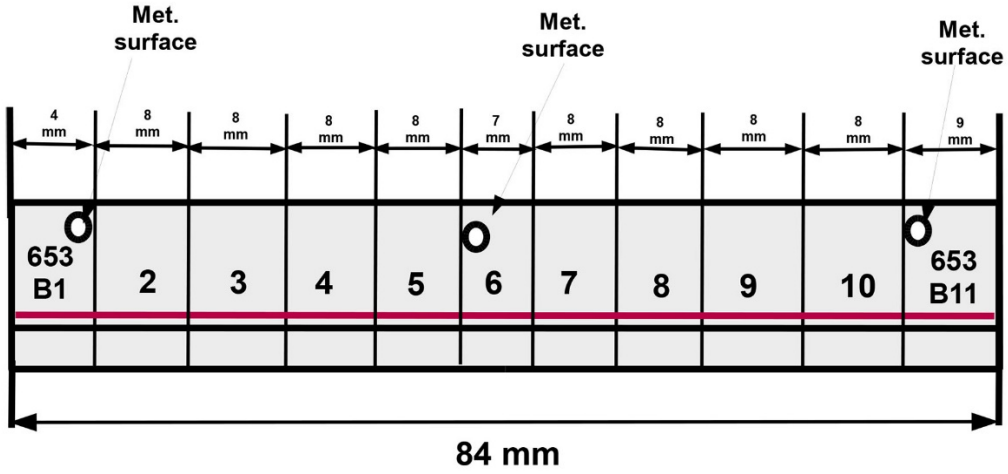

Figure 19: Post-sectioning diagram for as-irradiated M5® segment 653B. Segment top is to the left.

Metallographic Examination Results

Preliminary results for sample B6 have been presented based on metallographic examination of the B6 cross section [6]. Additional results were generated for sample B11. Sample B1, which was too short for grinding and polishing, was not examined. Measured h_{ox} (13±1 µm) and h_m (549±2 µm) were relatively uniform around the circumference and at the two axial locations. Previous ANL data for irradiated M5® indicate a hydrogen content (C_H) of about 90−100 wppm for a 13-µm oxide layer on M5® cladding.

Images at 100X magnification were used to measure h_m and images at 500X were used to measure h_{ox} at about 14 circumferential orientations for each axial location. The grinding process used to prepare MET samples can degrade the oxide layer such that only part of the oxide layer is imaged at individual circumferential locations. Locations for the 14 images/sample were chosen to give the maximum oxide layer thickness.

Both 653B6 and 653B11 surfaces were etched to image hydrides. With the exception of two short radial hydrides (see Figs. 20 and 21), all hydrides were oriented in the circumferential direction.

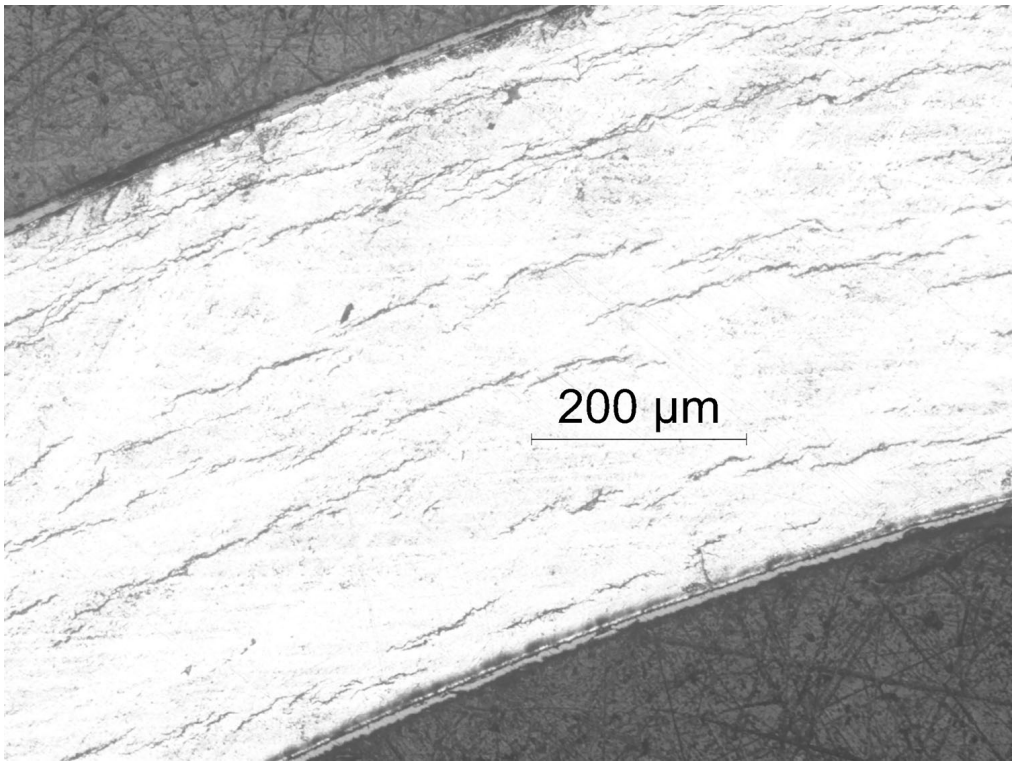

Figure 20: Short radial hydride (7%) observed on the as-irradiated M5® surface of 653B6.

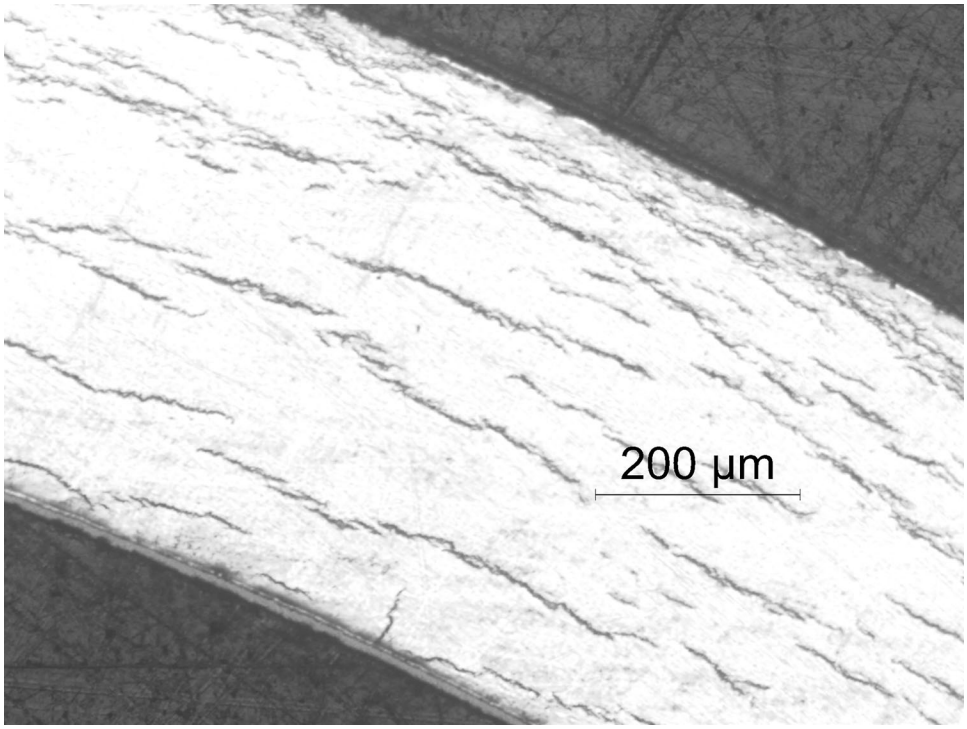

Figure 21: Short radial hydride (10%) observed on the as-irradiated M5® surface of 653B6.

RCT Results

All RCTs were conducted at a displacement rate of 0.05 mm/s to allow stopping of the test at the end of abrupt load drops ≥13% indicative of cracking in the radial direction. At this slow displacement rate, there is ample time to observe the evolution of load with increasing displacement and to unload the sample, which returns the loading rod to its initial position (1 mm above the sample). This is an important feature of the current tests to allow correlation of load drops with cracking extent. In particular, the criterion that >25% load drop implies a single crack extending through >50% of the cladding wall needs further validation. The slow displacement rate also allows the stopping of a test during initial loading if there is a lag during which the loading slope is much lower than the expected loading slope for full loading along the ring axis. Such a loading lag could result from a cutting burr that was not properly removed prior to the RCT or from high spots on the sample for samples with variation in outer diameter. As embrittlement at RT (nominally set to 20°C) was not anticipated, all RCTs were conducted at RT to a preset maximum displacement of 1.7 mm.

Figures 18 and 19 show red and black lines inscribed on the segments for orientation. Usually, the sample is lined up such that the loading plate contacts the sample between these two lines to maintain orientation between pre- and post-RCT MET samples. However, for the 653B RCT samples, the orientation of the samples was random with respect to the red and black lines to investigate the effects of loading direction on cladding ductility.

Figures 22 through 29 show the RCT load-displacement curves for samples B2−B5 and B7-B10, respectively. None of the samples exhibited abrupt load drops greater than a few percent, which indicates that no cracking or only very minor cracking occurred. As such, the maximum offset strain recorded represents a lower bound on ductility.

Samples B2 (Fig. 22) and B3 (Fig. 23) experienced no significant loading lags or load drops and achieved about 10% offset strain. There was also excellent agreement between calculated offset strain and directly measured permanent strain (within 0.6%) indicating that the red unloading line calculated from Eq. 3b is reasonably accurate. Samples B4 (Fig. 24) and B10 (Fig. 29) experienced significant loading lags, which resulted in full-sample displacements <1.7 mm and maximum offset strains of 7.4% and 6.4%, respectively. These tests are valid as ductility screening tests, but the full-sample loading slopes are lower and the difference between maximum offset strain and permanent strain is >1%. Most samples exhibited minor load flattening or load drops in the elastic-plastic displacement transitions. These appeared to have had little impact on the maximum load achieved during these tests. For all eight RCTs, the measured maximum load (P_{max}) normalized to an 8-mm sample length was 534±6 N, which shows excellent consistency and indicates that the load-flattening and small load drops observed had no significant effect on load-bearing capacity. Excluding B4 and B10 because of excessive loading lags, the normalized (to 8-mm length) K_{LM} values were in the range of 846±64 N/mm. The variation was primarily due to lower recorded loading slopes for samples with small and intermediate loading lags.

For the six samples that did not exhibit large loading lags, the average offset strain at the end of loading was 9%, which translates to >9% ductility. Qualitatively, RCT samples with 2% to <4% maximum offset strain have low ductility, samples with 4% to <6% maximum offset strain have intermediate ductility, and samples with ≥6% maximum offset strain have high ductility.

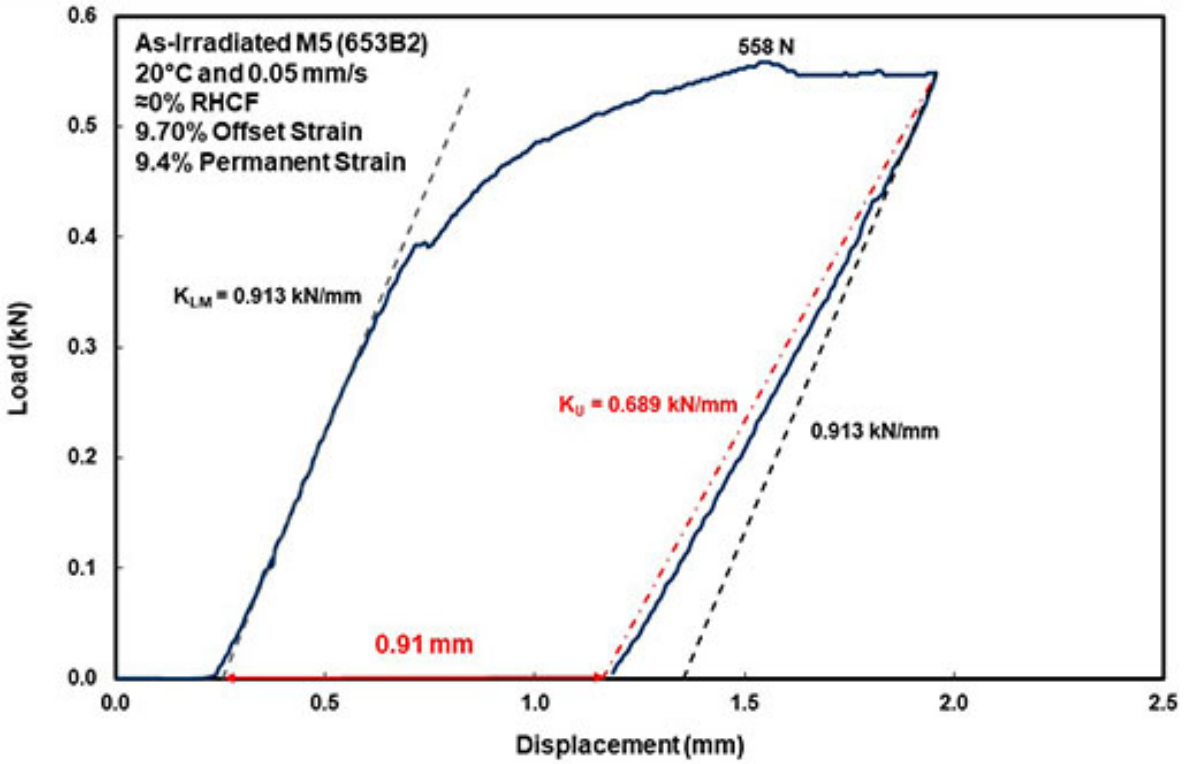

Figure 22: Load-displacement curve for RCT sample 653B2.

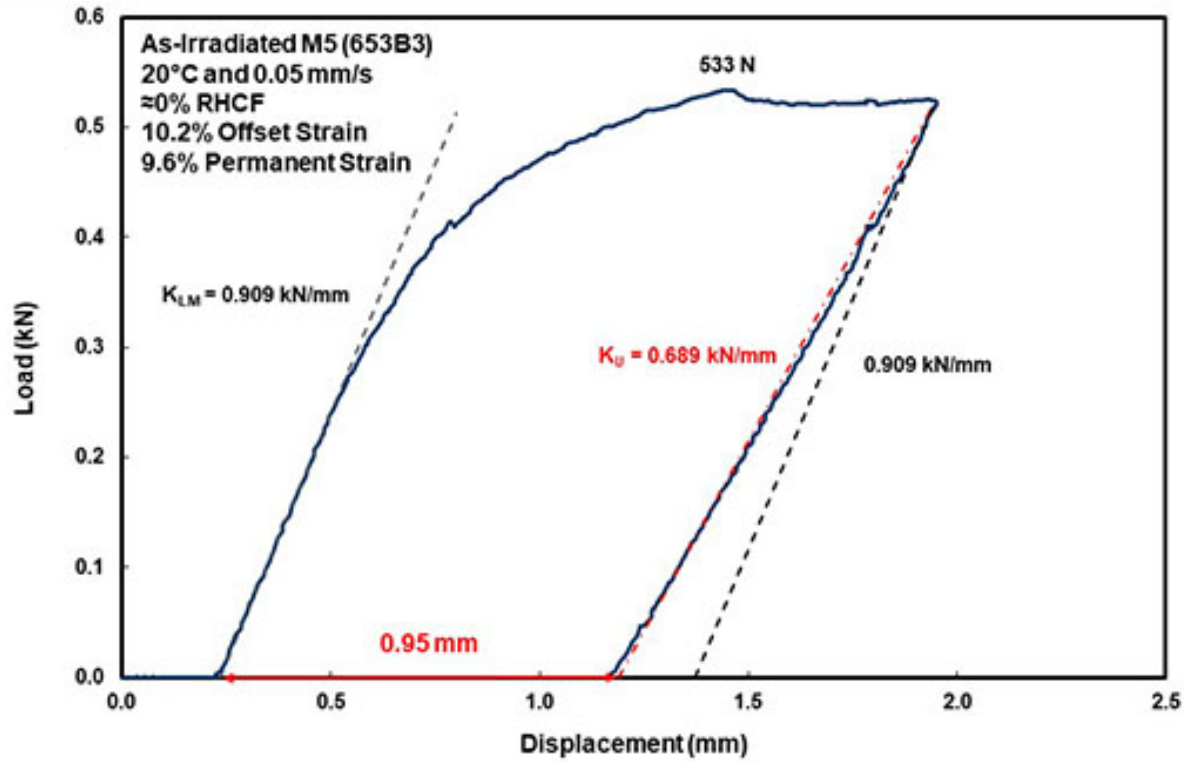

Figure 23: Load-displacement curve for RCT sample 653B3.

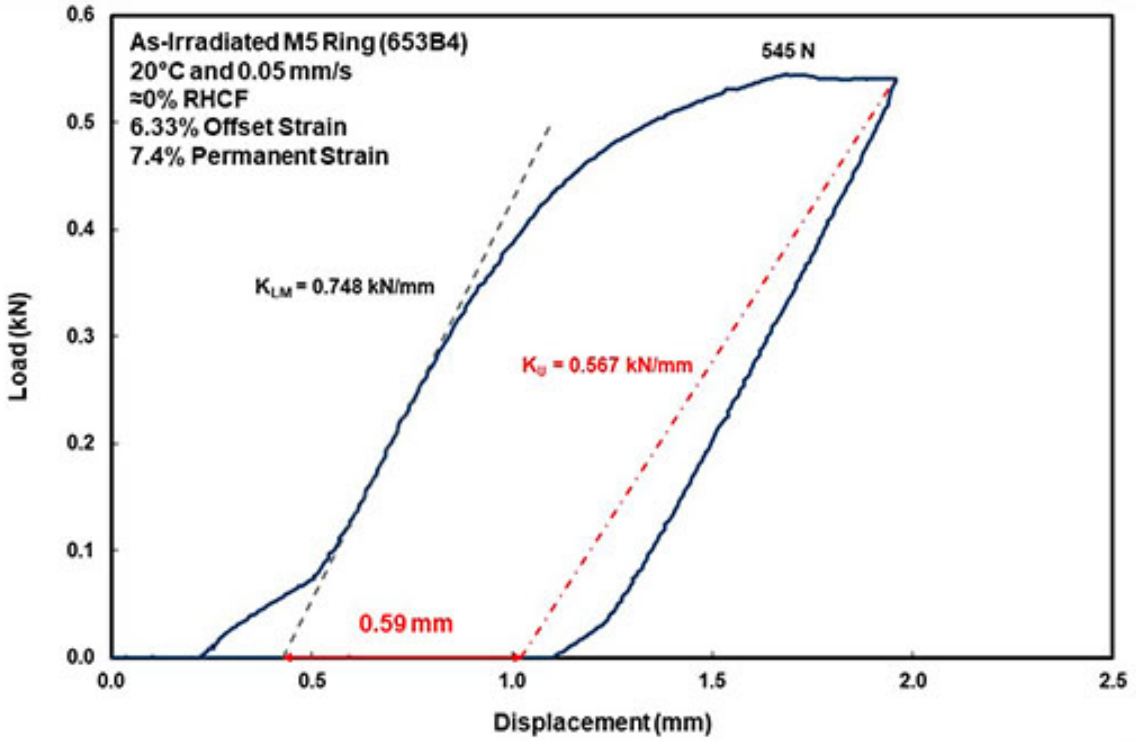

Figure 24: Load-displacement curve for RCT sample 653B4.

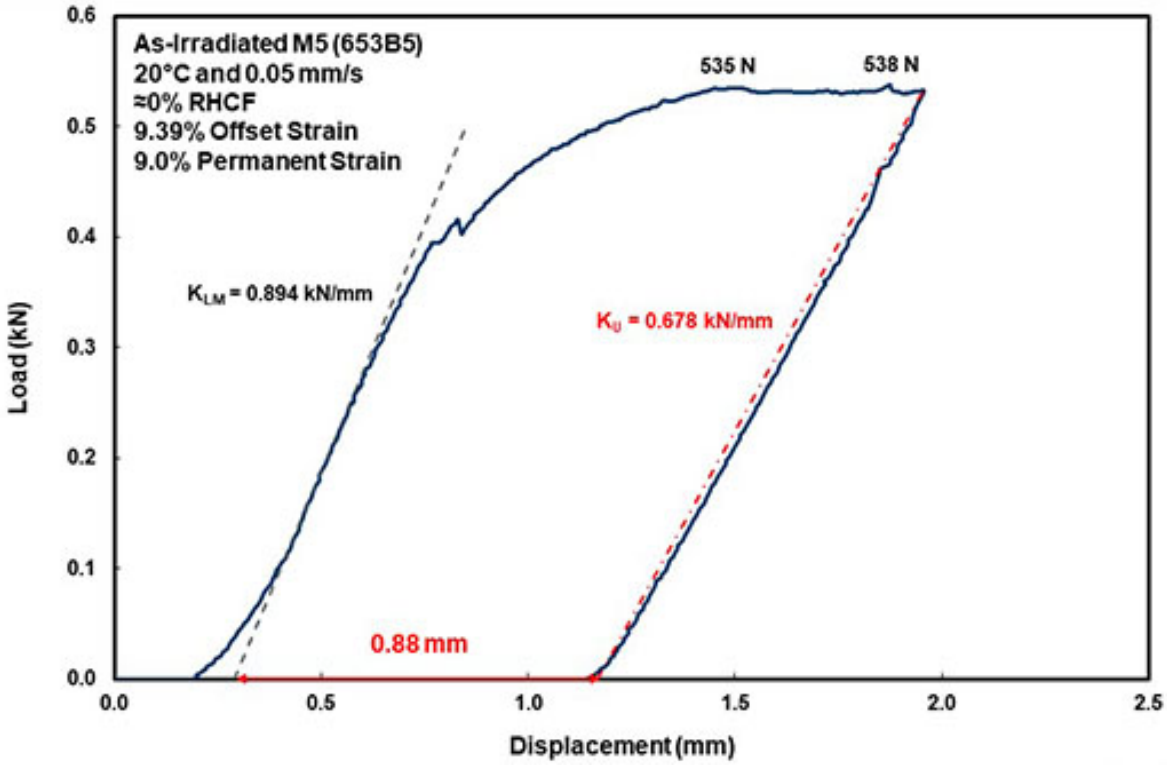

Figure 25: Load-displacement curve for RCT sample 653B5.

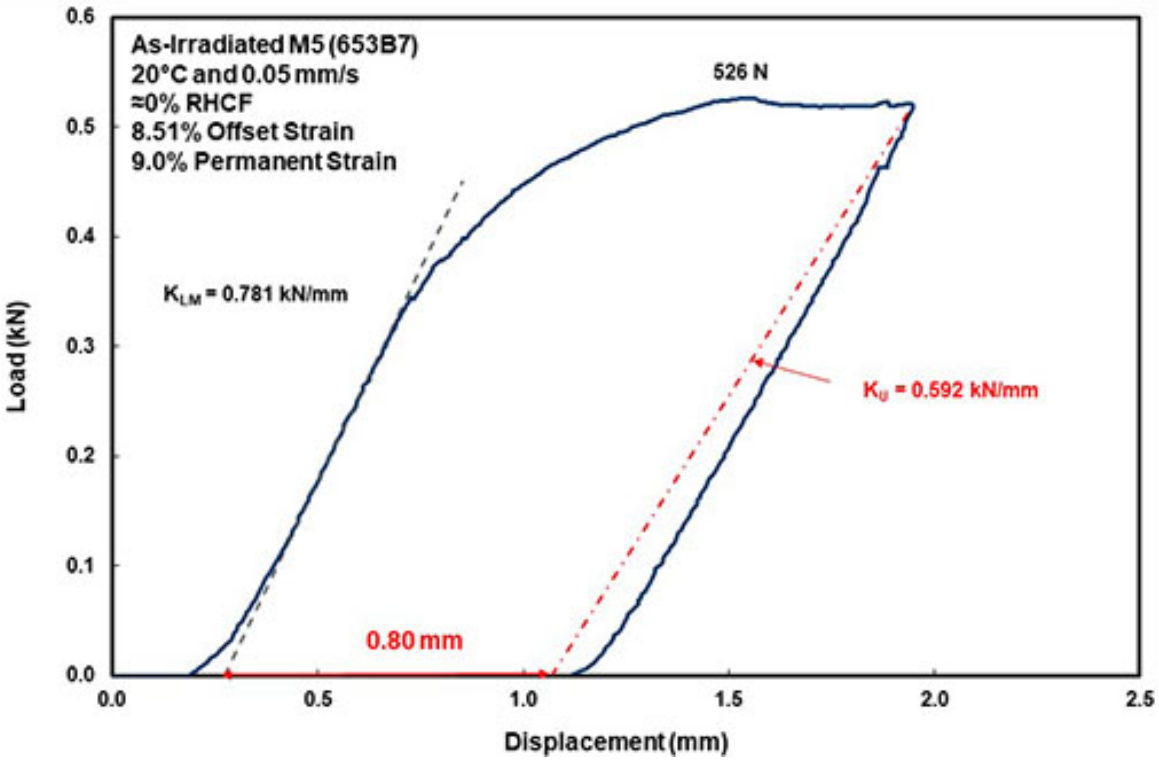

Figure 26: Load-displacement curve for RCT sample 653B7.

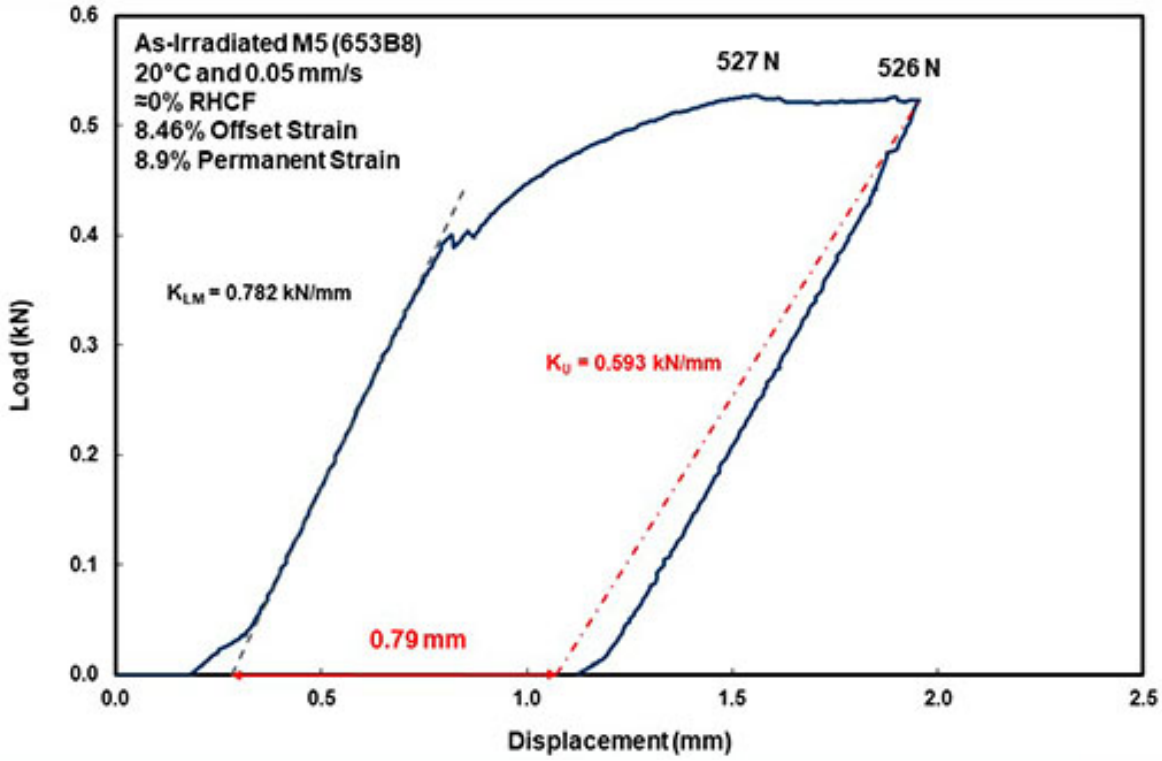

Figure 27: Load-displacement curve for RCT sample 653B8.

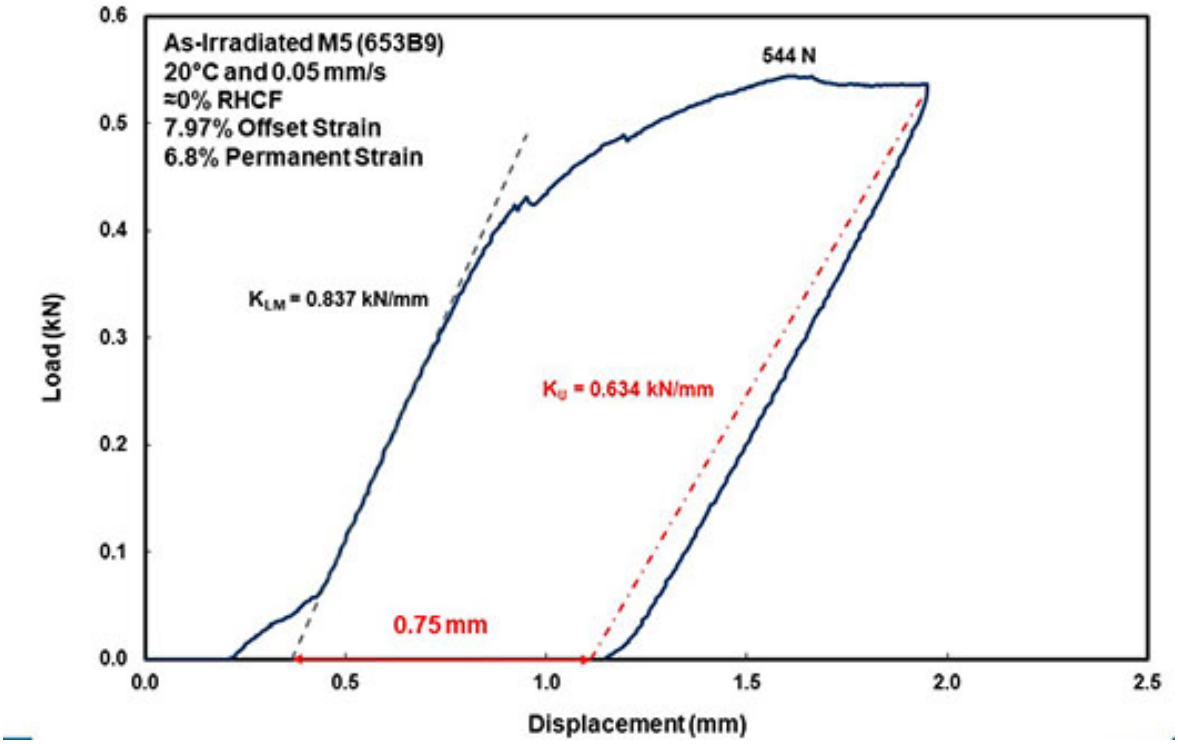

Figure 28: Load-displacement curve for RCT sample 653B9.

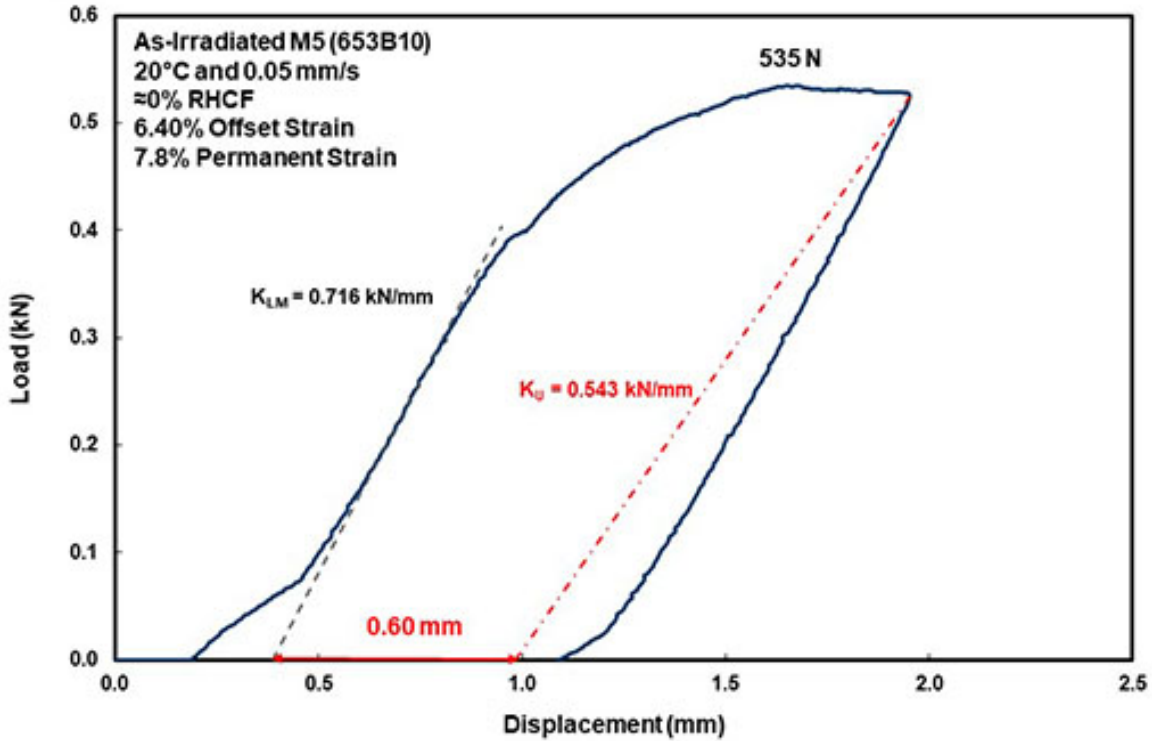

Figure 29: Load-displacement curve for RCT sample 653B10.

4.2 MET & RCT RESULTS FOR HEAT-TREATED M5® (654B)

Segment 654B is from fuel rod 30AE14 at an axial location approximately 3309−3399 mm from the bottom of the fuel rod. During FHT, control of the top heater was lost during the heating ramp such that 654B was heated initially to a peak temperature of 485°C. During the 8-hour hold time, the temperature coasted down to 401°C as the cooling was initiated at an average rate of 3.6°C/h. For M5® cladding with about 70−100 wppm hydrogen, full dissolution of hydrogen would occur rapidly at about 300−330°C, respectively. From the perspective of radial hydride dissolution and precipitation, the overheating should have had no significant effect assuming that partial annealing of irradiation damage did not occur during the 401−485°C phase of the FHT.

Figure 30 shows the pre-sectioning diagram for segment 654B. Cutting losses and losses due to squaring and deburring resulted in 8 mm of material loss. Figure 31 shows the post-sectioning diagram. Rings B3 and B7, respectively, exhibited load drops of 29% at high displacement and 9% at low displacement. As such they were subsectioned for metallographic examination to investigate crack depth vs. load drop. The RCT sample lengths were in the range of 7.88±0.23 mm, where 0.23 mm is one standard deviation.

Prior to sectioning, the cladding outer diameter was measured at three axial locations and two orientations per location. These measurements indicated a uniform cladding D_o = 9.41±0.00 mm (one reading was 9.42 mm). Prior to conducting the RCTs, D_o was measured at two orientations at the sample mid-span and at the RCT sample ends by another worker. On the basis of the 48 data points generated for RCT samples, D_o = 9.42±0.01 mm, which is lower than the 9.440±0.015 mm measured by ORNL before fuel-rod sectioning. The two data sets do overlap somewhat at ≈9.43 mm.

Metallographic examination of as-polished (not etched) surfaces of B1, B6, and B11 gave 11±1 µm for h_{ox} and 570±5 µm for h_m. On the basis of irradiated M5® previously characterized by ANL, C_H is estimated to be 80−90 wppm. The ratio of R_{mi} and h_{ox} is used in Eq. 1 to determine the wall-average hoop stress, along with the internal pressure at 401°C at cooling initiation and the external pressure (assumed to be 0.1 MPa). The internal pressure was measured by ORNL at the ambient hot-cell area temperature and results were extrapolated to 25°C to give 3.2 MPa. At 401°C, the internal pressure increased to 7.24 MPa. The geometric factor R_{mi}/h_{ox} and the average hoop stress were calculated with D_o = 9.41 mm and 9.42 mm. The average hoop stresses were 51.5±0.5 MPa for 9.41-mm and 51.6±0.6 MPa for 9.42-mm D_o, respectively. Thus, the 0.01-mm change in D_o had a negligible effect on results. Given the measurement uncertainties, the wall-average hoop stress was 52±1 MPa at 401°C at FHT cooling initiation.

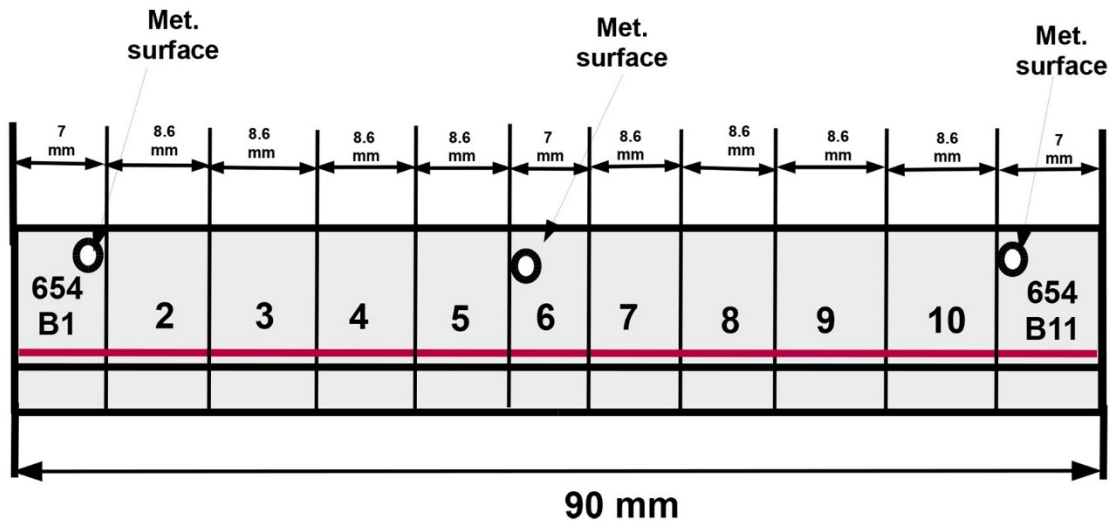

Figure 30: Pre-sectioning diagram for heat-treated M5® segment 654B. Top of segment is to the left.

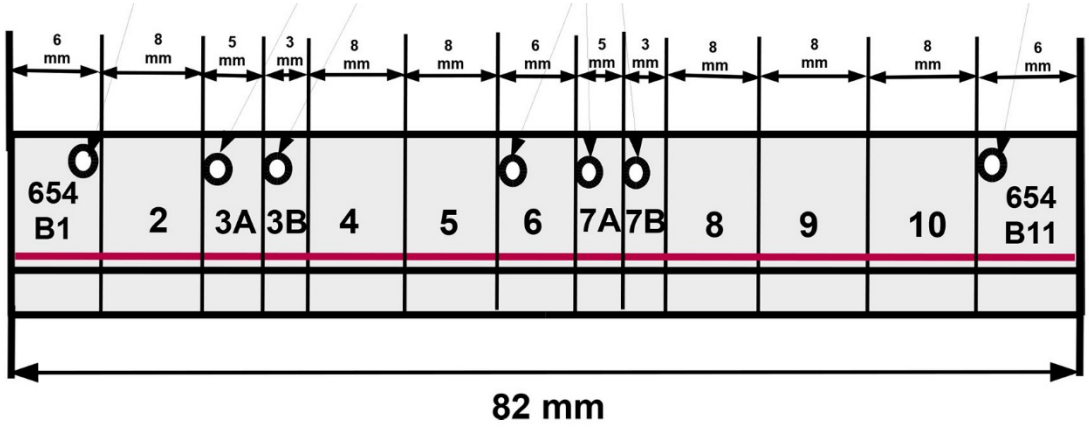

Figure 31: Post-sectioning diagram for heat-treated M5® segment 654B. Top of segment is to the left.

Metallographic Examination Results

Results for 654B6 and 654B1 were presented previously [6]. Additional work conducted during the current period included metallographic examination of sample B11, as well post-RCT rings B3A and B3B.

The 654B6, 646B1, and 646B11 surfaces, along with 646B3A and 646B3B surfaces, were etched and imaged at 100X− and 200X−magnification. For the B6 surface, the 20 circumferential locations imaged were ones containing radial hydrides. The average and maximum RHCF values for B6 were 22±15% and 59%, respectively. The average RHCF is an upper bound of what would have been determined from images covering the full surface. For the remaining MET surfaces, the RHCF was based on images covering all or most of the surface area. The RHCF values were determined to be 18±10% with 49% maximum for surface B1, 13±8% with 37% maximum for surface B11, 19±12% with 60% maximum for surface B3A, and 21±14% with 54% maximum for surface B3B. Overall for FHT segment 656B, the RHCF was 18±12% with a maximum value of 60%. With the possible exception of the B11 surface at which radial hydrides were rather faint, the agreement in RHCF values for the other four surfaces examined was quite good.

The determination of RHCF allows for ≤5−µm gaps in the radial direction between radial hydrides in the assessment of continuity [9−10]. It is assumed that a crack growing along a radial hydride can propagate rapidly through a 5-µm gap to the next radial hydride. It is possible, as suggested by the MET for cracked RCT sample 654B3, that such a crack can propagate rapidly through gaps >5 µm. The following images at 100X and 200X magnification show gaps of ≤5 µm and >5 µm between relatively short radial hydrides.

Figures 32−33 show 100X- and 200X-magnification images of the circumferential location at which the maximum radial hydride was observed for surface 654B6. The RHCF was assessed to be 59%. However, as observed in the 200X image (Fig. 33), the continuity of the radial hydrides is questionable because of the radial gaps between hydrides. The radial hydride shown in Fig. 34 appears longer than the radial hydride in Fig. 32. However, based on the 200X-magnification image (Fig. 35), the hydride contains two gaps >5 µm. If a crack could rapidly grow through these gaps, the RHCF could be as high as 80%. Figures 36 and 37 show, respectively, 100X- and 200X- magnification images of the 654B1 surface at about 2:45 o'clock. The radial hydride to the right of the three radial hydrides appears to be as long as 67% of the cladding wall, while the radial hydride in the center is only 49% of the cladding wall. The 200X image, which includes both of these hydrides, shows radial gaps >5 µm for the hydride on the right. Depending on the limiting gap size for continuity, the RHCF could be between 49% and 67%. Additional metallographic images of the 654B surfaces are shown in Ref. 6.

Previously, M5® cladding samples were heat-treated at peak conditions prior to 5°C/h cooling of 400°C/90-MPa, 350°C/89-MPa, 400°C/111-MPa, and 400°C/142-MPa [12−14]. To better appreciate the combined effects of hoop stress and hydrogen content, it is useful to tabulate results and to include the hoop stress [σ_θ (T_P)] at the hydride precipitation-initiation temperature (T_P). T_P is assumed to be 65°C lower [15] than the dissolution temperature (T_D), which increases as the hydrogen content increases [16]. The results in Table 2 show a consistent pattern for RHCF, which increases as σ_θ (T_P) increases: 37±17% for 67 MPa, 44±18% for 74 MPa, 54±16% for 94 MPa, and 62±17% for 127 MPa. These results are also plotted in Fig. 38. The hydrogen content available for precipitation is also an important factor in the effective lengths of radial hydrides. It is important to recall that radial-hydride discontinuities in M5® are larger in the axial direction than they are in higher-hydrogen-content ZIRLO®. Although radial hydrides as long as 100% of the wall have been observed on a surface in irradiated and heat-treated M5®, all RCT samples for segments listed in Table 2 were ductile at 90°C with some exhibiting brittle behavior at 60°C. These results, along with MET results following regrinding depths of 0.5 mm and 0.1 mm, support the postulation that axial continuity of radial hydrides is poor in low-hydrogen-content M5®.

Sibling-pin M5® segment 654B, which was from a fuel rod subjected to FHT at 401°C/52-MPa, is expected to have a precipitation-initiation hoop stress of only about 40 MPa. For this RXA alloy, some radial hydrides are likely to precipitate at such a low stress, but the radial hydrides are not expected to be as continuous in the radial and axial directions as they would be at higher precipitation-initiation hoop stresses (67−127 MPa) and higher hydrogen contents.

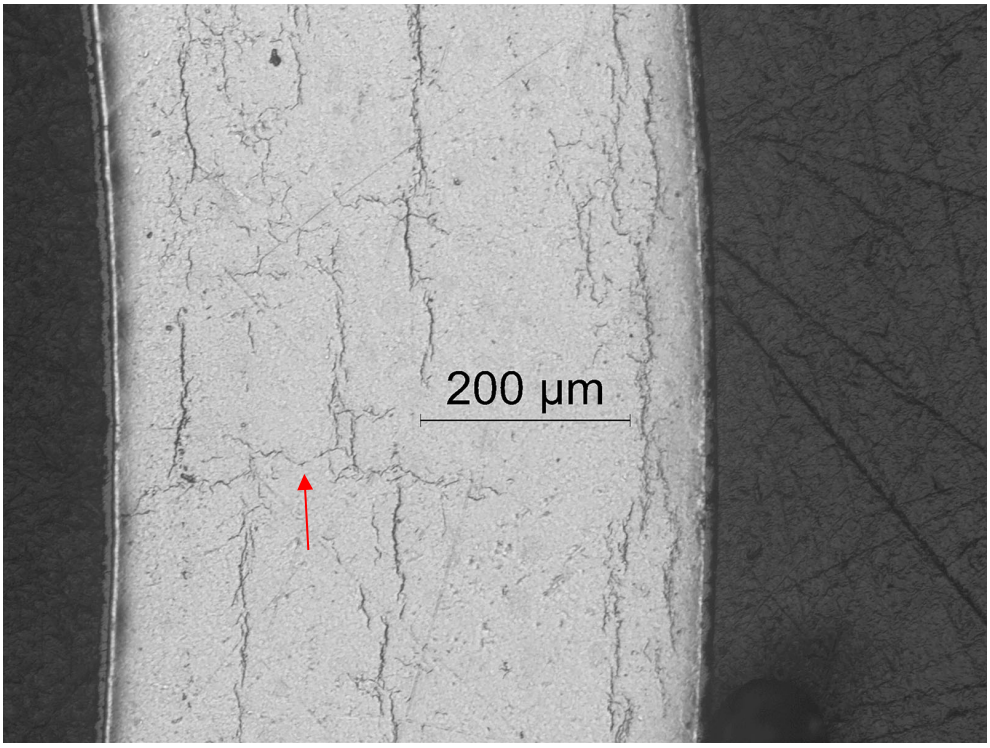

Figure 32: 100X image of the longest radial hydride (59% RHCF) observed at the 3 o'clock orientation of M5® surface 654B6 located at ≈3357 mm from the bottom of FHT fuel rod 30AE14.

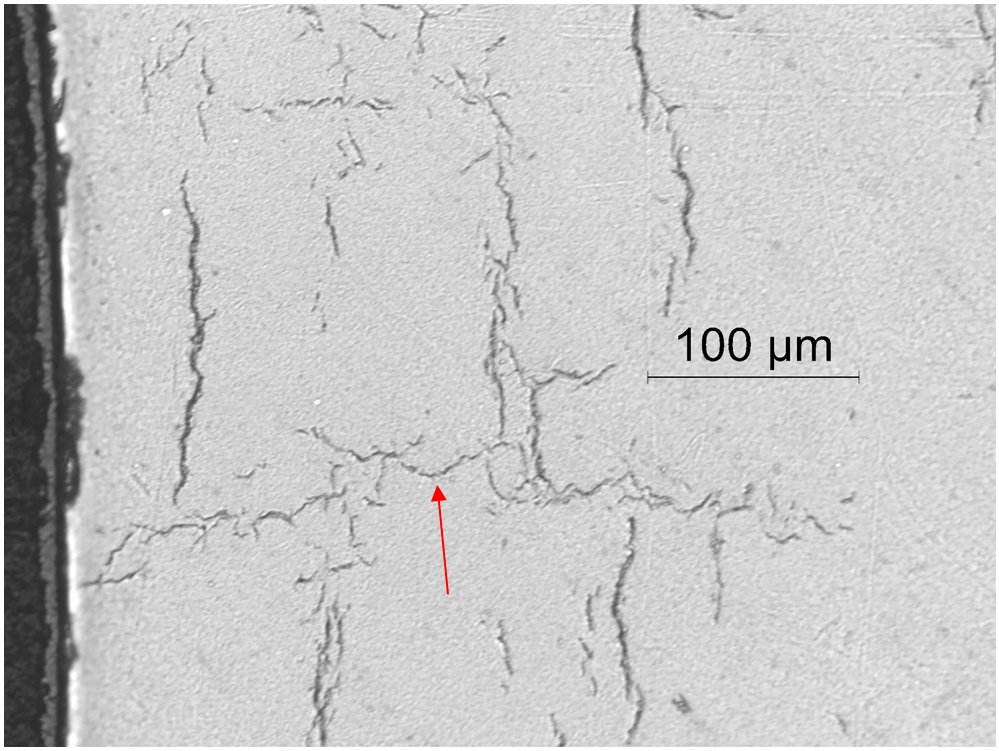

Figure 33: 200X image of the longest radial hydride (59% RHCF) observed at the 3 o'clock orientation of M5® surface 654B6 located at ≈3357 mm from the bottom of FHT fuel rod 30AE14.

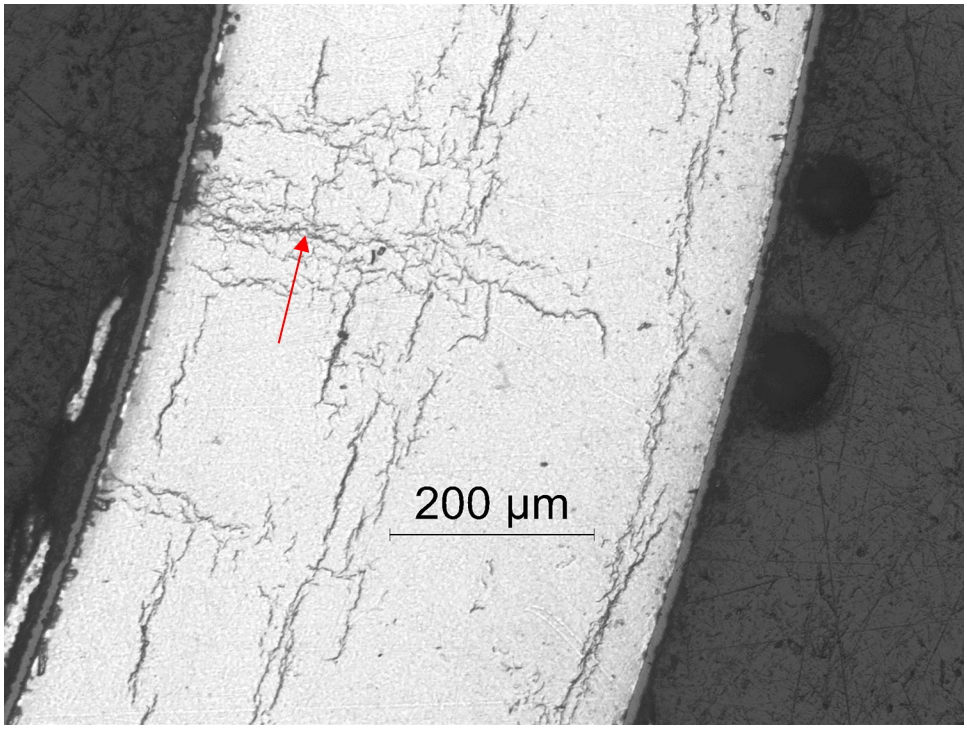

Figure 34: 100X image of a long radial hydride (40% RHCF) observed at the 3:30 o'clock orientation of M5® surface 654B6 located at ≈3357 mm from the bottom of FHT fuel rod 30AE14.

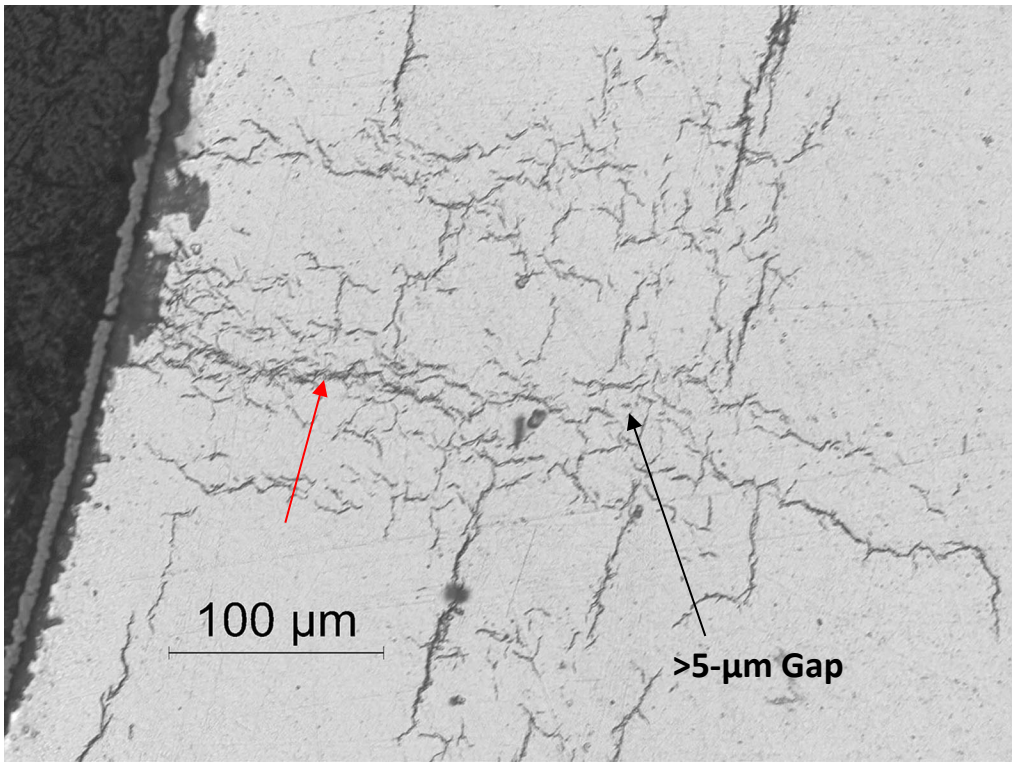

Figure 35: 200X image of a long radial hydride (40% RHCF) observed at the 3:30 o'clock orientation of M5® surface 654B6 located at ≈3357 mm from the bottom of FHT fuel rod 30AE14.

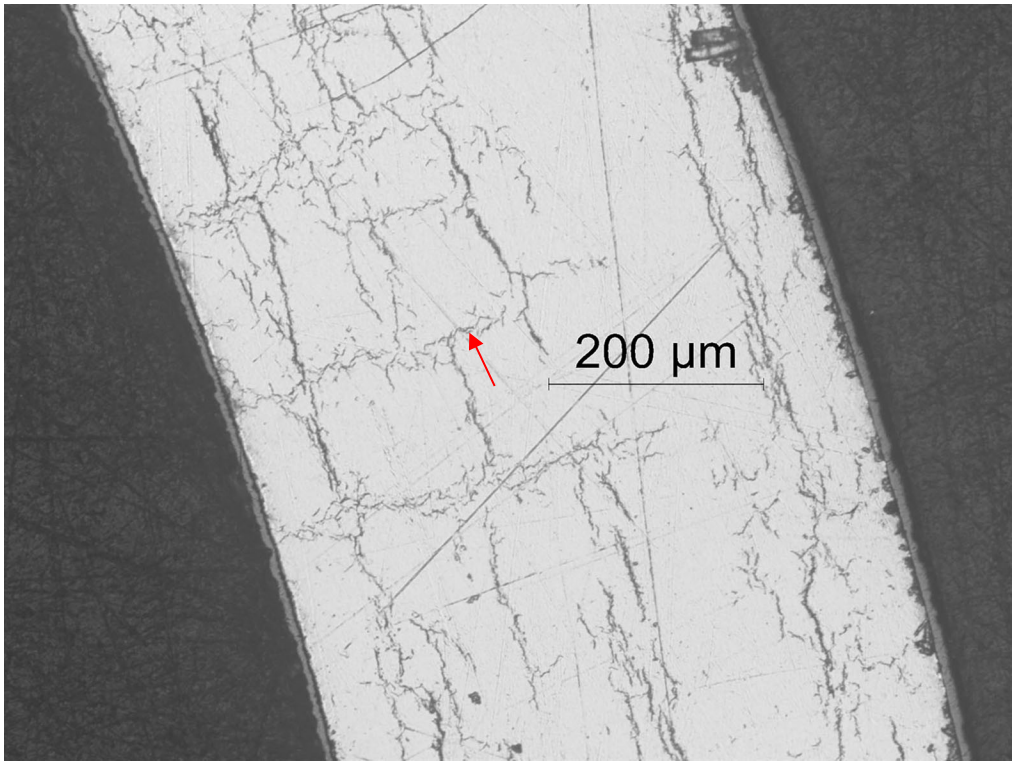

Figure 36: 100X image of a long radial hydride (49% RHCF) observed at the 2:45 o'clock orientation of M5® surface 654B1 located at ≈3392 mm from the bottom of FHT fuel rod 30AE14.

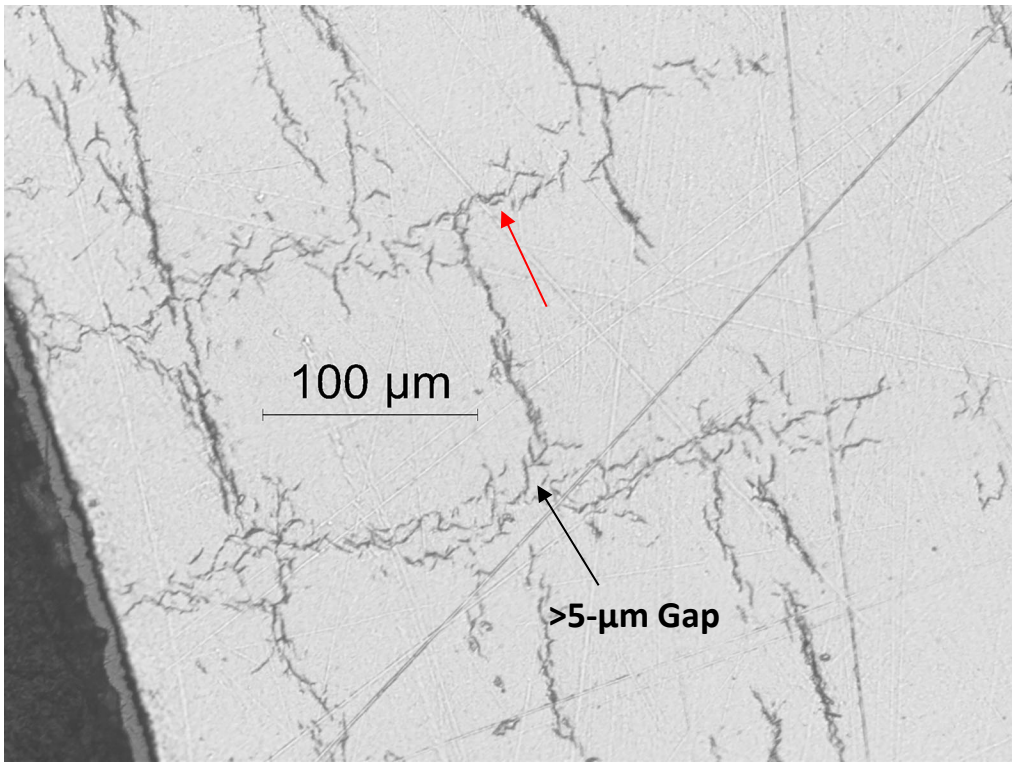

Figure 37: 200X image of a long radial hydride (49% RHCF) observed at the 2:45 o'clock orientation of M5® surface 654B1 located at ≈3392 mm from the bottom of FHT fuel rod 30AE14.

Table 2 Summary of radial hydride results and parameters influencing radial hydride precipitation in irradiated M5® cladding segments following radial hydride treatment.

Parameter	FHT Rod 30AE14 654B	ANL Rodlet 651E3	ANL Rodlet 652F2	ANL Rodlet 651E5	ANL Rodlet 645D
Average Burnup, GWd/MTU	54	68	70	68	63
h_{ox}, µm	11±1	9±1	11±1	8±1	13±0
C_H, wppm	TBD	58±15	80±7	72±10	94±6
PCT, °C	401	400	350	400	400
T_D, °C	TBD	290	315	307	206±5
T_P, °C	TBD	335	285	285	329
σ_θ(PCT), MPa	52	90	89	111	142
$\sigma_\theta(T_P)$, MPa	TBD	67	74	94	127
Average RHCF, %	18±12	37±17	44±18	54±16	62±17
Maximum RHCF, %	60	96	100	100	99
# of Data Points	65	95	204	35	36

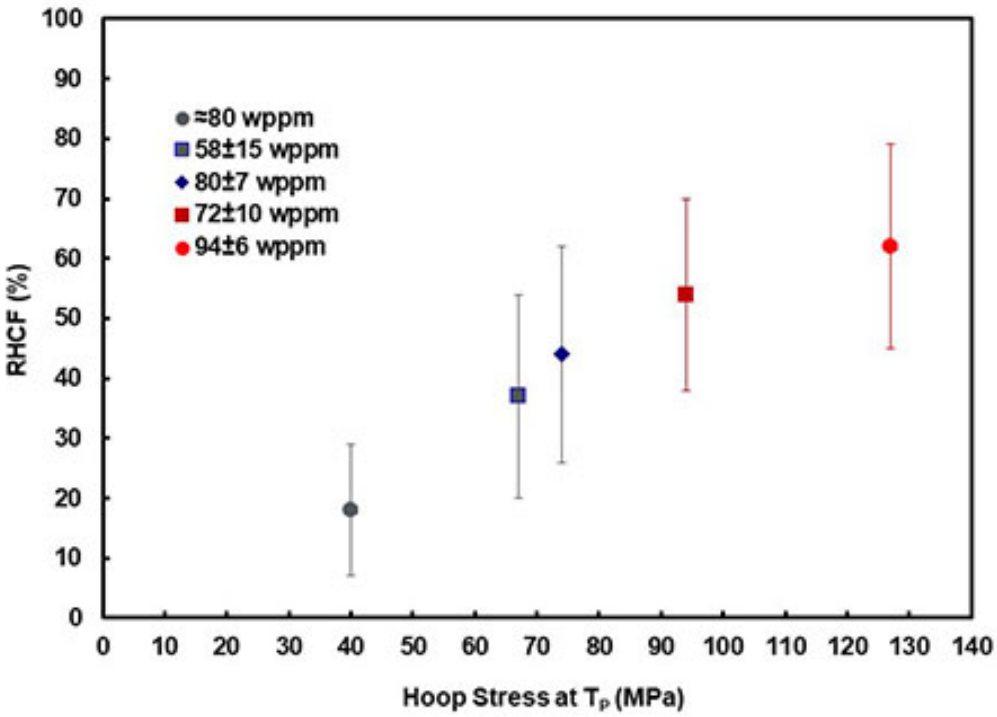

Figure 38: RHCF in irradiated M5® cladding versus hoop stress at the precipitation initiation temperature (T_P).

RCT Results

All 654B RCT samples were tested at RT and 0.05 mm/s to a maximum sample displacement of 1.7 mm. The pre-test protocol was modified somewhat to minimize loading lag at the initiation of contact. This protocol calls for lowering the loading rod manually until about 20 N of load is recorded. The loading rod is then retracted 1 mm from this contact point and the displacement is set to be 2.7 mm (1 mm free displacement and 1.7 mm contact displacement). However, several of the 653B samples had significant high spots in outer diameter such that contact was established locally along the length of the sample. For 654B samples with high contact points detected by the Instron LVDT, the load was increased to 40 N to establish the contact point. This step helped to reduce the initial loading lag and to ensure that most of the sample was subjected to 1.7-mm displacement.

Figures 39 through 46 show the RCT load-displacement curves for samples B2−B5 and B7-B10, respectively. With the exception of 654B3, which had a load drop of 29% at 7.8% offset strain, offset strains were ≈10% and samples experienced no abrupt load drops or minor load drops ≤9%. As such the ductility was assessed to be ≥10% for seven of the samples and 7.8% for one of the samples. Thus, the ductility of this material was assessed as high.

Sample B2 (Fig. 39), which was only 7.53-mm long, achieved the expected normalized P_{max} and K_{LM}. No load drops indicative of cracking were observed. The unloading slope (red dashed line in Fig. 39), which is calculated using Eq. 3b, resulted in excellent agreement between the offset strain (10.6%) and the permanent strain (10.2%). Results for samples B4 (Fig. 41), B5 (Fig. 42), B8 (Fig. 44), B9 (Fig. 45) and B10 (Fig. 46) were similar to the sample B2 results in terms of normalized P_{max}, normalized K_{LM}, and offset strain agreement with permanent strain.

Sample B7 (Fig. 43) experienced an abrupt load drop of 9% in the transition between elastic deformation and elastic-plastic deformation close to P_{max}. However, the load-bearing capacity of the cracked sample was relatively high, which is consistent with a minor crack from the 9% load drop. To assure this is the case, the ring will be subjected to metallographic examination to determine crack depth for a 9% load drop. Excluding the P_{max} for this sample due to the low-deformation load drop, the normalized P_{max} (529±7 N) was relatively consistent. The normalized K_{LM} (905±23 N/mm) for all samples was also consistent. The comparison between normalized P_{max} for as-irradiated 653B samples (534±6 N) and for heat-treated 654B sample (529±7 N) suggests that the overheating to 485°C during FHT did not result in partial annealing.

Sample B3 (Fig. 40) experienced a significant load drop (29%) at 7.8% offset strain just prior to unloading. What appears as a second load drop is really due to unloading. The intent was to stop the test at the bottom of the 29% load drop. However, the load drop was mistaken for unloading and the test was not terminated until just after unloading began. The small displacement following the 29% load drop would have no effect on the crack or cracks associated with the load drop. The “failure” criterion established in Section 2 is that >25% load drop indicates >50% wall cracking. Metallographic examination was performed at one end of 654B3 (A) and at approximately the mid-span (B). Figures 47 and 48 show the 100X-and 200X-magnification images at the 12 o’clock orientation for end surface 6543A. The single crack observed is 60% of the wall thickness, which is consistent with the criterion. Figures 49 (100X) and 50 (200X) show a 54% wall crack at the 12 o’clock sample mid-span. Figures 51 (100X) and 52 (200X) show a secondary crack at the mid-span ≈6 o’clock orientation that is also about 54% of the cladding wall. Based on the radial hydrides observed to the left and right of the cracks in the 200X images, it appears as if cracks can grow rapidly along radial hydrides with a couple of gaps >5 μm.

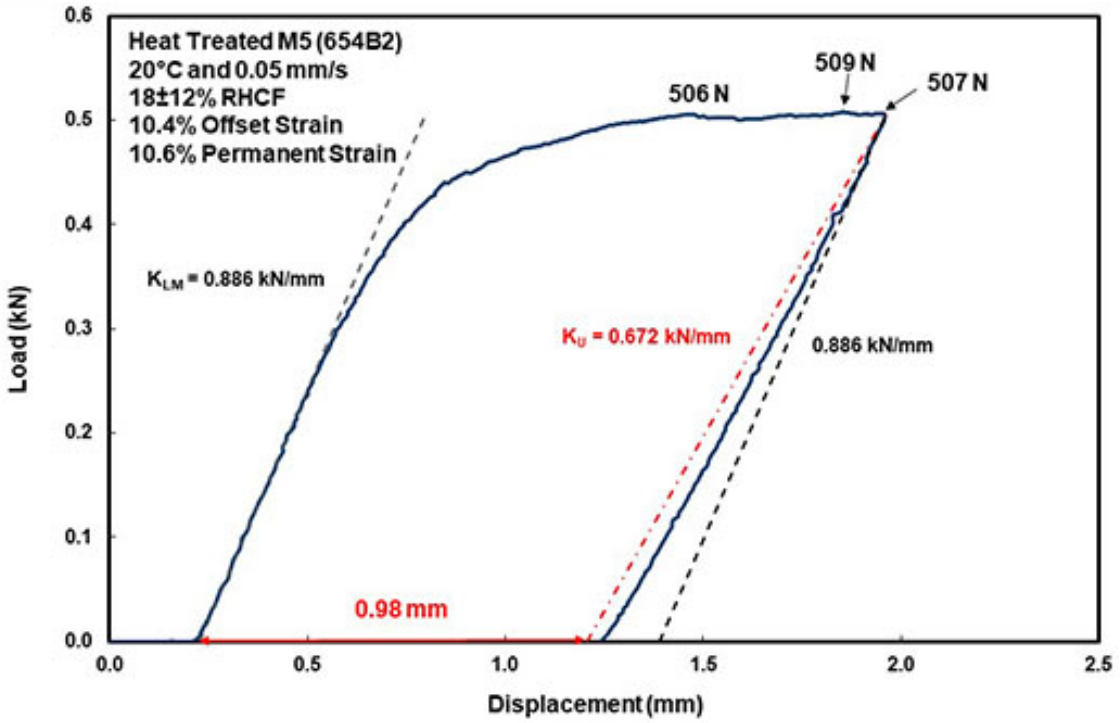

Figure 39: Load-displacement curve for RCT sample 654B2.

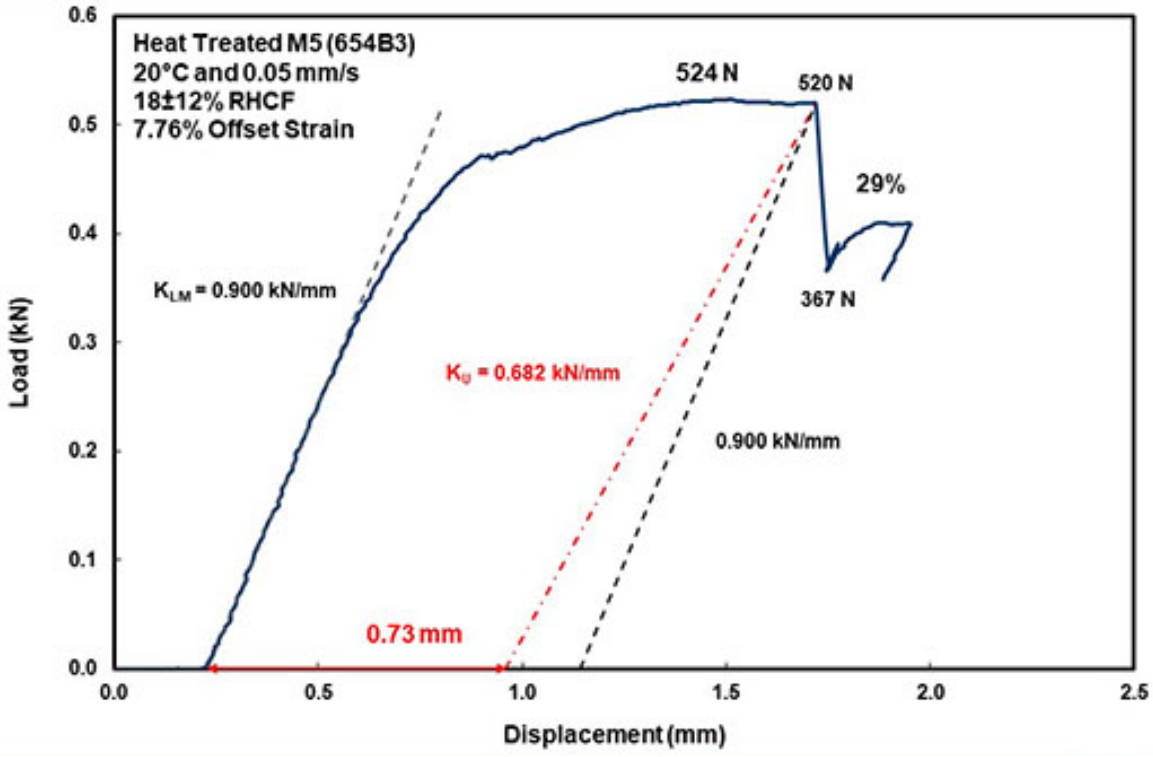

Figure 40: Load-displacement curve for RCT sample 654B3.

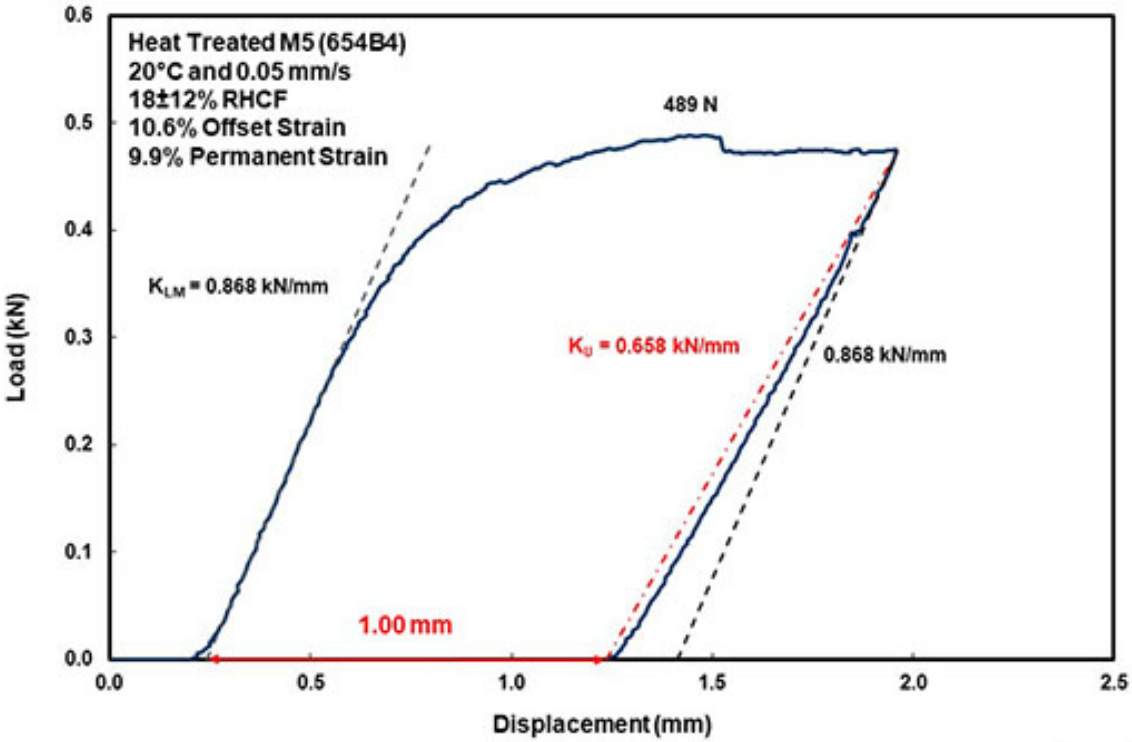

Figure 41: Load-displacement curve for RCT sample 654B4.

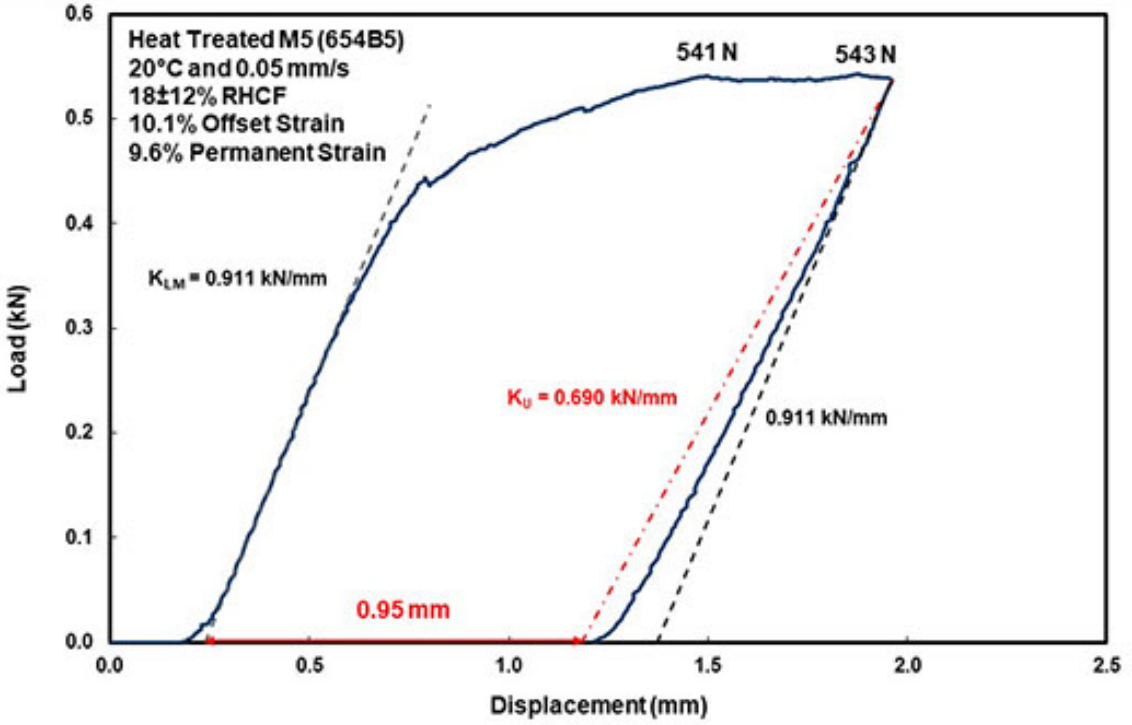

Figure 42: Load-displacement curve for RCT sample 654B5.

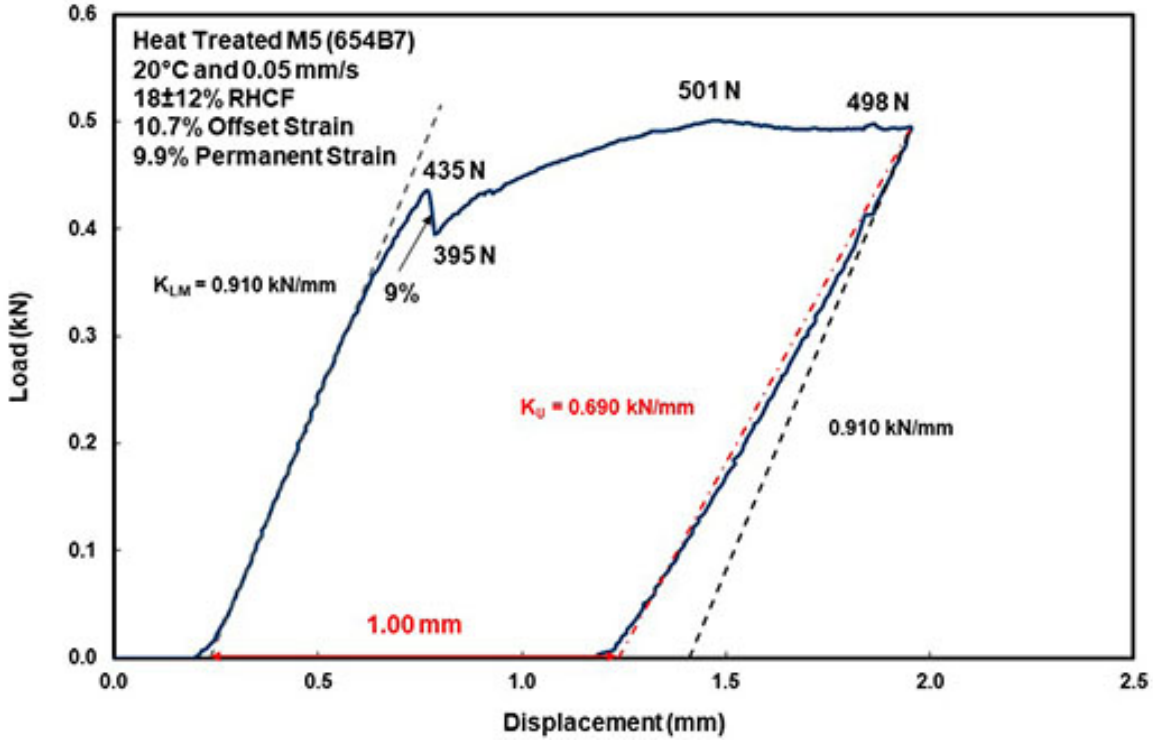

Figure 43: Load-displacement curve for RCT sample 654B7.

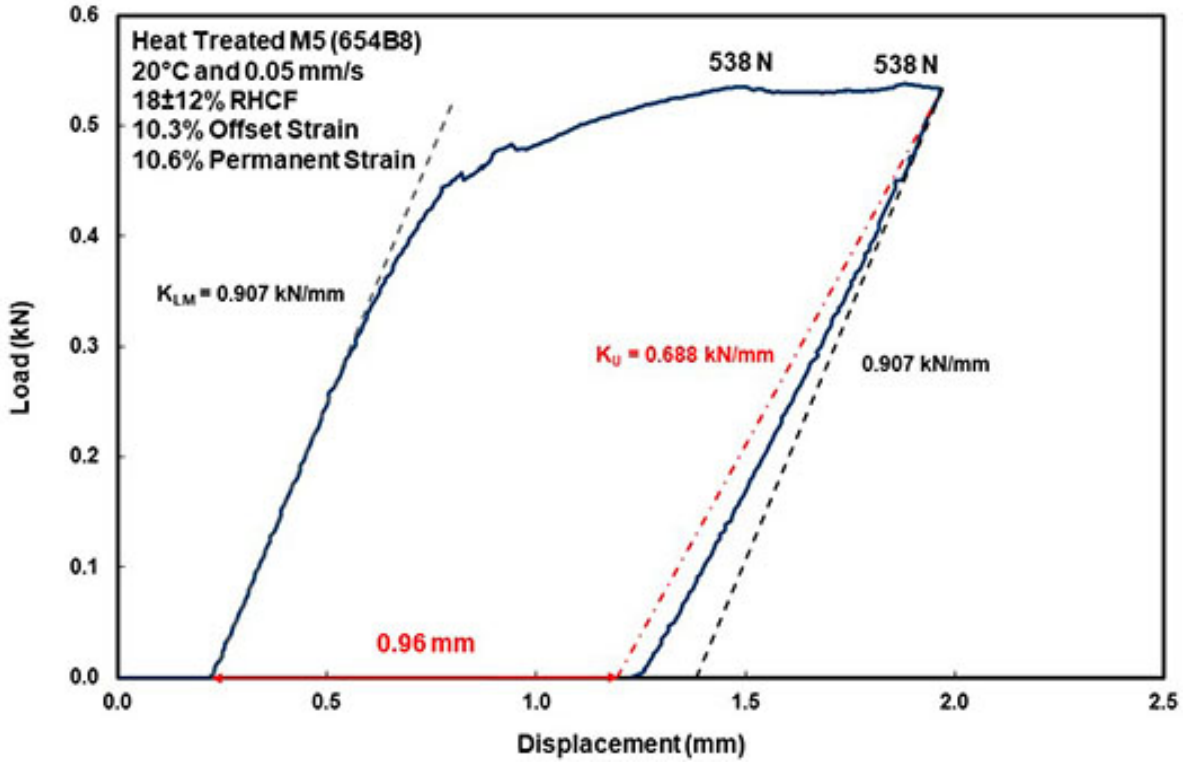

Figure 44: Load-displacement curve for RCT sample 654B8.

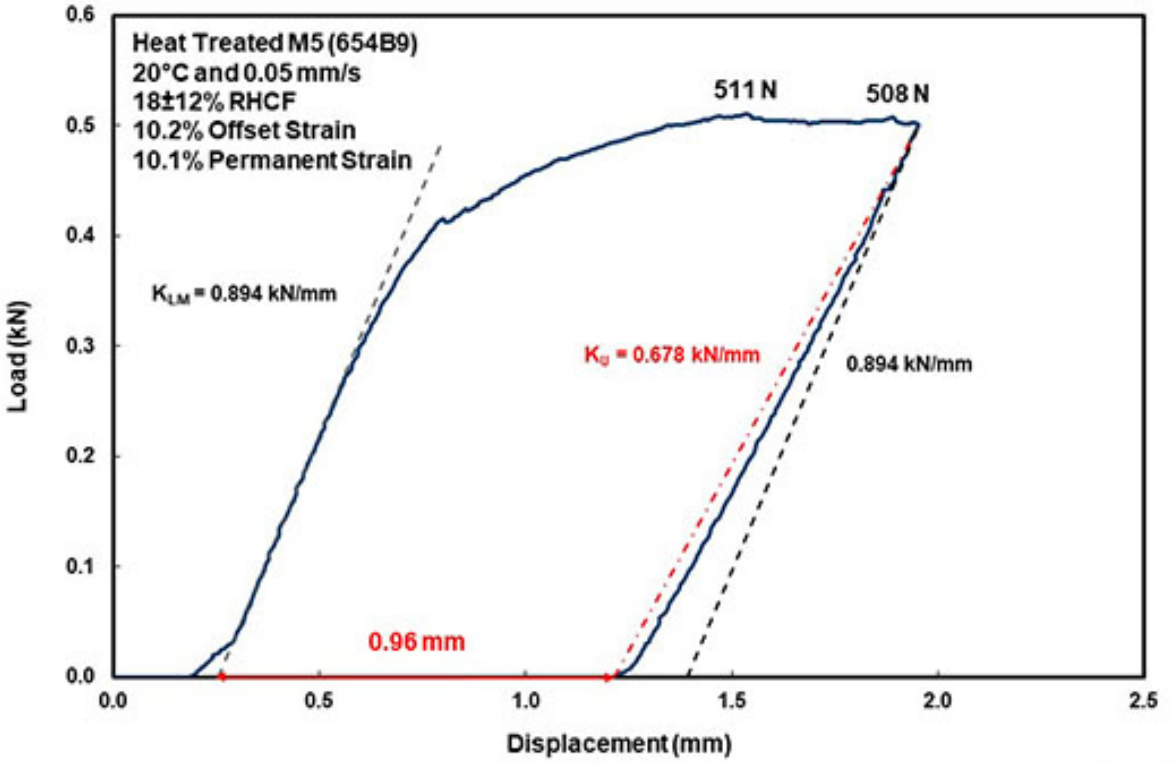

Figure 45: Load-displacement curve for RCT sample 654B9.

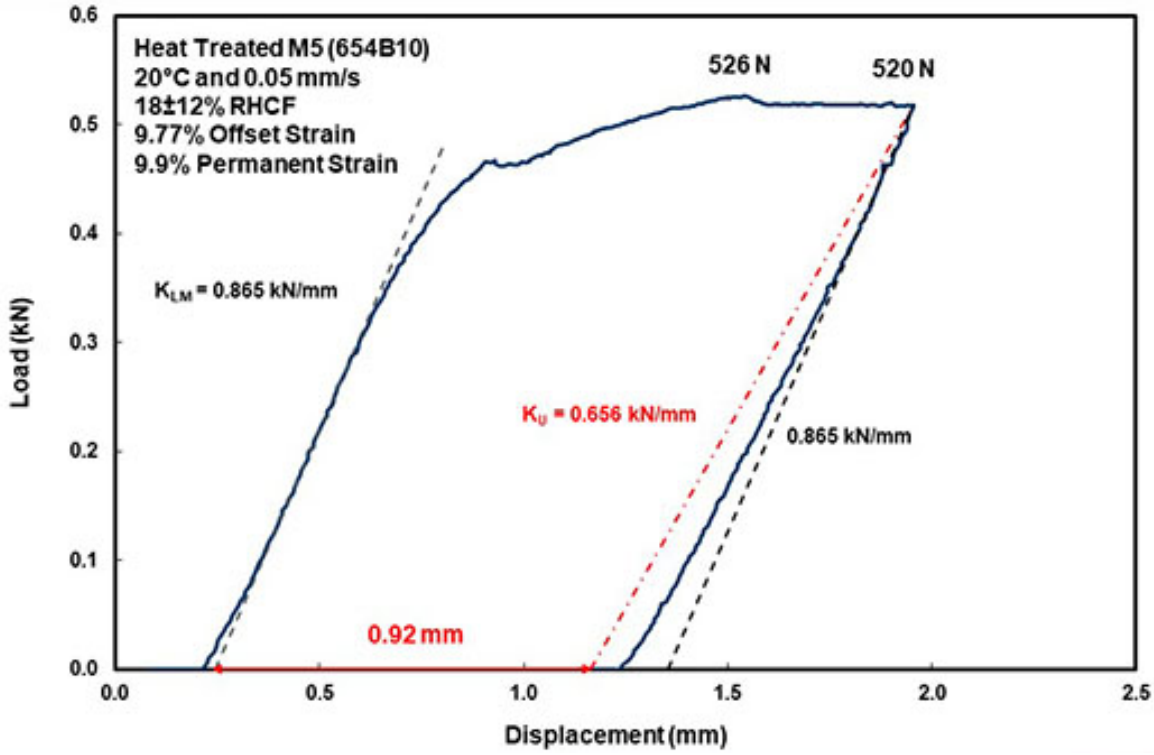

Figure 46: Load-displacement curve for RCT sample 654B10.

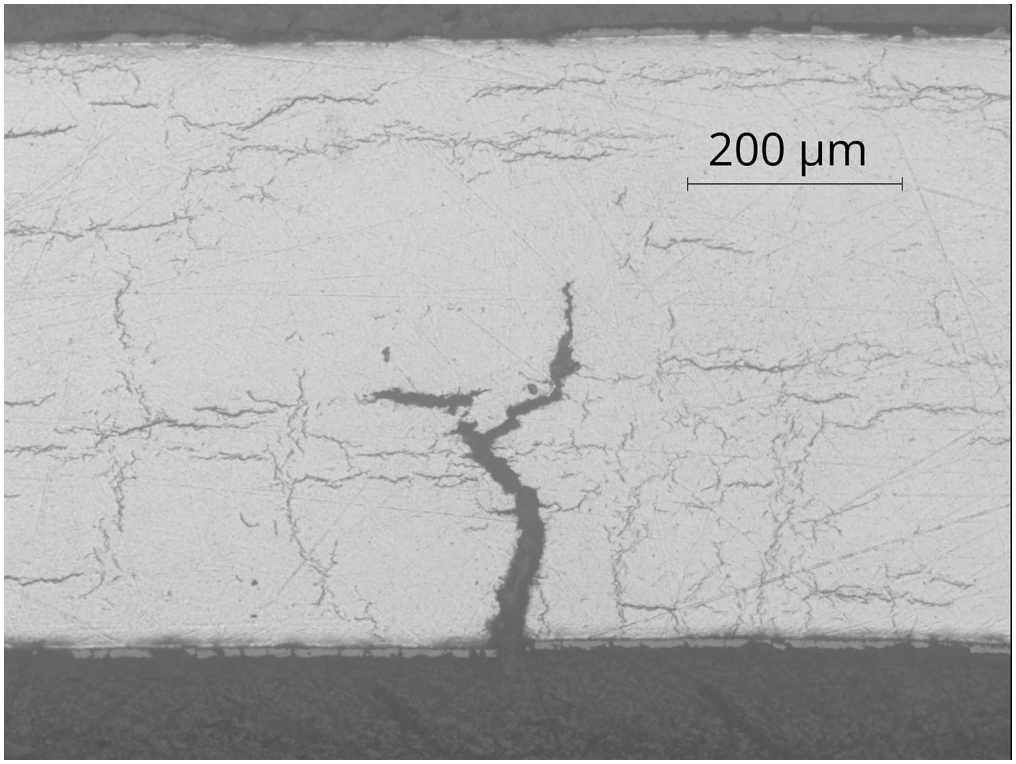

Figure 47: Image (100X) of 60% radial crack at 12 o'clock observed at the end (654B3A) of RCT sample 654B3 following a 29% load drop.

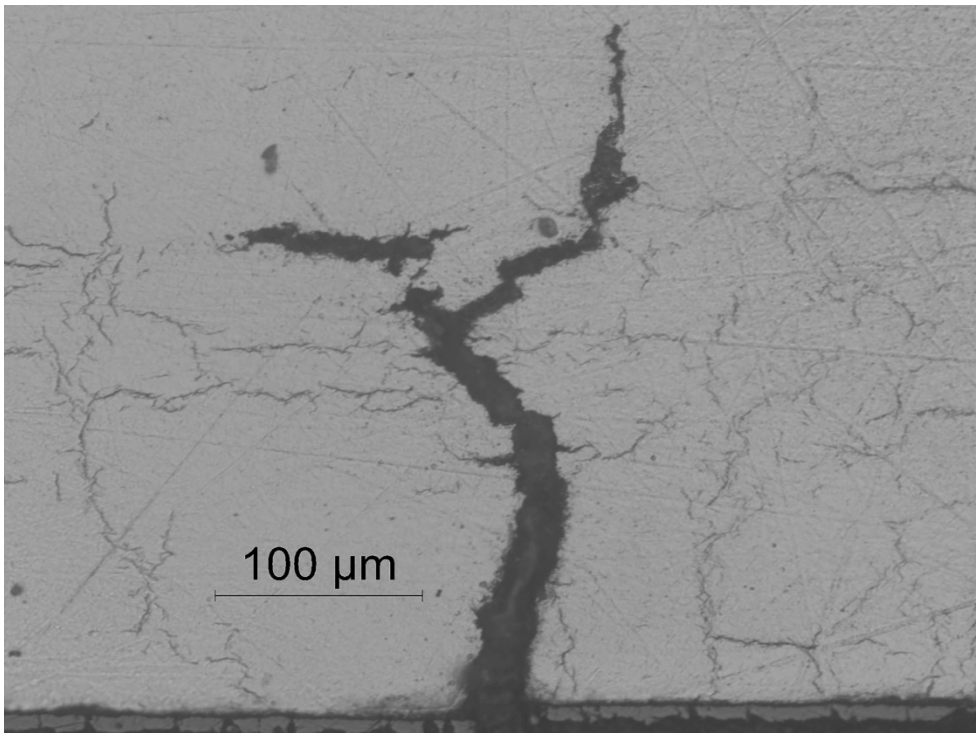

Figure 48: Image (200X) of 60% radial crack at 12 o'clock observed at the end (654B3A) of RCT sample 654B3 following a 29% load drop.

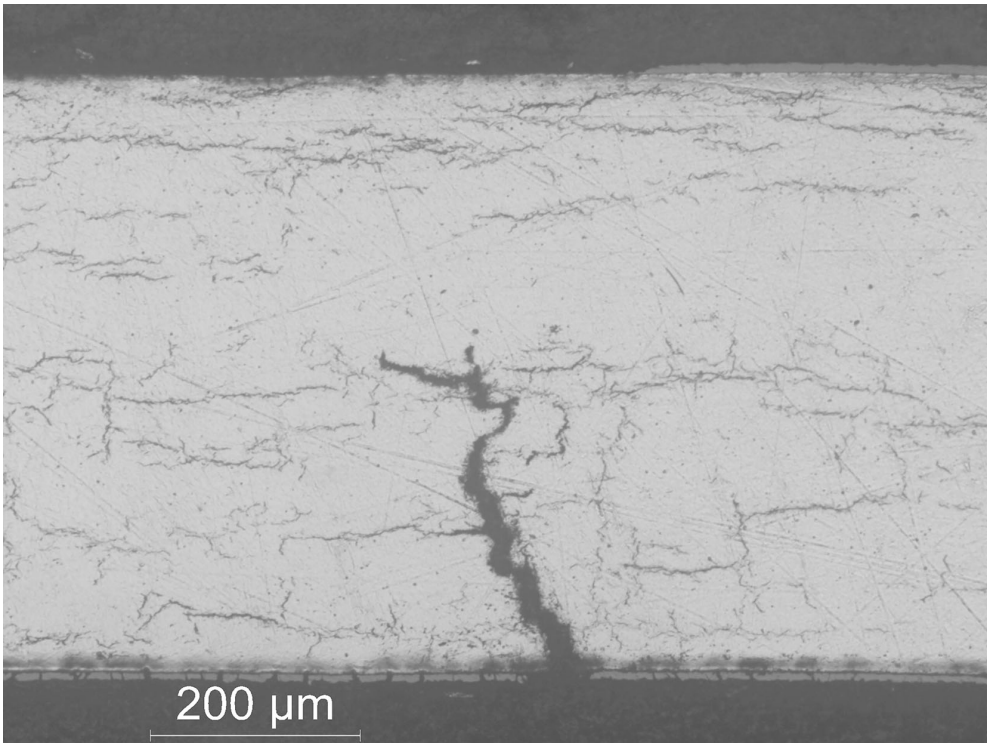

Figure 49: Image (100X) of 54% radial crack at 12 o'clock observed at the mid-span (654B3B) of RCT sample 654B3 following a 29% load drop.

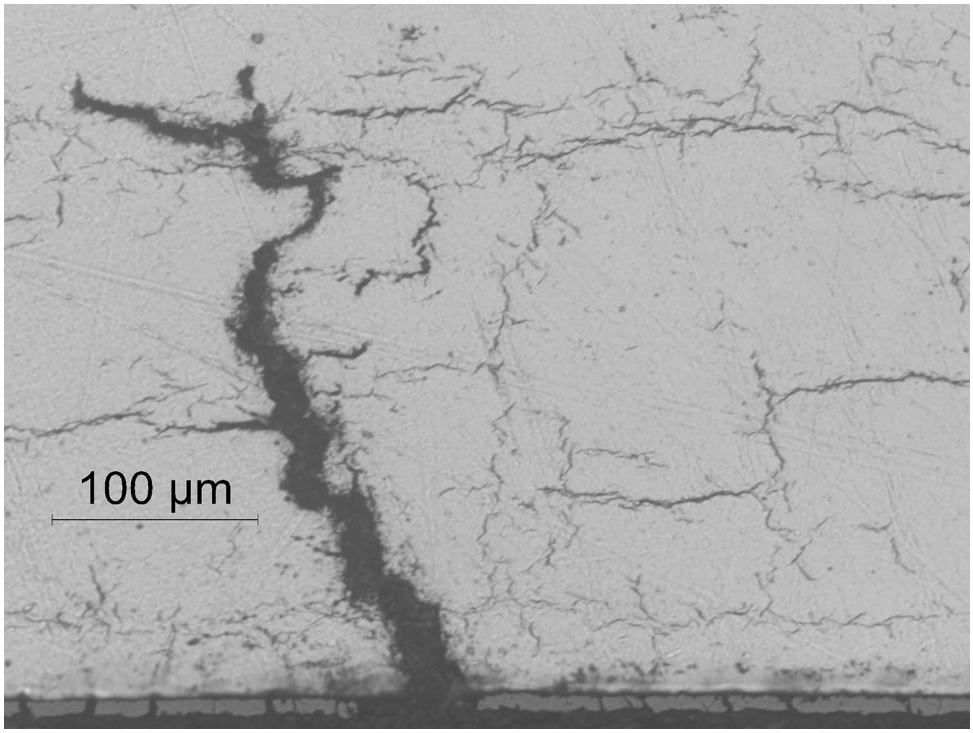

Figure 50: Image (200X) of 54% radial crack at 12 o'clock observed at the mid-span (654B3B) of RCT sample 654B3 following a 29% load drop.

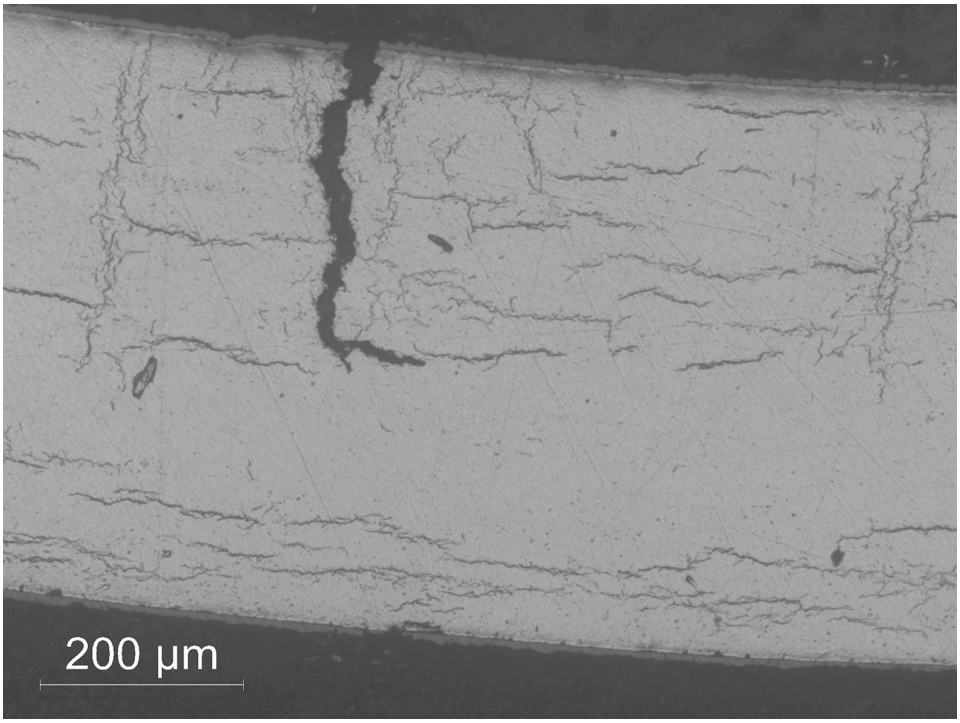

Figure 51: Image (100X) of 54% radial crack at ≈6 o'clock observed at the mid-span (654B3B) of RCT sample 654B3 following a 29% load drop.

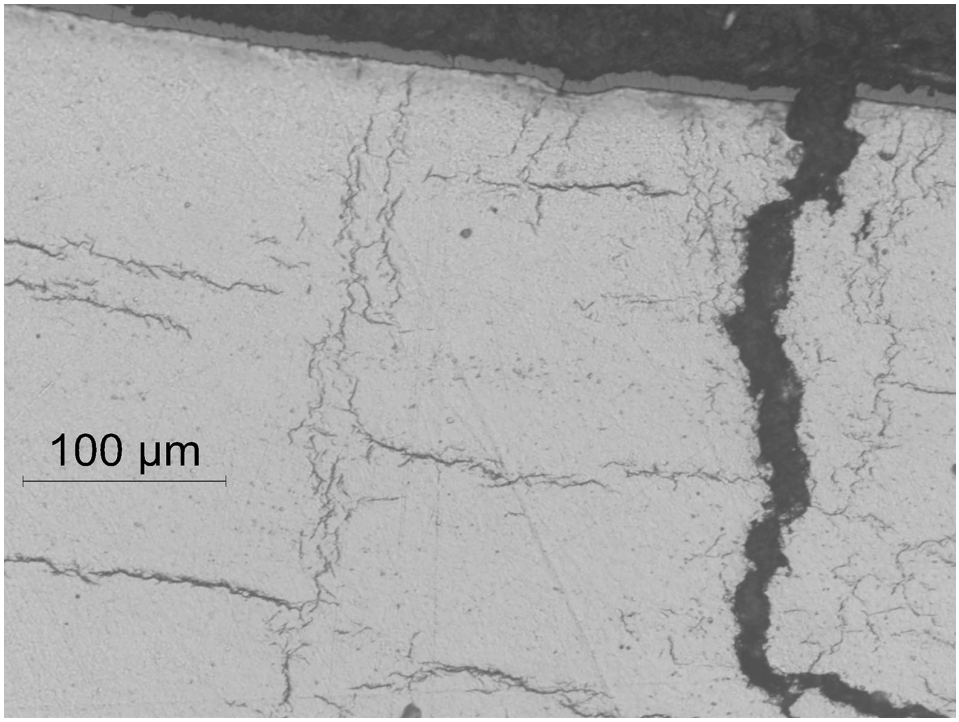

Figure 52: Image (200X) of 54% radial crack at ≈6 o'clock observed at the mid-span (654B3B) of RCT sample 654B3 following a 29% load drop.

5. ZIRLO® CLADDING CHARACTERIZATION AND TEST RESULTS

The sibling-pin cladding segments received from ORNL are described in Table 1. Two ZIRLO® segments were selected for metallographic examination (MET) and RCT: (a) 655B (as-irradiated ORNL ID 3D8E14 2565 2655) and (b) 656B (FHT ORNL ID 3F9N05 3241 3331) [4]. The relative axial location of the mid-span of these segments were at 0.71 and 0.90 z/L_f. Segment 655B was from the uniform burnup region away from grid spacers, and segment 656B was located in the burnup down slope region partially under the top grid spacer. Prior to sectioning and defueling samples for ANL and prior to heat-treating 3F9N05, the cladding outer diameter was measured by ORNL [1] at two orientations along the fuel-rod length using LVDT. ORNL profilometry results are shown in Figs. 53 and 54 for as-irradiated ZIRLO® fuel rod 3D8E14 and as-irradiated (pre-FHT) ZIRLO® fuel rod 3F9N05, respectively, in axial regions relevant to segments sent to ANL. The estimated average, minimum and maximum values for 3D8E14 are 9.515 mm, 9.49 mm, and 9.54 mm, which give 9.515±0.025 (note ±0.025 mm is not one standard deviation), within 2565 mm and 2655 mm. Estimated average, minimum, and maximum values for 3F9N05 are 9.48 mm, 9.43 mm, and 9.51 mm, which give 9.48±0.03 mm. These measurements are only accurate to the second decimal place.

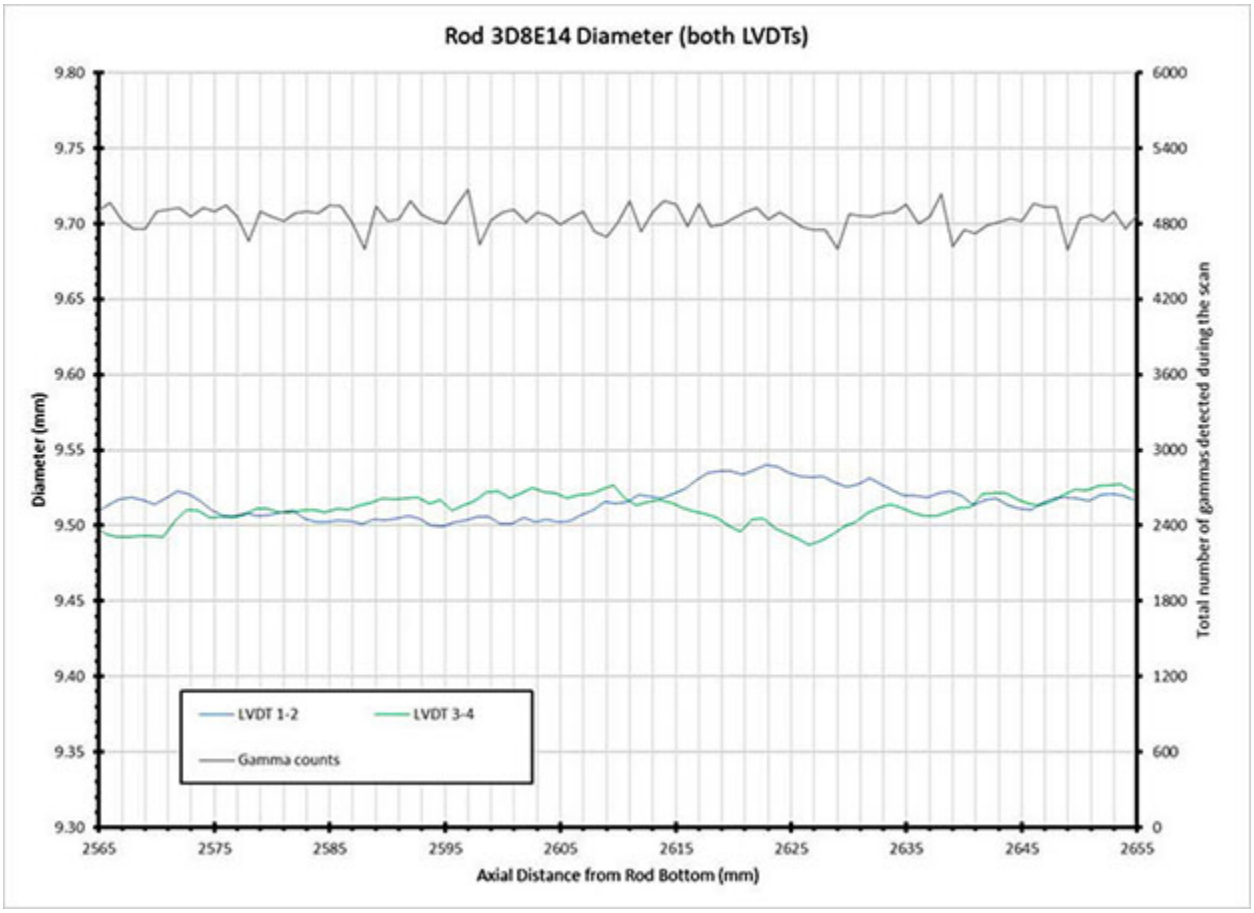

Figure 53: Profilometry results for as-irradiated ZIRLO® fuel rod 3D8E14 for the 655B segment axial locations from the fuel-rod bottom (*courtesy of ORNL*).

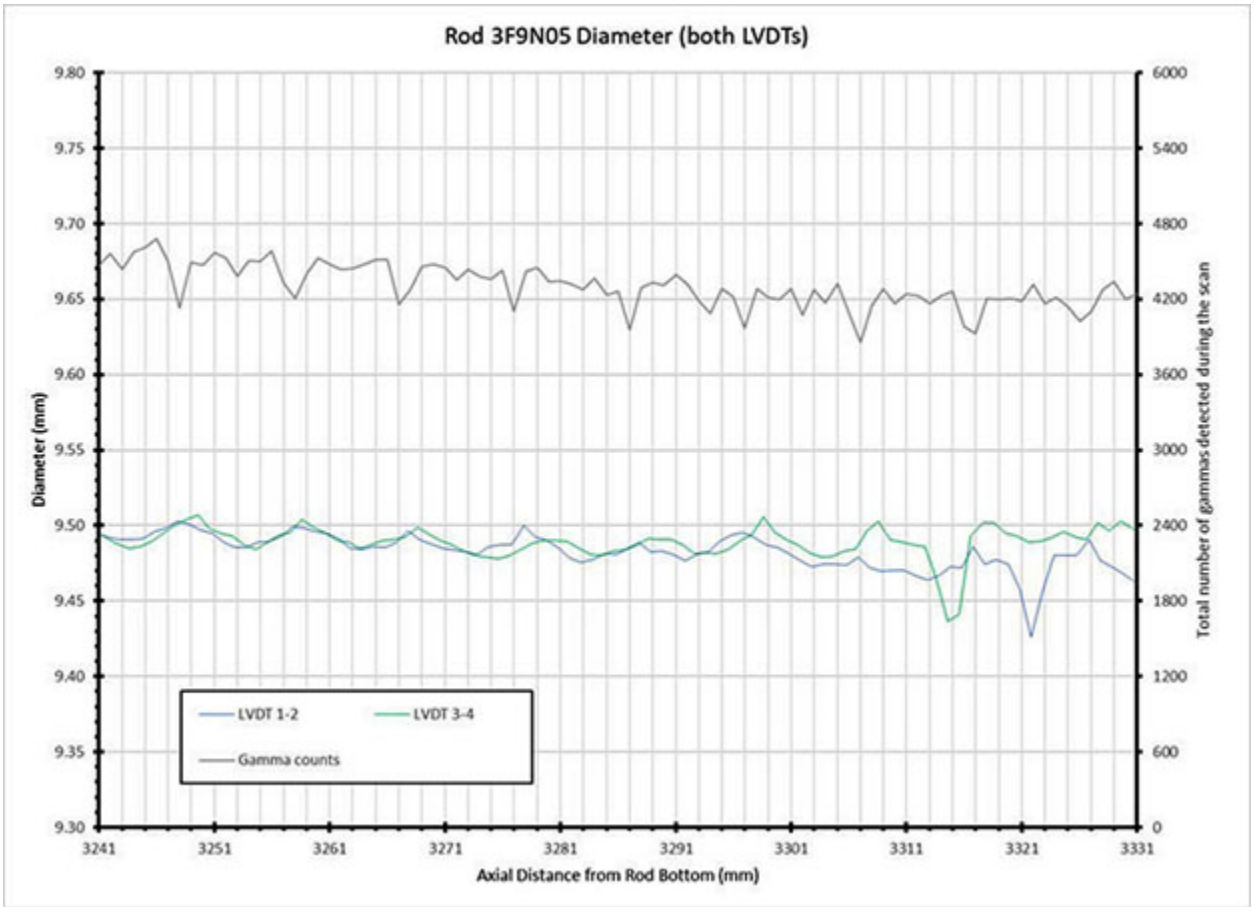

Figure 54: Profilometry results for as-irradiated ZIRLO® fuel rod 3F9N05 for the 656B segment axial locations from the fuel-rod bottom (*courtesy of ORNL*).

5.1 MET & RCT RESULTS FOR AS-IRRADIATED ZIRLO® (655B)

Figure 55 shows the pre-sectioning diagram for segment 655B. The lengths of the eight RCT samples were in the range of 8.01±0.07 mm (0.07 mm is one standard deviation) following sectioning, squaring and deburring. The three samples sectioned for metallographic examination are labeled B1, B6, and B11 with the circle indicating the surface to be examined.

Prior to sectioning, D_o was measured at three axial locations (≈25%, ≈50%, and ≈75% from the bottom) and two orientations (0° and 90°) to be 9.45±0.01 mm, which is lower than the ≈9.52±0.03 mm shown in Fig. 53. Following sectioning, squaring, and deburring of RCT samples, D_o was measured at two RCT-sample mid-span orientations by one worker in the squaring-deburring glove box (16 data points) and at three axial locations and two orientations by another worker in the Instron glove box (48 data points). Averaging the combined data sets gave 9.47±0.01 mm, which is lower than the minimum value (9.49 mm) shown in Fig. 53. It appears that defueling in nitric acid, along with ANL ethanol cleaning, may have reduced fuel rod diameters by removing debris on the fuel rod that may have been present at the time ORNL performed profilometry.

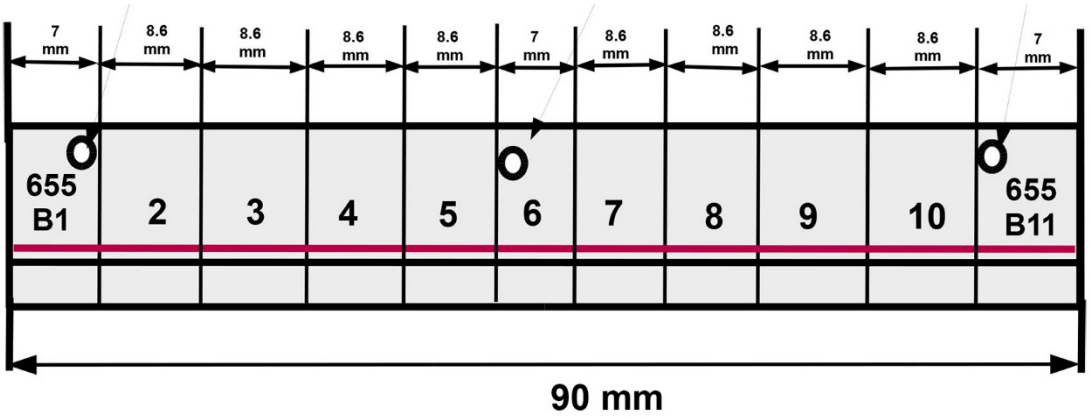

Figure 55: Pre-sectioning diagram for as-irradiated ZIRLO® segment 655B. Segment top is to the left.

Metallographic Examination Results

Images at 100X magnification were used to measure h_m and images at 200X were used to measure h_{ox} at about 14 circumferential orientations for each axial location. The grinding process used to prepare MET samples can degrade the oxide layer such that only part of the oxide layer is imaged at particular circumferential locations. Locations for the 14 images per sample were chosen to give the maximum oxide layer thickness.

Metallographic examinations were performed for the as-polished surfaces located on the 655B1, 655B6, and 655B11 surfaces to determine h_{ox} and h_m. However, the oxide layer was too degraded on the 655B1 surface for measurements. Results for the 655B6 and 655B11 surfaces gave 28±3 µm for h_{ox} and 560±7 µm for h_m. Previous ANL data for irradiated ZIRLO® with oxide layers ranging from 26 µm to 30 µm indicate about 350±40 wppm C_H for a 28-µm oxide layer. The hydrogen content will be measured directly in future work at several axial locations to determine more precise values for ZIRLO® segment 655B, as well as axial and circumferential variations in hydrogen content.

655B1, 655B6 and 655B11 surfaces were etched to image hydrides. The new solution prepared for etching resulted in spots on the surfaces, which were unacceptable. However, the results indicated circumferential hydrides located within the outer-surface hydride rim (expected results), several circumferential hydrides located near the cladding inner surface (unexpected as in not previously observed) and the middle 70% to 80% of the cladding wall essentially devoid of hydrides (unexpected). For irradiated ZIRLO® cladding previously examined, the several long circumferential hydrides were located near the cladding mid-radius rather than near the cladding inner wall. Also observed in the wall region with very low hydrogen content were short circumferential and radial hydrides forming an “x-like” or “cross” pattern. The surfaces were re-ground, re-polished, and re-etched for about 30 seconds to better image the short hydrides. This long etching time resulted in over-etching of the circumferential hydrides in the cladding rim. The process was repeated with a shorter etching time of about eight seconds.

Figure 56 shows the hydride distribution and orientation typical of this material. It also includes the longest (21% RHCF) radial hydride. Most of the 43 images at 100X magnification showed similar x-like hydrides with 7±2% maximum RHCF. Figure 57 shows a singular, long (26% RHCF) radial hydride emanating from the inner-surface circumferential hydrides on the 655B11 surface. The axial continuity of this hydride was at least 0.3 mm, as it appeared in all three sets of images. The RHCF was 8±4%.

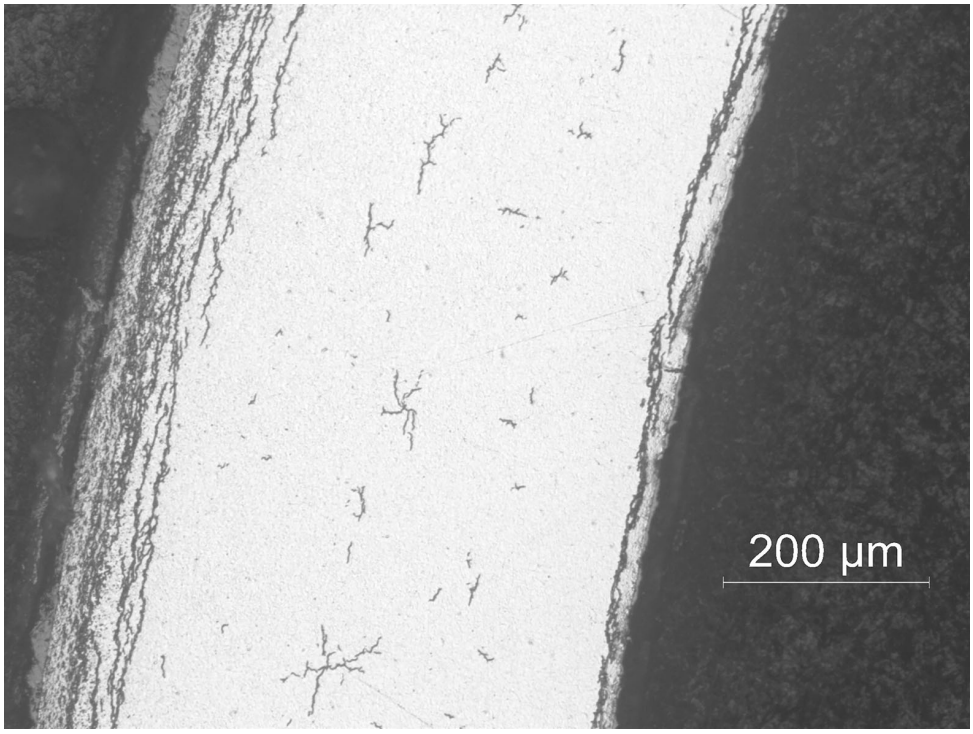

Figure 56: Centrally located radial hydride (21% RHCF) observed on the as-irradiated ZIRLO® 655B1 surface at about 9:15 o'clock.

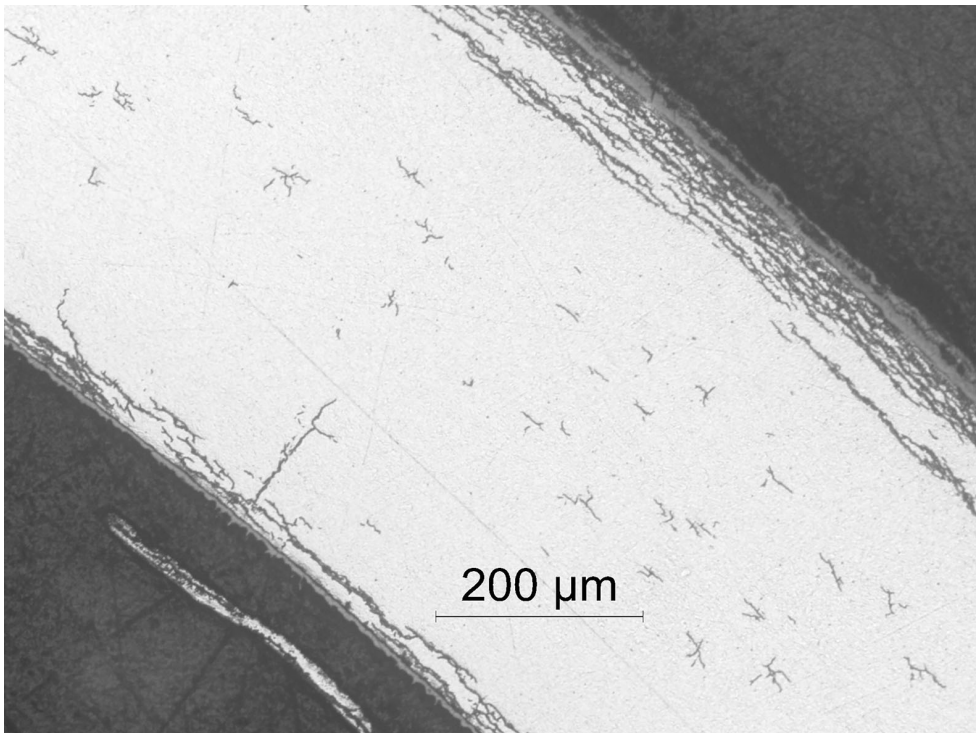

Figure 57: Longest (26%) radial hydride observed on the as-irradiated ZIRLO® 655B11 surface at about 2 o'clock.

RCT Results

All RCTs were conducted at RT (nominally 20°C), 0.05 mm/s displacement rate, and 1.7-mm targeted sample displacement. The load was applied between the black and red lines shown in Fig. 55. Although short radial hydrides (8±4%) were present in these RCT samples, high RT ductility was anticipated because most of the radial hydrides were located in regions of low-tensile, zero, and low-compressive stresses induced by RCT sample bending.

Figures 58 through 65 show the RCT load-displacement curves for 655B samples B2−B5 and B7−B10, respectively. None of the samples exhibited abrupt load drops and only a few of the samples exhibited gradual load drops of a few percent. The results indicated that no cracking or only very minor cracking occurred. As such, the maximum offset strain recorded represents a lower bound on ductility.

Samples B3 (Fig. 59), B5 (Fig. 61), and B9 (Fig. 54) had negligible loading lags, which resulted in the largest offset strains (10%). The ductility for these samples was >10%. These three samples also had the largest loading slopes (1066±49 N/mm). Samples that experienced loading lags achieved a maximum normalized loading slope of only about 825 N/mm and maxim offset strains of only 6% to 8%. The tests with loading lags did, however, reach normalized P_{max} values consistent with samples that experienced no loading lags. The average of all normalized P_{max} values was 647±12 N.

Loading lags are a result of high spots on the cladding OD resulting in initial loading of only part of the sample. Such high spots can result from cladding ridging due to pellet-cladding mechanical interaction during reactor operation, from flaring and burrs induced by cutting, and from a slight bowing of samples. The squaring and deburring operations should have minimized the effects of cutting. Also, the RCT sample length (≈8 mm) is shorter than the pellet length (≈10 mm). For the unlikely event of the RCT sample loaded by a pellet symmetrically located within that cladding region, cladding sample ends would have larger outer diameters than the sample mid-span. For other pellet axial locations, the high spot could be located anywhere within the RCT sample.

There are two ways to anticipate whether or not a loading lag might occur. The variation of D_o measured at the RCT sample mid-span and at the sample ends is one way to anticipate a loading lag. A more direct way is to lower the Instron loading rod until contact is made with the sample. If the contact point occurs at a higher elevation than predicted by the average D_o for the sample, then a loading lag might occur. However, the loading-rod-plate contact point was often at a higher elevation than predicted from D_o measurements. The source of the loading lag, particularly for the one shown for sample B8 in Fig. 63, is not clear. Nor is it clear regarding the best way to minimize the effects of the loading lag, which are reduced loading slope and reduced full-sample displacement and offset strain. One approach to increase the sample displacement is to increase the contact load from about 25 N to 45 N. This has a relatively small effect on the results. The second approach is to stop the test during the loading lag, withdraw the loading rod, and reload the sample. This was done for sample 655B10, which exhibited an initial low loading slope (<500 N/mm), a load drop to about 10 N, and a loading slope rise to 760 N/mm. The test was stopped, and the load was withdrawn. It was discovered that the sample had a burr, indicating that deburring was not 100% successful for this RCT sample. The sample was reloaded and exhibited a normalized loading slope of 874 N/mm, a normalized P_{max} of 659 N, and offset and permanent strains of about 8%. If the test had been run without interruption, the loading slope would have been lower and the offset and permanent strains would have been lower.

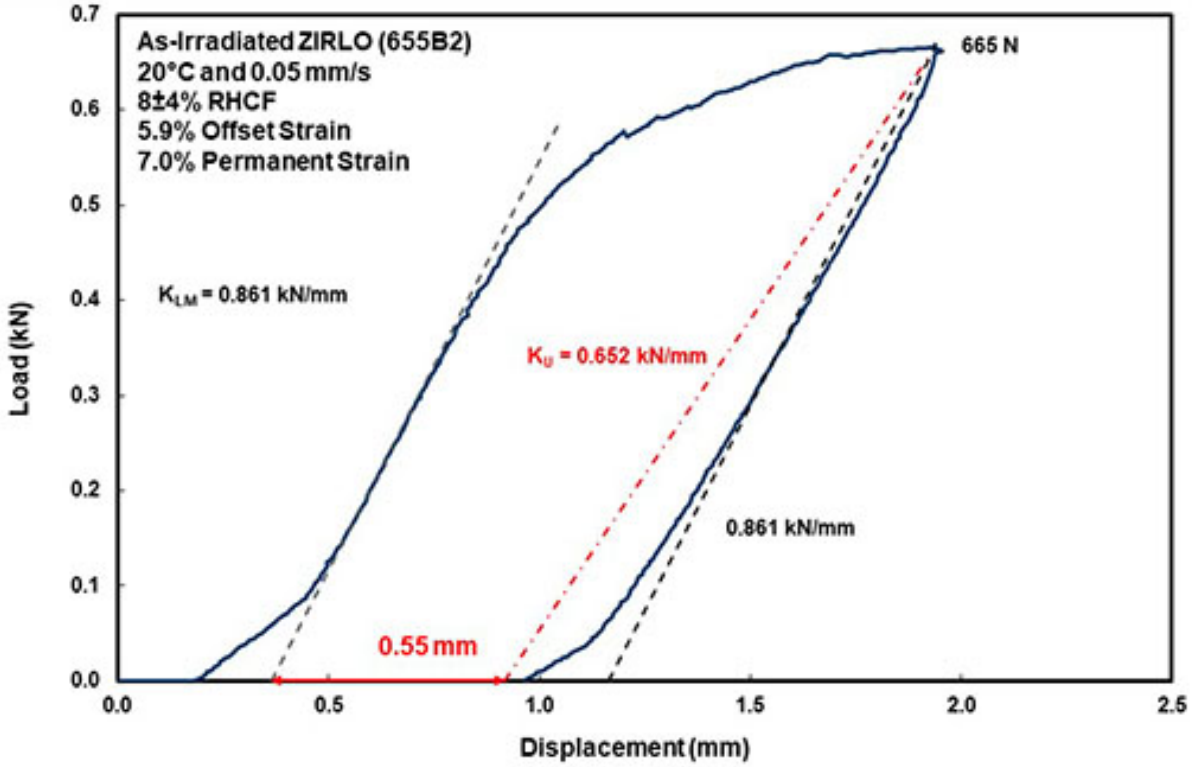

Figure 58: Load-displacement curve for RCT sample 655B2.

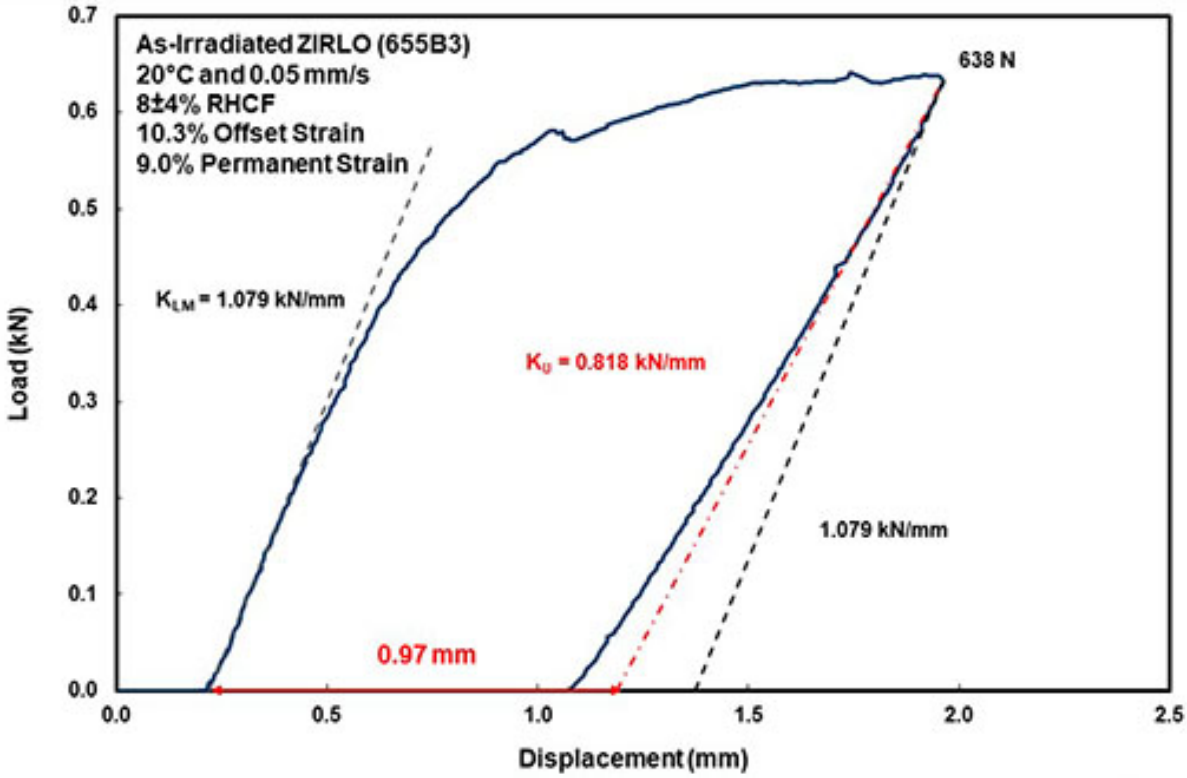

Figure 59: Load-displacement curve for RCT sample 655B3.

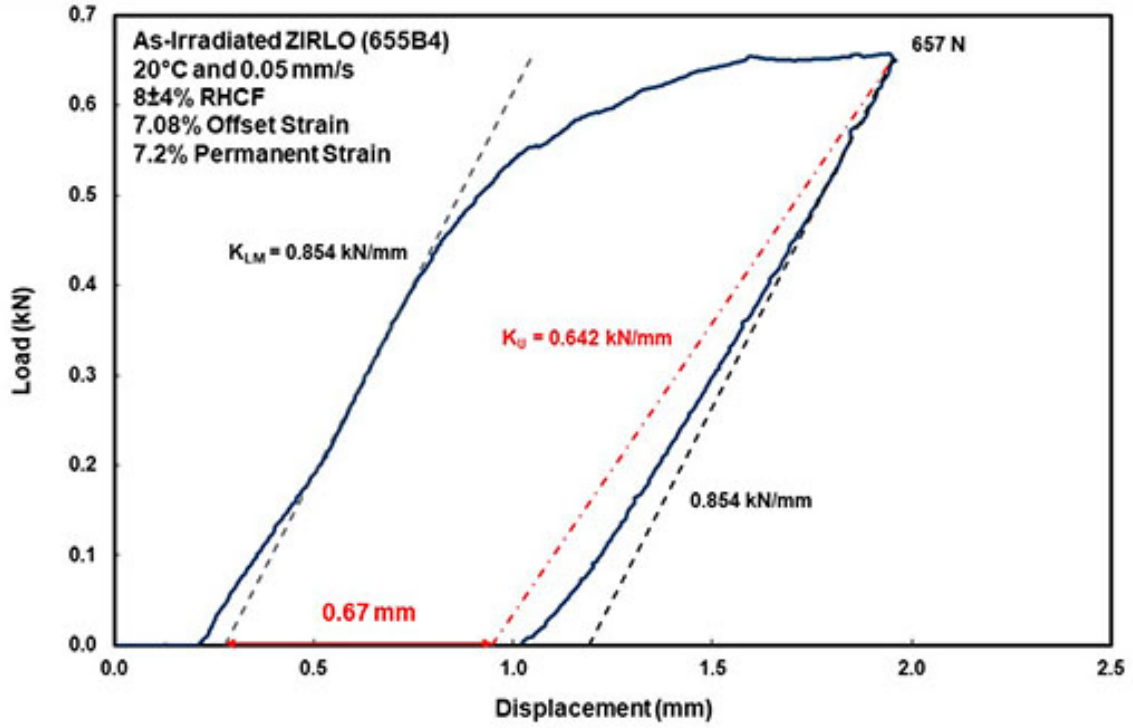

Figure 60: Load-displacement curve for RCT sample 655B4.

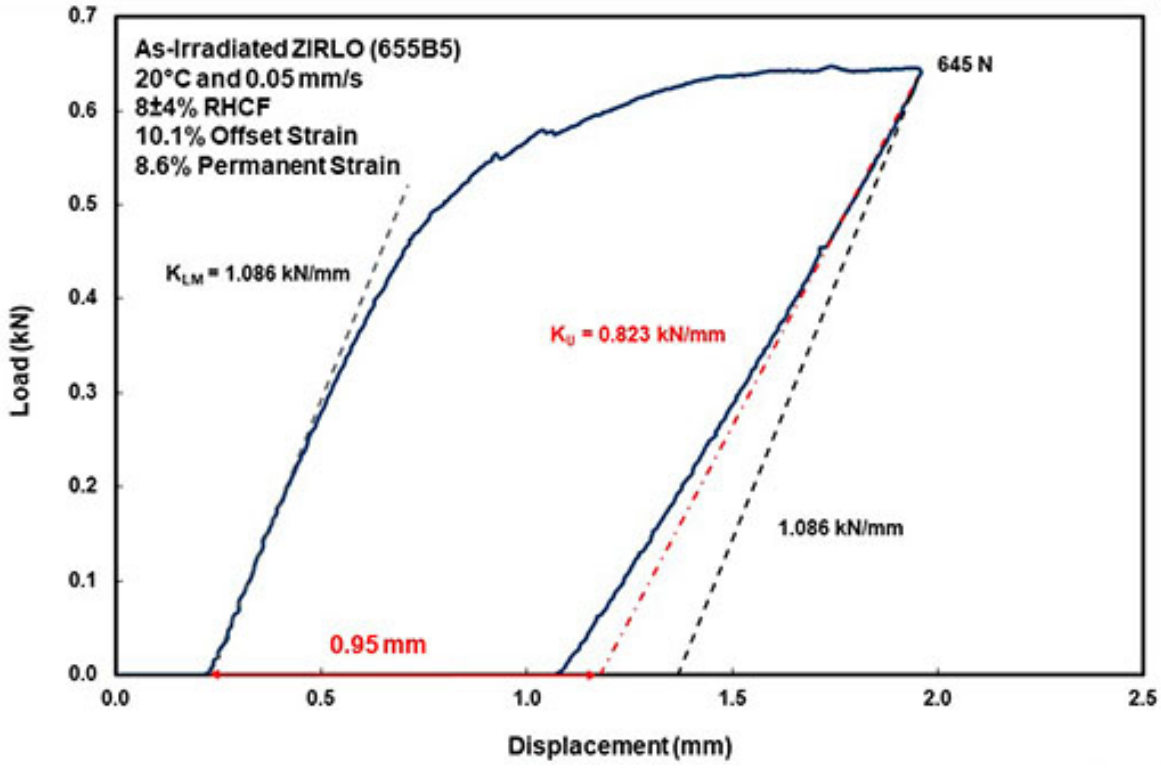

Figure 61: Load-displacement curve for RCT sample 655B5.

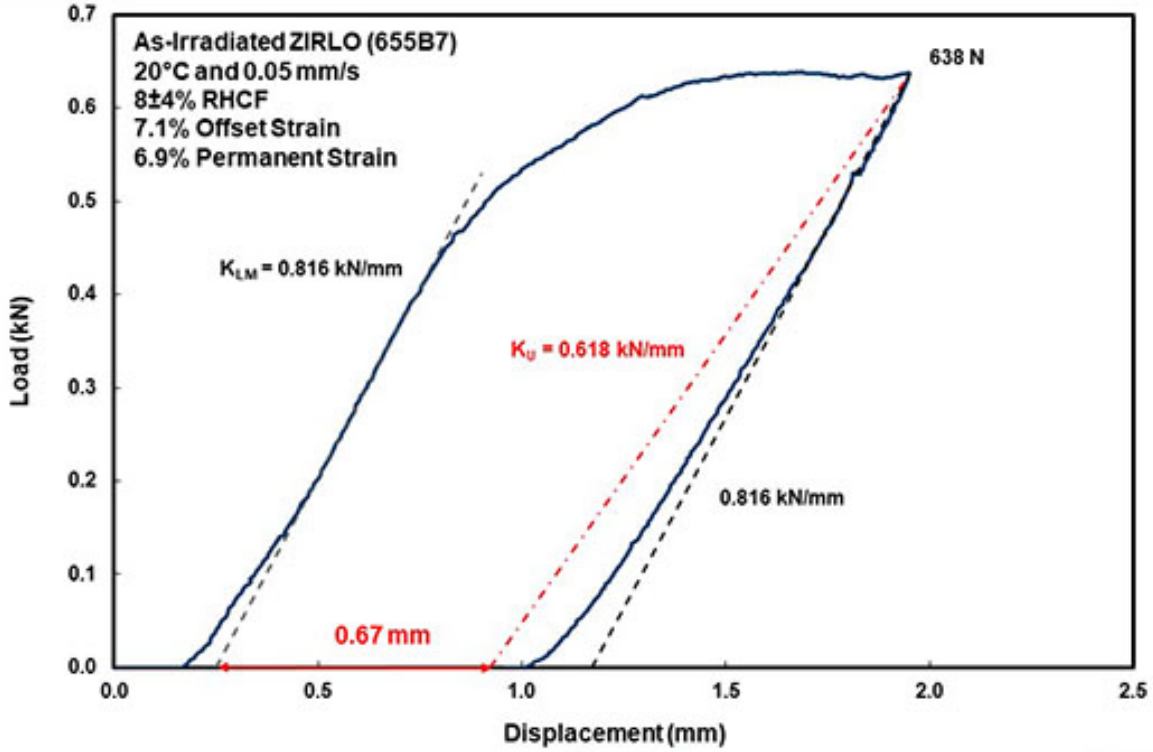

Figure 62: Load-displacement curve for RCT sample 655B7.

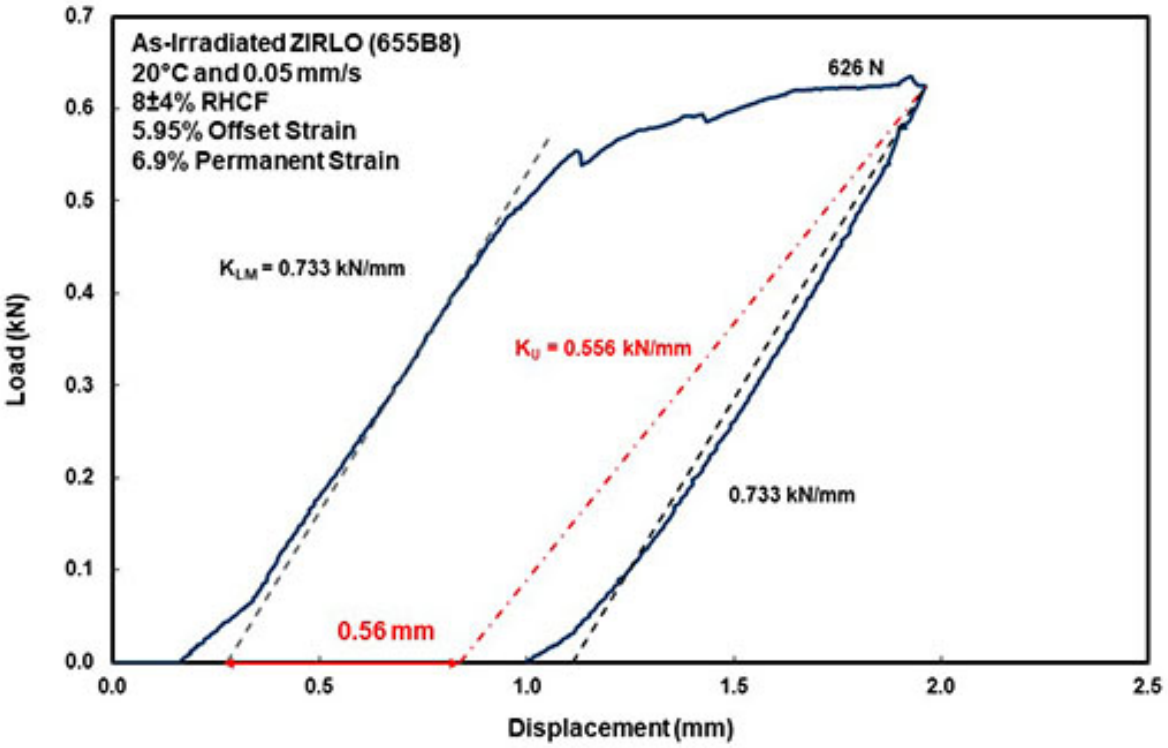

Figure 63: Load-displacement curve for RCT sample 655B8.

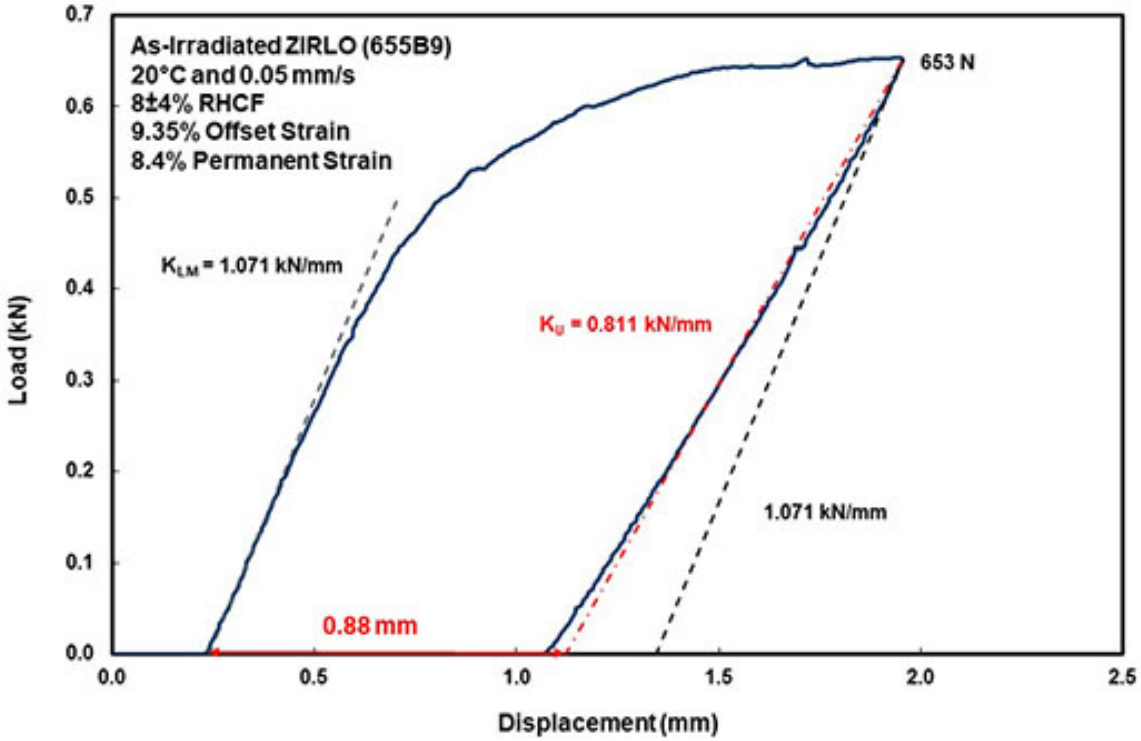

Figure 64: Load-displacement curve for RCT sample 655B9.

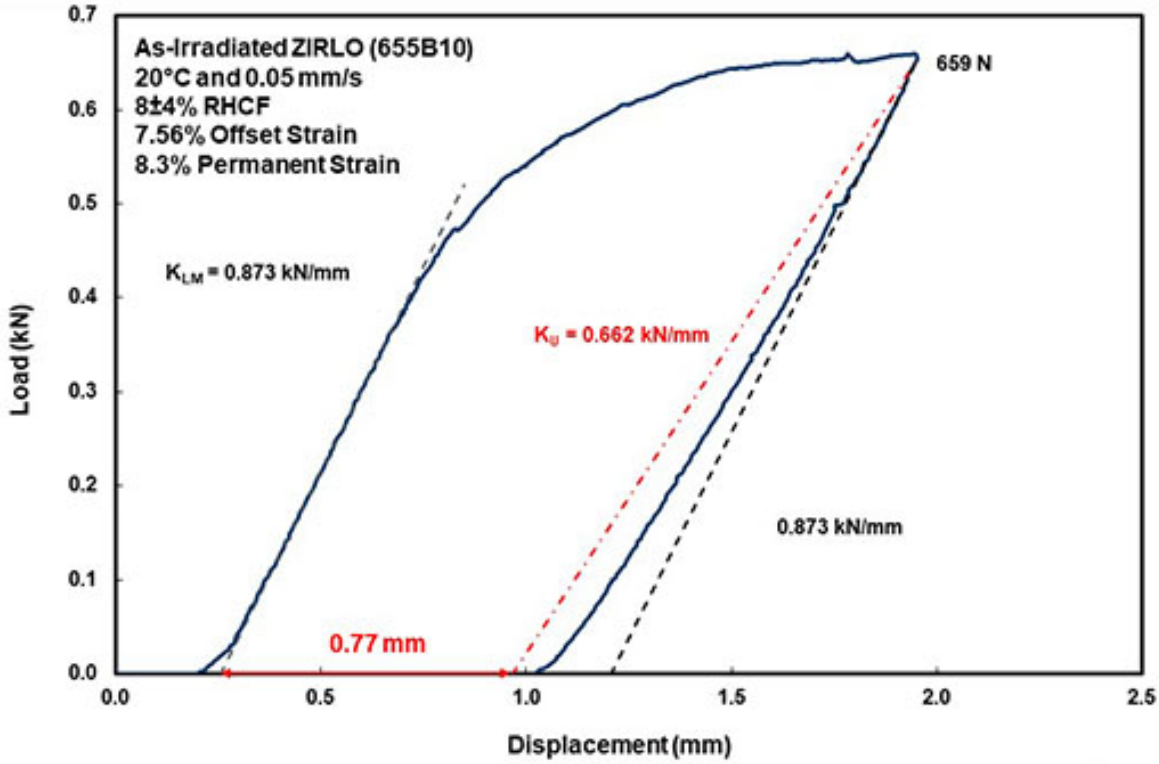

Figure 65: Load-displacement curve for RCT sample 655B10.

5.2 MET & RCT RESULTS FOR HEAT-TREATED ZIRLO® (656B)

Segment 656B is from fuel rod 3F9N05 at an axial location of 3241−3331 mm from the bottom of the fuel rod, which was subjected to FHT with 400°C PCT for eight hours followed by cooling at ≤3.7°C/h down to 100°C. Figure 66 shows the pre-sectioning diagram for segment 656B. Rings B1, B6, and B11 were sectioned for metallographic examinations of surfaces indicated by the open circles. Rings B2−B5 and B7−B10 were sectioned, squared and deburred for RCTs. Rings B3 and B8 exhibited interesting load drops of 13% at low displacement and 23% at high displacement, respectively. As such they were subsectioned for metallographic examination to investigate crack depth vs. load drop. The RCT sample lengths were in the range of 7.97±0.17 mm.

Prior to sectioning, the cladding outer diameter was measured at three axial locations and two orientations per location. The resulting D_o was 9.45±0.01 mm with minimum and maximum values of 9.43 mm and 9.46 mm, respectively. Following squaring and deburring, RCT sample minimum and maximum D_o values were measured at the mid-span by one worker in the squaring-deburring glove box. Prior to conducting the RCTs, D_o was measured at two orientations at the RCT sample mid-span and ends by another worker. On the basis of the 64 data points generated for RCT samples after sectioning, D_o = 9.47±0.01 mm, which is comparable to the 9.48±0.03 mm measured by ORNL before FHT.

Metallographic examination of as-polished (not etched) surfaces of B1, B6, and B11 gave 44±7 µm for h_{ox} and 554±6 µm for h_m. On the basis of irradiated ZIRLO® with 40−48 µm oxide layers previously characterized by ANL, C_H is estimated to be 550±50 wppm. The ratio of R_{mi} and h_{ox} is used in Eq. 1 to determine the wall-average hoop stress, along with the internal pressure at 400°C at cooling initiation and the external pressure (assumed to be 0.1 MPa). The internal pressure was measured by ORNL at the ambient hot-cell area temperature and results were extrapolated to 25°C to give 4.0 MPa. At 400°C, the internal pressure increased to 9.00 MPa. The geometric factor R_{mi}/h_{ox} and the average hoop stress were calculated with D_o = 9.46 mm for MET sample B1, 9.47 mm for MET sample B6 and 9.48 mm for MET sample B11. The average R_{mi}/h_{ox} was 7.46±0.08 and the average hoop stress was 66±1 MPa at 400°C.

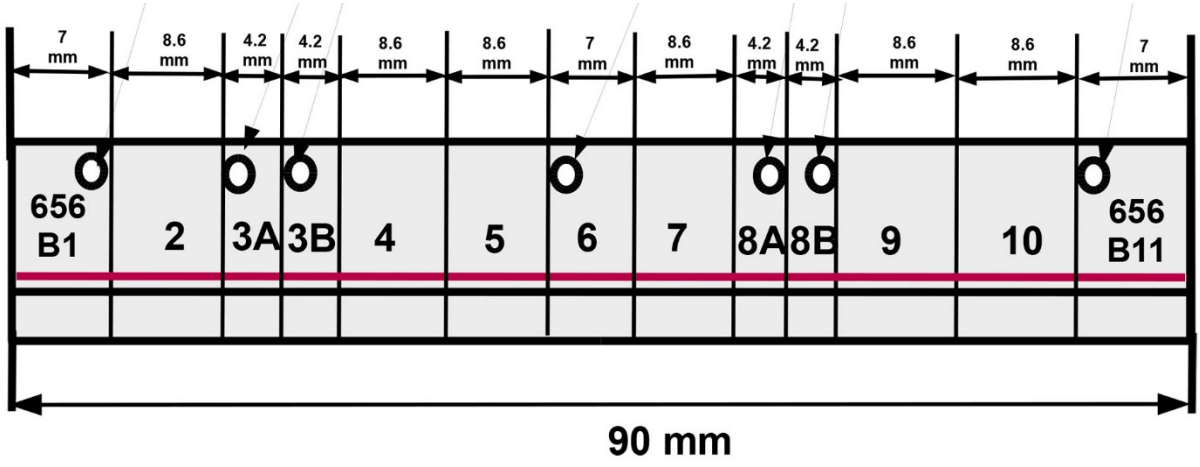

Figure 66: Pre-sectioning diagram for heat-treated ZIRLO® segment 656B. Top of segment is to the left.

Metallographic Examination Results

Surfaces 656B1, 656B6, and 656B11 were etched and imaged at 100X− and 200X−magnification. Forty images were taken for each sample to give full-surface coverage. On the basis of previous experience with irradiated ZIRLO® subjected to 80 MPa at 400°C prior to cooling at 5°C/h to 200°C, it was expected that the RHCF would be less than 9±5%. Although the stress at 400°C was lower (66 MPa) for FHT ZIRLO®, the cooling rate was slower (≤3.7°C/h) and this cooling rate was maintained down to 100°C, both of which would promote the precipitation of longer hydrides. Measured values for 656B1, 656B6, and 656B11 surfaces were, respectively, 10±9% with 20% maximum, 8±4% with 20% maximum, and 11±6% with 26% maximum. Combining these 120 data points gives 9±5%, which is close to the 8±4% measured for the as-irradiated ZIRLO® segment. However, as will be shown in the following, the locations of many of the radial hydrides for FHT ZIRLO® were in potentially high tensile stress regions, which could lead to cracks extending through part (<50%) of the cladding wall.

Figures 67 and 68 show 100X-magnification and 200X-magnification images of the 565B11 surface at the 7 o'clock orientation. The longest radial hydride (26% RHCF) is located closer to the outer surface. It is unlikely that crack initiation would occur at this radial hydride. However, it could enhance the extent of cracks initiating at the hydride-rim outer surface and propagating along circumferential hydrides to this radial hydride if it lined up with the 3 or 9 o'clock RCT orientations where the tensile hoop stress is highest at the outer surface.

Figures 69 and 70 show 100X- and 200X-magnification images of the 656B11 surface at the 10 o'clock orientation. A 25% radial hydride is observed to emanate from the cladding inner surface, which experiences the highest tensile hoop stress at the 12 o'clock and 6 o'clock RCT orientations. If the radial hydride lined up with either of these orientations, cracking could initiate at the innermost end of this hydride and propagate into about 25% of the wall.

The 656B11 surface had interesting radial hydrides at the 4 o'clock orientation that either emanated from the cladding inner surface or precipitated close to the cladding inner surface. Figures 71 and 72 show images of a 24%-long radial hydride close to the inner surface. Figures 73 and 74 show a group of radial hydrides with ≤20% RHCF emanating from or close to the cladding inner surface. These radial hydrides are relatively close in location to the radial hydride shown in Figs. 73 and 74.

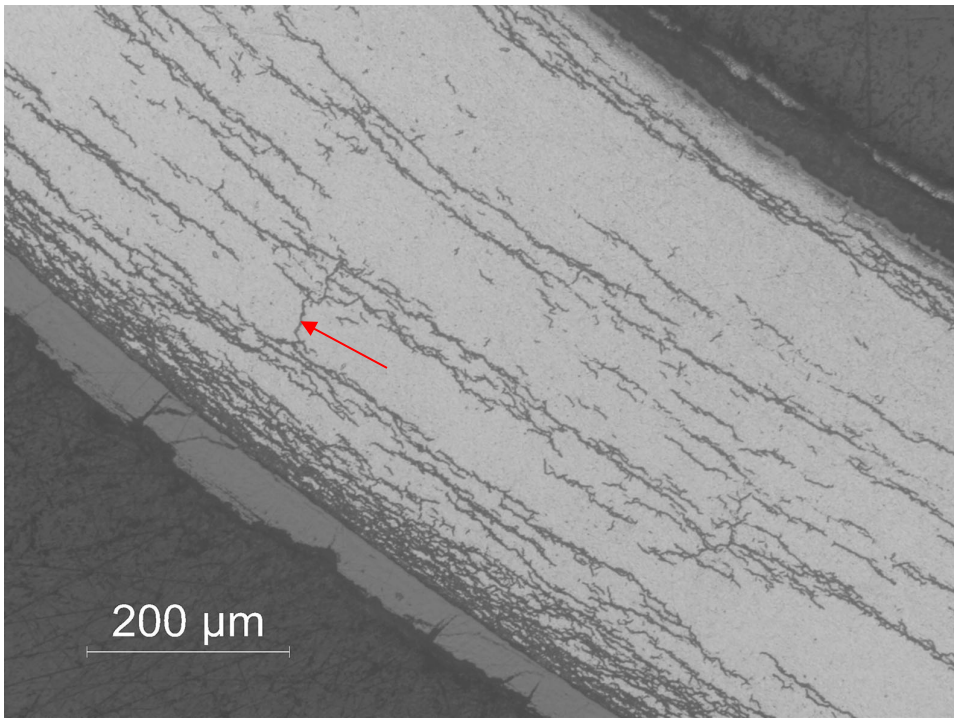

Figure 67: 100X image of the longest radial hydride (26% RHCF) observed at the 7 o'clock orientation of ZIRLO® surface 656B11 located at ≈3248 mm from the bottom of FHT fuel rod 3F9N05.

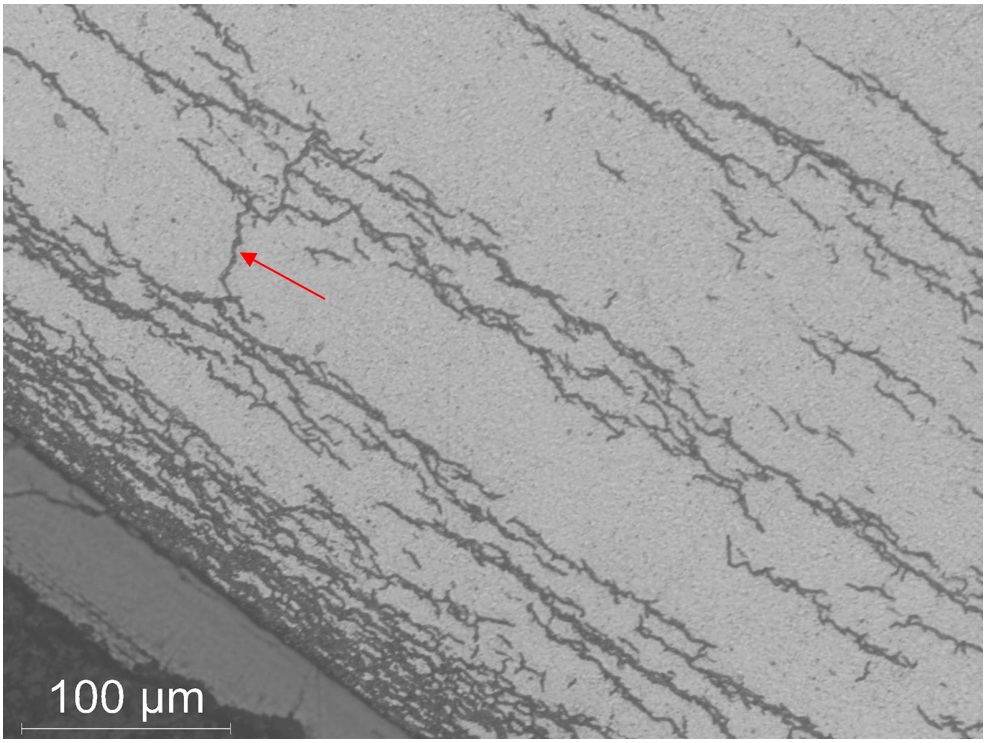

Figure 68: 200X image of the longest radial hydride (26% RHCF) observed at the 7 o'clock orientation of ZIRLO® surface 656B11 located at ≈3248 mm from the bottom of FHT fuel rod 3F9N05.

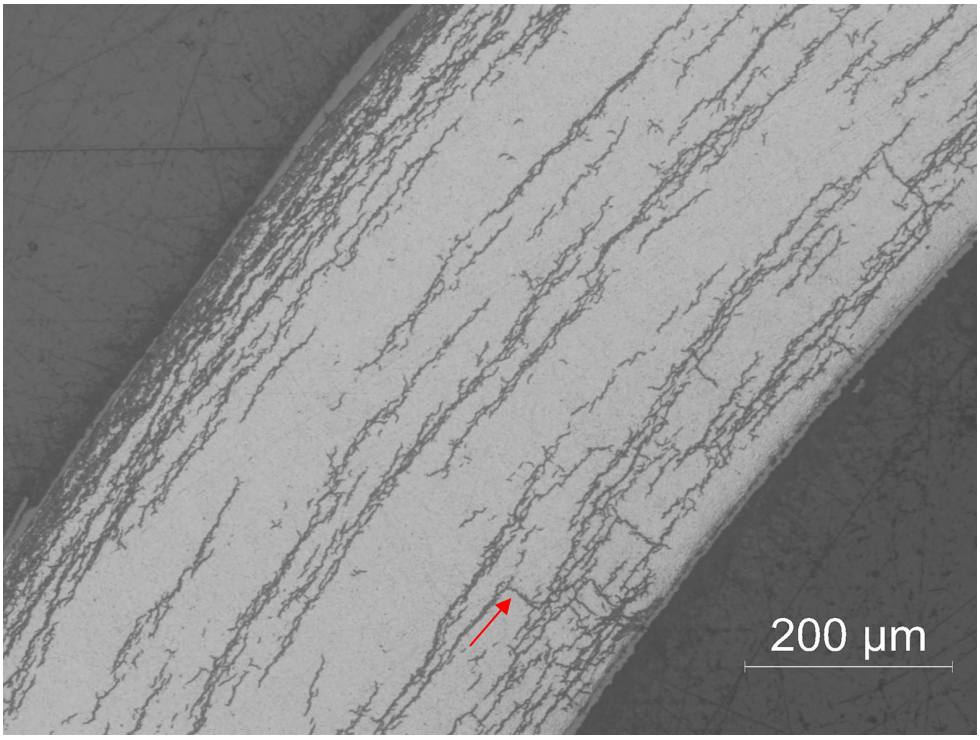

Figure 69: 100X image of the longest radial hydride (25% RHCF) observed at the 10 o'clock orientation of ZIRLO® surface 656B11 located at ≈3248 mm from the bottom of FHT fuel rod 3F9N05.

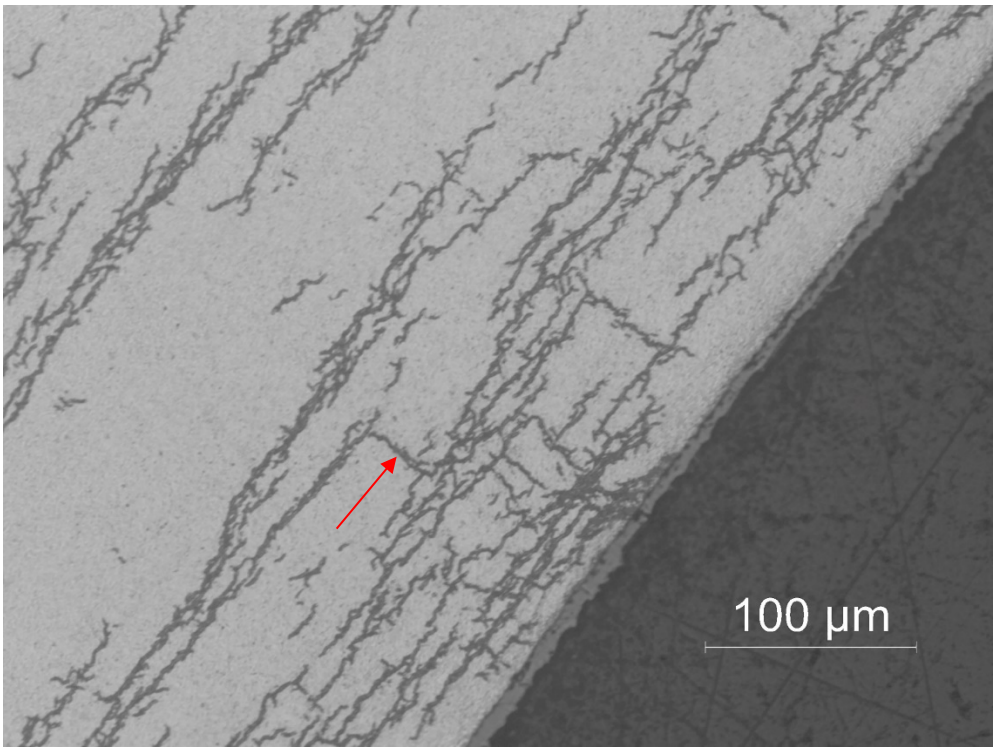

Figure 70: 200X image of the longest radial hydride (25% RHCF) observed at the 10 o'clock orientation of ZIRLO® surface 656B11 located at ≈3248 mm from the bottom of FHT fuel rod 3F9N05.

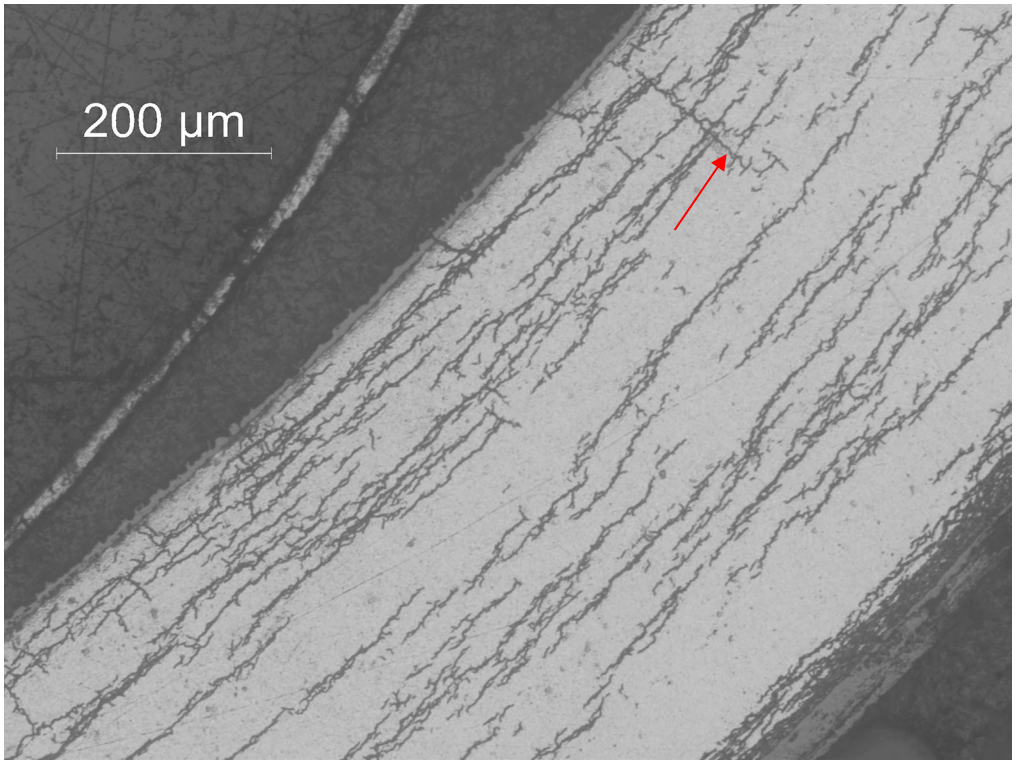

Figure 71: 100X image of the longest radial hydride (24% RHCF) observed at the 4 o'clock orientation of ZIRLO® surface 656B11 located at ≈3248 mm from the bottom of FHT fuel rod 3F9N05.

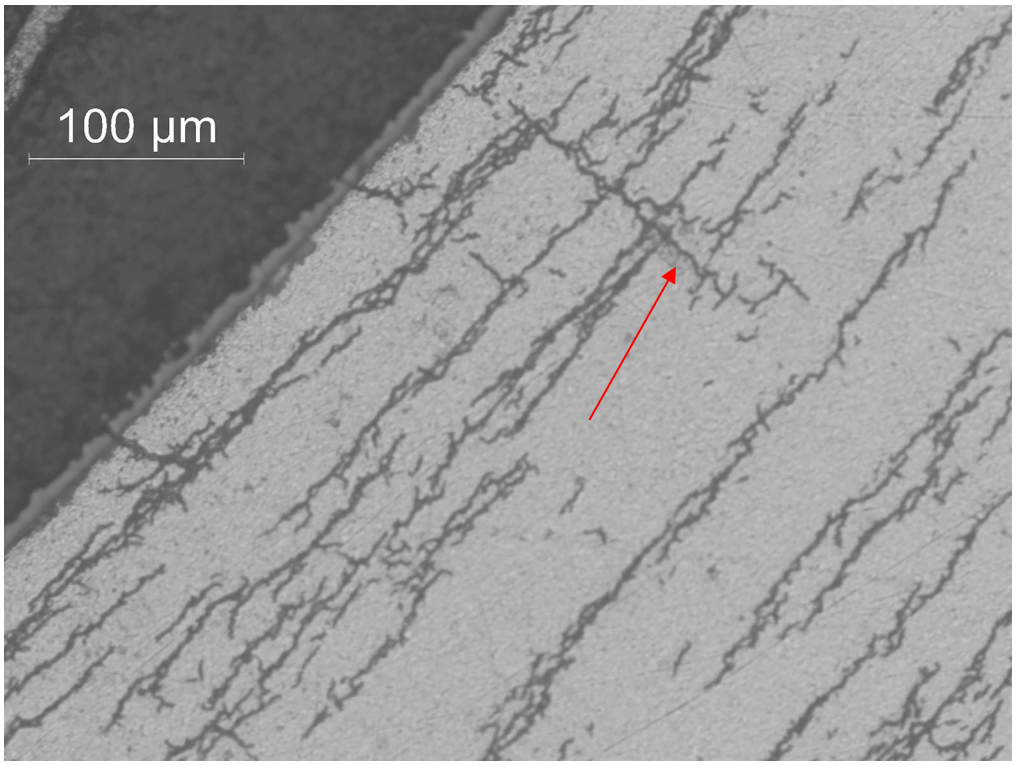

Figure 72: 200X image of the longest radial hydride (24% RHCF) observed at the 4 o'clock orientation of ZIRLO® surface 656B11 located at ≈3248 mm from the bottom of FHT fuel rod 3F9N05.

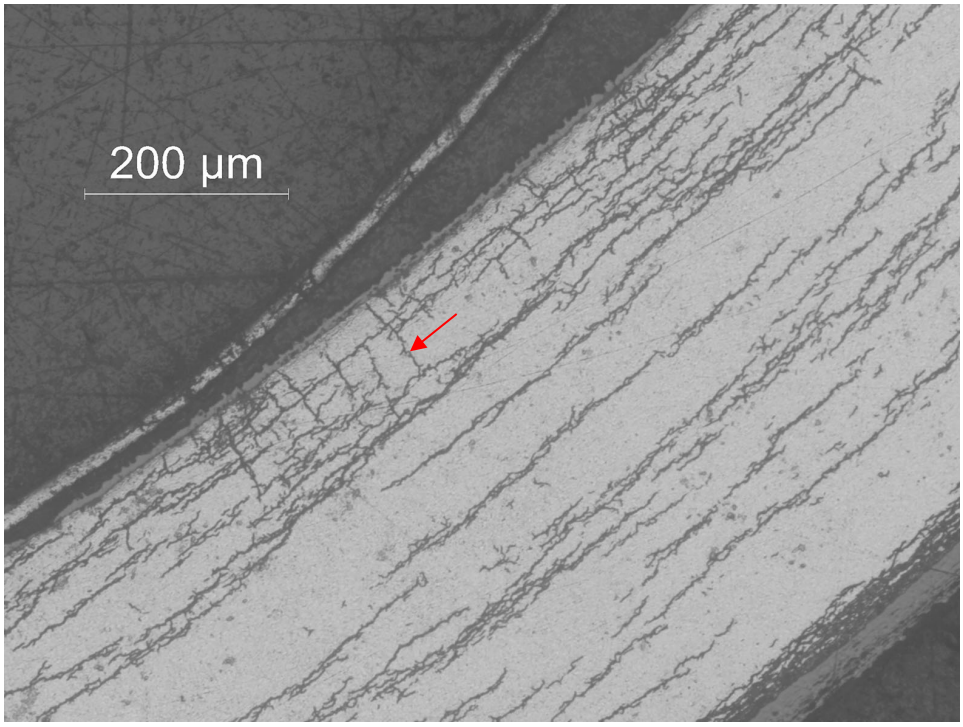

Figure 73: 100X image of radial hydrides (≤20% RHCF) observed at the 4 o'clock orientation of ZIRLO® surface 656B11 located at ≈3248 mm from the bottom of FHT fuel rod 3F9N05.

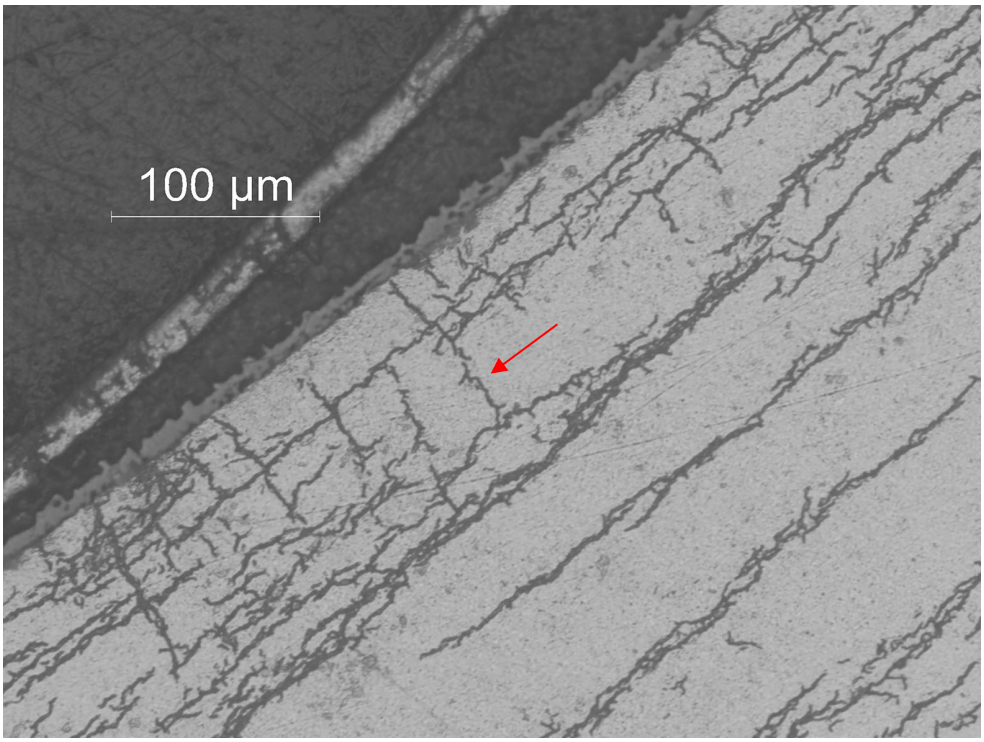

Figure 74: 200X image of radial hydrides (≤20% RHCF) observed at the 4 o'clock orientation of ZIRLO® surface 656B11 located at ≈3248 mm from the bottom of FHT fuel rod 3F9N05.

RCT Results

All 656B RCT samples were tested at RT and 0.05 mm/s. As shown in Fig. 2, this heat-treated ZIRLO® segment contained regions of peeled oxide. RCT samples B2−B7 contained local outer surface regions with peeled oxide. These samples were rotated with respect to the loading direction such that the peeled oxide was at the 3 or 9 o'clock orientation where the tensile hoop stress at the outer wall is maximum. Samples B8−B10 contained no regions of peeled oxide. As such these samples were oriented such that contact of the loading plate with the ring occurred between the black and red lines shown in Fig. 66. With the exception of samples B3 and B8, the remaining six RCT samples were subjected to a maximum sample displacement of 1.7 mm. RCTs with samples B3 and B8 were terminated at 23% load drop at large displacement and 13% load drop at low displacement, respectively, for metallographic examination to correlate abrupt load drop with extent of cracking.

Figures 75 through 82 show the RCT load-displacement curves for samples B2−B5 and B7−B10, respectively. All samples experienced load drops in the range of 3% to 23%. For samples with minor load drops (3% to 10%), the offset strains were in the range of 9.7% to 11.5%, which indicated that the ductility of these samples was >10%. Sample B3 experienced a 23% load drop at 7.8% offset strain, which is close to the >25% load-drop failure criterion. As such, the ductility of this sample was assessed to be 7.8%.

Samples B2 (Fig. 75), B4 (Fig. 77) and B7 (Fig. 79) experienced small load drop (≤7%) at high offset strain. Thus, the load drops were of no consequence in the determination of offset strain and ductility. For samples B5 (Fig. 78), B9 (Fig. 81) and B10 (Fig. 82), load drops of 6% to 10% occurred at low and intermediate displacements. On the basis of the load recovery following the load drop, it is clear that cracking was relatively minor. For B5 with a low-displacement load-drop of 10%, the load dropped from 573 N to 517 N and recovered to 555 N. If significant cracking had occurred, the load recovery would have been much less. None of these samples exhibited an implied load drop (discussed in Section 2).

Excluding samples B4 and B7, which experienced loading lags, the normalized loading slopes (1032±67 N/mm) were consistent for the other eight samples. The normalized values of P_{max} were even more consistent and independent of small loading lags: 594±17 N.

It is not clear from the load displacement curves if local regions of peeled oxide had any effect on the RCT response. RCT samples B3 (23% load drop) and B8 (13% load drop) were subsectioned for metallographic examination to determine crack extent and location. If major cracks occurred at the 12 and/or 6 o'clock orientations due to radial hydrides, then the region of peeled oxide would have had no effect on cladding ductility for B3. If the crack or cracks initiated at locations of the peeled oxide (3 or 9 o'clock), then oxide peeling might have had a degrading effect on RCT sample response.

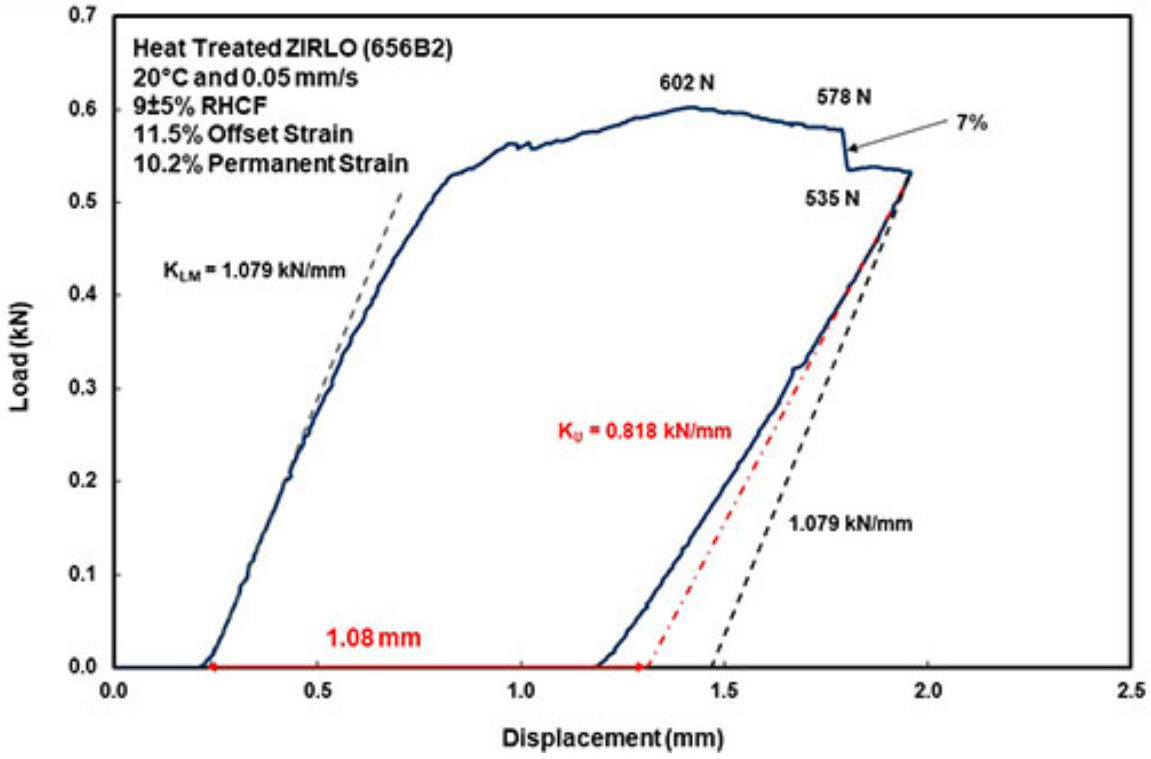

Figure 75: Load-displacement curve for RCT sample 656B2.

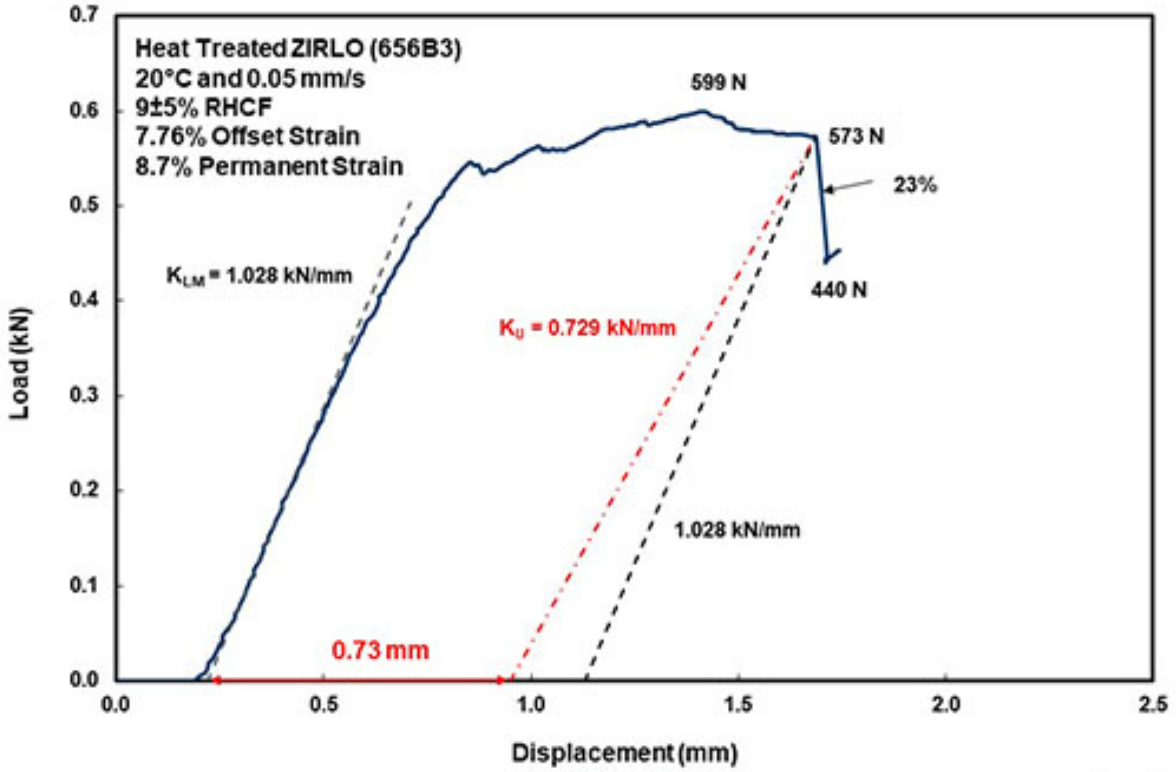

Figure 76: Load-displacement curve for RCT sample 656B3.

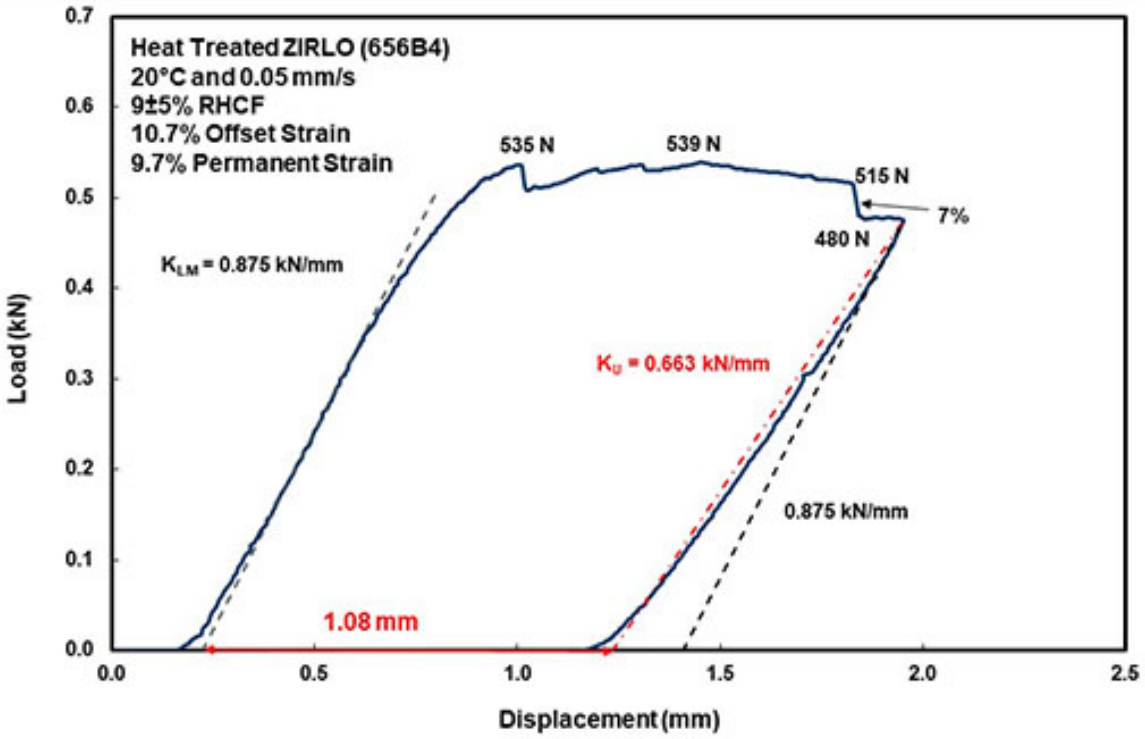

Figure 77: Load-displacement curve for RCT sample 656B4.

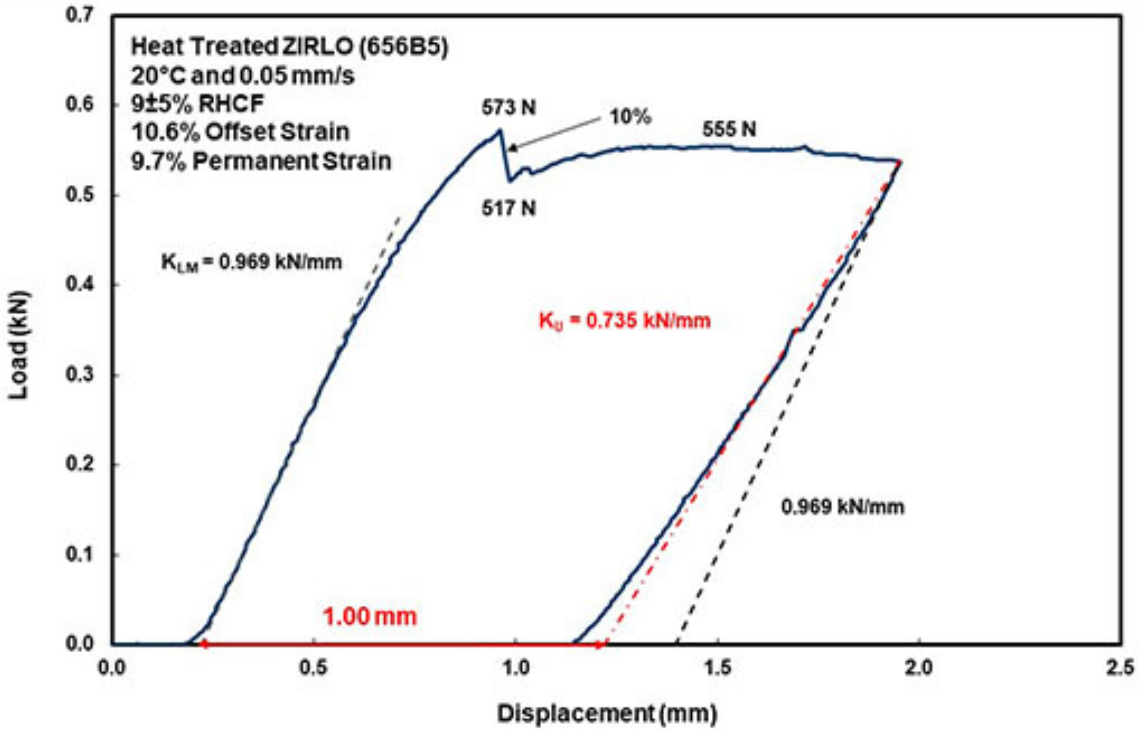

Figure 78: Load-displacement curve for RCT sample 656B5.

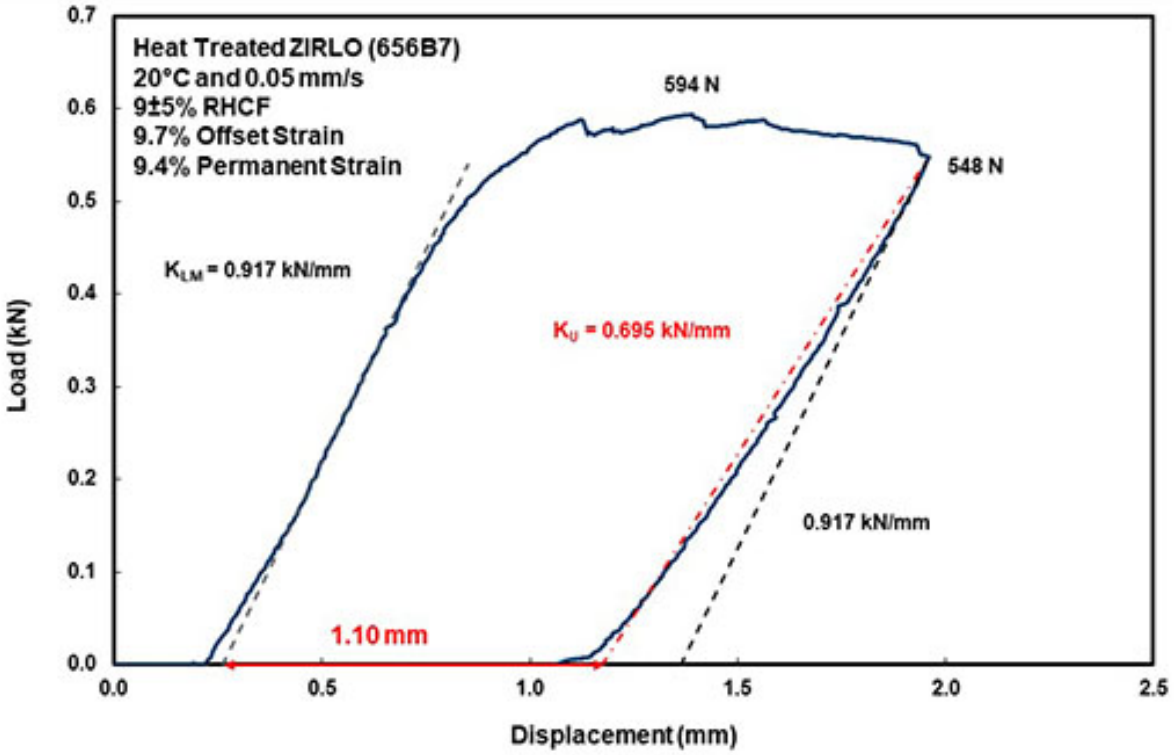

Figure 79: Load-displacement curve for RCT sample 656B7.

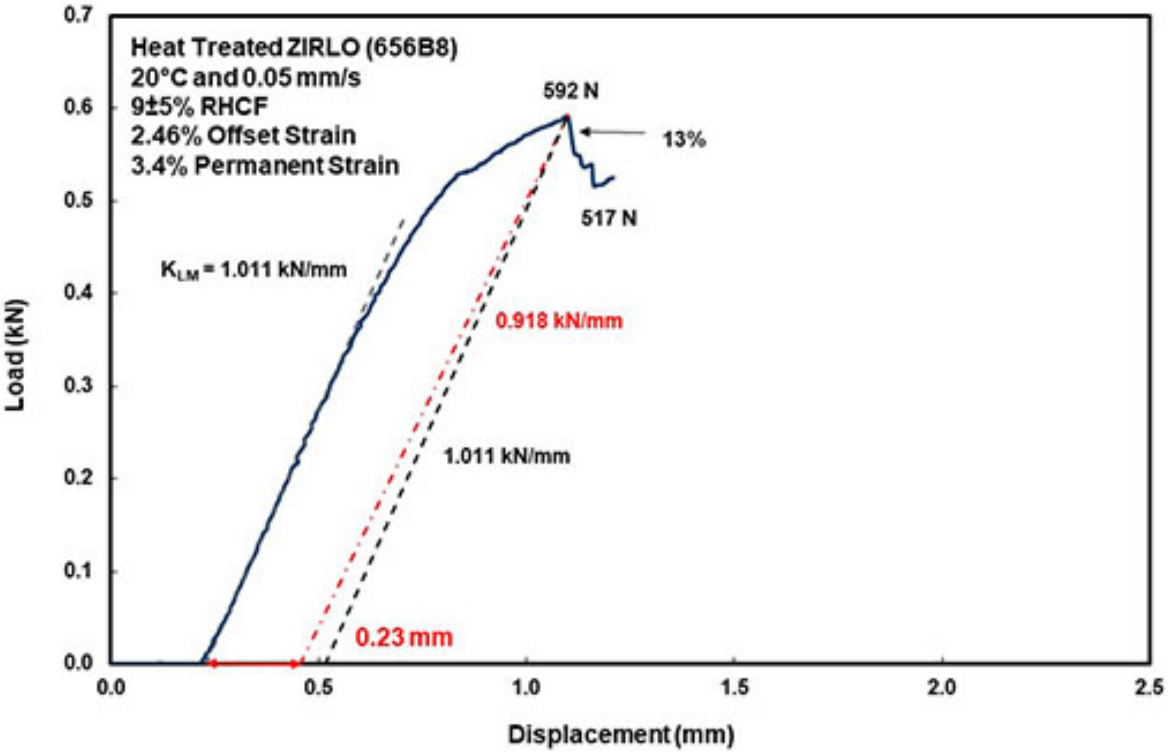

Figure 80: Load-displacement curve for RCT sample 656B8.

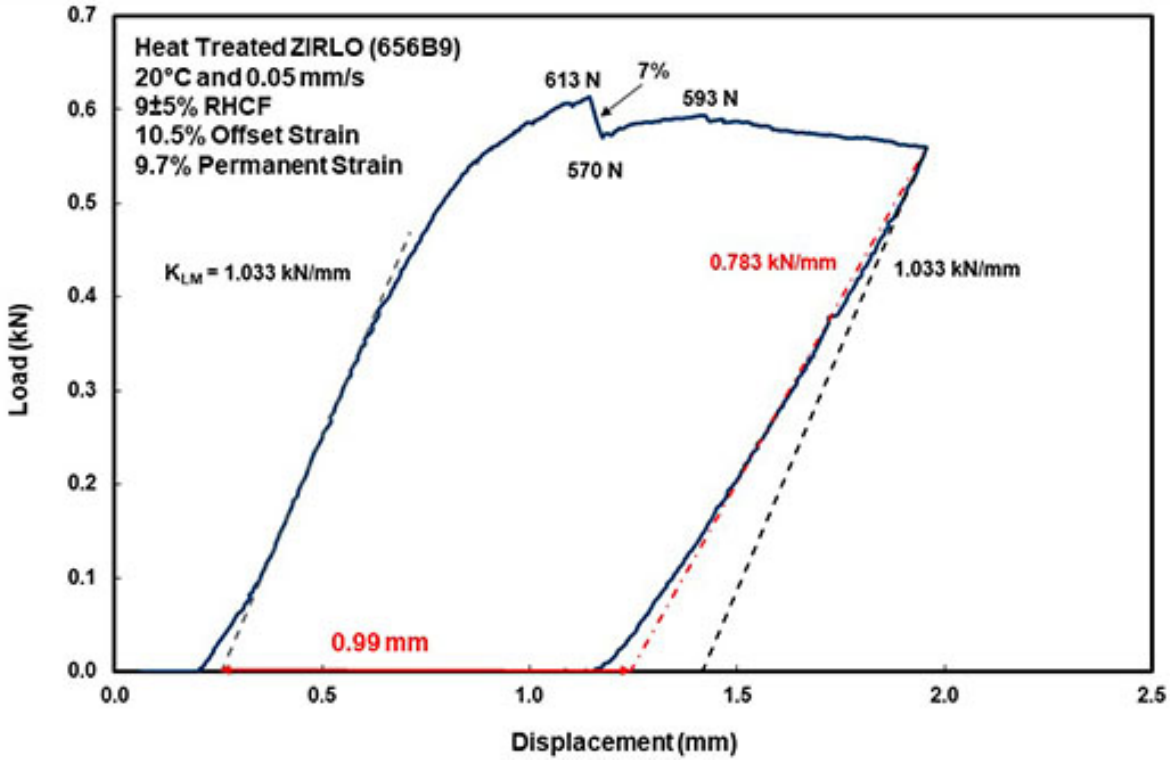

Figure 81: Load-displacement curve for RCT sample 656B9.

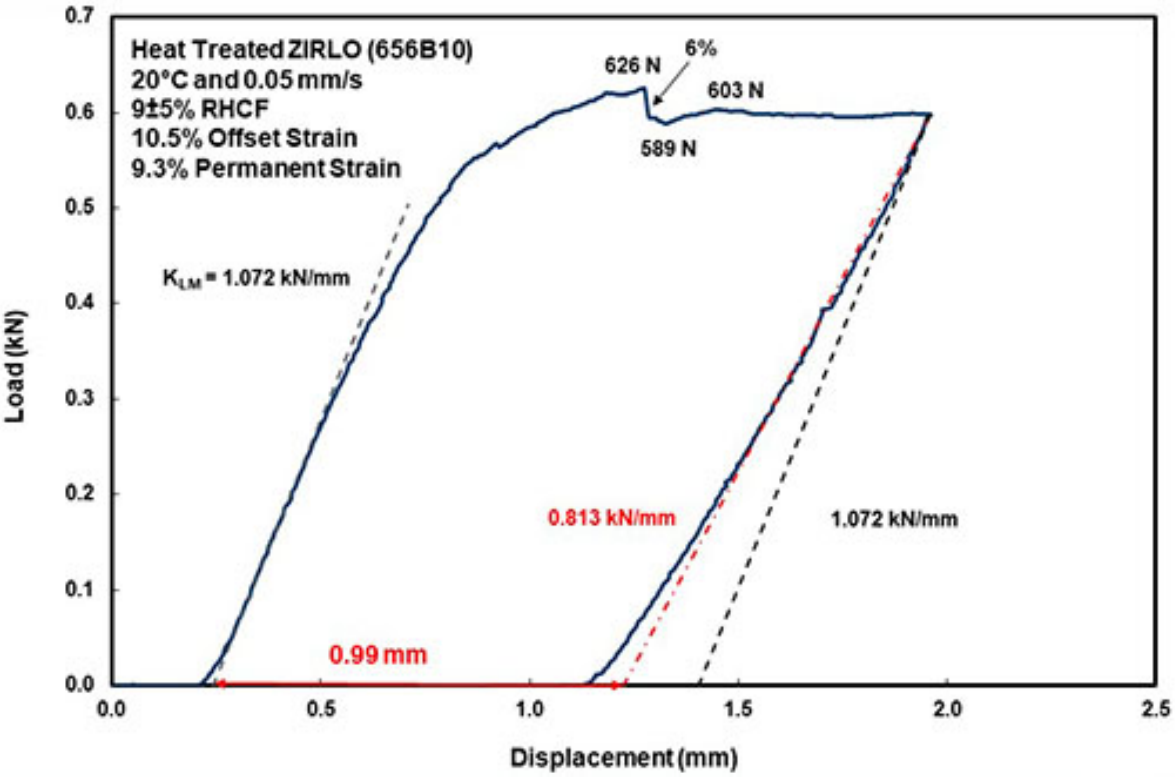

Figure 82: Load-displacement curve for RCT sample 656B10.

6. DISCUSSION

Benchmark Tests with As-Fabricated 17×17 M5® Cladding Samples

At least three RCT tests are routinely conducted with AF 17×17 M5® cladding samples (nominal dimensions of 9.50-mm D_o, 0.57-mm and 0.61-mm h_m, and 8.0 mm length) prior to testing irradiated samples to ensure that there has been no changes in the response of the Instron 8511 machine. A large data base has been collected for this material since 2011. These tests have been conducted at 0.05 mm/s and 5 mm/s displacement rates and at RT and 120°C. During March 2020, additional tests were conducted with 0.61 mm thick M5® to "test" the performance of a new team of experimenters. The previous Instron expert, who left ANL in April 2019, had for 15 years performed all glove-box work (i.e., pre- and post-test sample measurements, sample positioning on the support plate, etc.) and operated the Instron controls. He was replaced by an expert in glove box operations and an expert in operating Instron controls. During the third week in March 2020, seven tests were conducted at RT: four at 0.05 mm/s and three at 5 mm/s. Agreement was excellent between the results of the March tests and previous tests in terms of normalized (to 8-mm sample length) loading slope, maximum load, and permanent displacement and strain. Benchmark tests were repeated by this team in June 2020 after a three-month delay due to COVID-19 restrictions. These benchmark tests are essential to perform prior to data-generation for irradiated cladding, especially if there are changes in personnel or changes to the Instron (e.g., replacing grips).

Ductility of Sibling Pin M5® Cladding

For as-irradiated M5® RCT samples tested at RT and 0.05 mm/s, abrupt load drops indicative of cracking were not observed. For samples that did not exhibit significant loading lags, maximum offset strains were about 10%. This indicates a high ductility >10%. The normalized (to 8-mm length) P_{max} achieved by these samples was 534±6 N. This is important for comparison with the P_{max} achieved by heat-treated M5® to determine if partial annealing may have occurred during the unplanned temperature excursion to 485°C. Partial annealing would result in a decrease in P_{max}. An important geometrical parameter needed for this comparison is the cladding wall thickness divided by the cladding mid-radius (h_m/R_{mid}), which was 0.125±0.001 for as-irradiated M5®. As shown in Eq. 2, the cladding stiffness varies with $(h_m/R_{mid})^3$. Previous work has indicated that the maximum load in the plastic deformation regime is proportional to $(h_m/R_{mid})^n$, where n is <3.

The heat-treated (401°C and 52-MPa hoop stress at cooling initiation) M5® used in the current study also exhibited high ductility under the same test conditions. The RHCF was 18±12% of the cladding wall with a maximum value of 59%. One of eight samples tested experienced a major load drop (29%) at 7.8% offset strain, which is also the ductility for this sample. Metallographic examination revealed an end crack extending through 60% of the cladding wall and a primary mid-span crack extending through 54% of the cladding wall. These crack lengths are consistent with the maximum RHCF values. Six of the remaining seven samples exhibited no load drops, which implied no cracking. One of the samples had a 9% load drop, which indicates minor cracking. Seven samples had maximum offset strains of about 10%, which implied >10% ductility. The normalized P_{max} was 529±7 N for h_m/R_{mid} = 0.129±0.001. Based on this geometrical parameter, maximum loads for the heat-treated M5® were expected to be $(1.032)^n$ higher than for the as-irradiated M5®. For n = 2, this gives a normalized P_{max} that would be 6.5% higher. However, given uncertainties, the normalized maximum loads are too close to draw conclusions about partial annealing. Hardness or micro-hardness measurements for the baseline and heat-treated cladding are a better way to determine if partial annealing had occurred.

Ductility of Sibling Pin ZIRLO® Cladding

No RCT load drops indicative of cracking were observed for as-irradiated ZIRLO® samples. Excluding samples with significant loading lags, the maximum offset strain was about 10% indicating >10% ductility. Metrics considered in evaluating the adequacy of as-irradiated ZIRLO® as baseline material for heat-treated ZIRLO® were: C_H (estimated to be 350±40 wppm based on oxide layer thickness), hydride distribution across the cladding wall, and the geometrical parameter h_m/R_{mid} (0.126±0.002). The hydride distribution across the cladding wall consisted of a hydride rim near the cladding outer surface, a group of several circumferential hydrides near the cladding inner surface (not previously observed), and a region extending across 70% to 80% of the cladding essentially devoid of hydrogen except for sparsely distributed short hydrides forming an x-like pattern (not previously observed). The low C_H of this region may have been due to axial migration of hydrogen to colder cladding under the closest grid spacer. Although very few radial hydrides were expected in as-irradiated ZIRLO®, the RHCF was 8±4% of the cladding wall thickness with a maximum value of 26%.

RCT load-displacement curves for heat-treated (400°C and 66-MPa hoop stress at cooling initiation) ZIRLO® indicated that six of the eight rings tested exhibited minor load drops (3% to 10%), which would result in minor cracking. The maximum offset strains for these samples were ≥10%, which indicated that the ductility strain was >10%. One sample exhibited a 23% load drop at 7.8% offset strain at which point the test was stopped to allow examination of cracking extent for this load drop. For another sample, a 13% load drop occurred at 2.5% offset strain. This test was also terminated to investigate cracking extent caused by a 13% load drop. The h_m/R_{mid} value was 0.126±0.001, which indicates that the as-fabricated ZIRLO® was a good baseline for the heat-treated ZIRLO® in terms of RCT parameters of loading slope and maximum load. However, the oxide layer was thicker and the estimated C_H was higher (550±50 wppm). Also, the radial distribution of hydrides was quite different from what was observed for the as-irradiated sample. Circumferential hydrides were present from the cladding outer- to inner-surface. These two factors suggest that the as-irradiated ZIRLO® was not a good baseline for the heat treated ZIRLO® in terms of hydrogen content, hydride distribution, and hydrogen morphology. The measured RHCF was 9±5% with a maximum value of 26%, which is low because of the low hoop stress at cooling initiation.

Future Work

Additional characterization will be performed to determine C_H and the relationship between RCT load drops and cracking extent. A new hydrogen analyzer has been ordered and will be delivered by the end of October 2020. RCT samples which exhibited load drops of 9% (heat-treated M5®), 13% (heat-treated ZIRLO®) and 23% (heat-treated ZIRLO®) have been sectioned for metallographic examination. This work was not completed because of hardware problems with the 13-year-old microscope. If the microscope cannot be repaired, a new one will be ordered and installed in the designated glove box.

The characterization and ring-compression testing presented in this report will be performed for the ten remaining defueled cladding segments provided by ORNL: as-irradiated and heat treated M5® from lower in their respective fuel rods, as-irradiated and heat treated ZIRLO® from lower in the their respective fuel rods, two as-irradiated LT Zry-4 segments, and two heat treated Zry-4 segments. In addition, PNNL will be sending ten defueled cladding samples to ANL in FY2021 with five that will be 51-mm long and five that will be 152-mm long. These will be in the as-irradiated condition. ANL will subject the longer samples to radial hydride treatment (RHT) with RT pressures ≤5 MPa. Efforts will continue to refine the details of RHCF determination, as well as the correlations among the abrupt load-drop magnitude, the extent of cracking, and the RHCF. These are important issues for the development of the RCT ASTM standard.

REFERENCES

[1] Montgomery, Rose, Bruce Bevard, Robert N. Morris, James Goddard, Jr., Susan K. Smith, and Jianwei Hu, *Sister Rod Nondestructive Examination Final Report*, SFWD-SFWST-2017-000003 Rev. 1, ORNL/SPR-2017/484 Rev. 1, May 16, 2018.

[2] Saltzstein, Sylvia J., Mike Billone, Brady Hanson, and John Scaglione, "Visualization of the High-Burnup Spent Fuel Rod Phase 1 Test Plan: Technical Memo," SAND2018-8042 O, Jul. 18, 2018.

[3] Ahn, T., H. Akhavannik, G. Bjorkman, F.C. Chang, W. Reed, A., Rigato, D. Tang, R.D. Torres, B.H. White, and V. Wilson, *Dry Storage and Transportation of High Burnup Spent Nuclear Fuel*, NUREG-2224, July 2018 draft report for public comment.

[4] Montgomery, Rose, Robert N. Morris, Ralph Ilgner, Benjamin Roach, Jy-An Wang, Zachery Burns, James T. Dixon, and Stephanie M. Curlin, *Sister Rod Destructive Examinations (FY19)*, ORNL/SPR-2019/1251 Revision 1, Sep. 27, 2019.

[5] Shimskey, RW, JR Allred, RC Daniel, MK Edwards, J Geeting, PJ MacFarlan, LI Richmond, TS Scott, and BD Hanson, *PNNL Phase 1 Update on Sibling Pin Destructive Examination Results*, PNNL-29179, Sep. 27, 2019.

[6] Billone, M.C. and T.A. Burtseva, *Preliminary Destructive Examination Results for Sibling Pin Cladding*, Argonne National Laboratory Report ANL-19/53 Rev. 2, March 25, 2020.

[7] Geelhood, K.J., W.G. Lusher, and C.E. Beyer, *PNNL Stress/Strain Correlation for Zircaloy*, Pacific Northwest National Laboratory Report PNNL-17700, July 2008.

[8] Geelhood, K.J., W.G. Lusher, and P.A. Raynaud, *Material Property Correlations: Comparison Between FRACAON-3.5, FRAPCON-1.5, and MATPRO*, NUREG/CR-7024, Rev. 1, October 31, 2014, ML14296A063.

[9] Billone, M.C., T.A. Burtseva, and Y. Yan, *Ductile-to-Brittle Transition Temperature for High-Burnup Zircaloy-4 and ZIRLO™ Cladding Alloys Exposed to Simulated Drying-Storage Conditions*, Argonne National Laboratory Report ANL-13/13, NRC ADAMS ML12181A238, Sept. 2012.

[10] Billone, M.C., T.A. Burtseva, and R.E. Einziger, "Ductile-to-Brittle Transition Temperature for High-Burnup Cladding Alloys Exposed to Simulated Drying-Storage Conditions," J. Nucl. Mater. **433**, 431–448 (2013).

[11] Fourgeaud, S, J. Desquines, M. Pettit, C. Getrey and G. Sert, "Mechanical characteristics of fuel rod claddings in transport conditions," Packaging, Transport, Storage & Security of Radioactive Material, Vol 20, no. 2 (2009), pp 69-76.

[12] Billone, M.C., T.A. Burtseva, and Y.Y. Liu, *Baseline Studies for Ring Compression Testing of High-Burnup Fuel Cladding*, Argonne National Laboratory Report ANL-12/58, FCRD-USED-2013-000040, Nov. 23, 2012.

[13] Billone, M.C., T.A. Burtseva, Z. Han, and Y.Y. Liu, *Embrittlement and DBTT of High-Burnup PWR Fuel Cladding Alloys*, Argonne National Laboratory Report ANL-13/16, FCRD-UFD-2013-000401, Sept. 30, 2013.

[14] Billone, M.C. and T.A. Burtseva, *Effects of Lower Drying-Storage Temperatures on the Ductility of High-Burnup PWR Cladding*, Argonne National Laboratory Report ANL-16/16, FCRD-UFD-2016-000065, Aug. 30, 2016.

[15] Kammenzind, B.F., D.G. Franklin, H.R. Peters, and W.J. Duffin, "Hydrogen Pickup and Redistribution in Alpha-Annealed Zircaloy-4," *Zirconium in the Nuclear Industry: 11th Intl. Symp.*, ASTM STP 1295, E.R. Bradley and G.P. Sabol, Eds., ASTM, pp. 338–370, 1996.

[16] Kearns, J.J., "Terminal Solubility and Partitioning of Hydrogen in the Alpha Phase of Zirconium, Zircaloy-2 and Zircaloy-4," J. Nucl. Mater. **22**, 292–303, 1967.